GNSS Signal Analysis using High Gain Antenna

Pratana Kukieattikool

16.February 2009

Contents

1. Introduction **2**

2. Introduction to the Global Positioning System (GPS) **4**
2.1 System Architecture 4
2.2 Signals 6
2.3 Spectral Analysis 10

3. Signal Power and Correlation Function **14**
3.1 Energy of the Signal 14
3.2 Correlation Property 15
3.3 Correlation Peak Deformation 19
3.4 Signal Power Level 19

4. Code Modulation / Sub Modulation **21**
4.1 BPSK (Binary Phase-Shift Keying) 21
4.2 QPSK (Quadrature Phase-Shift Keying) 21
4.3 BOC (Binary Offset Carrier) 23
4.4 MBOC (Multiplexed Binary Offset Carrier) 27

5. Measurement and Processing **28**
5.1 Measurement Facility 28
5.2 Absolute Calibration 28
5.2.1 System Gain Calibration 28
5.2.2 Antenna Gain Calibration 29
5.3 Spectral Analysis 30
5.3.1 Spectral Calibration 30
5.3.2 Comparison with Theoretical Spectrums 30
5.3.3 Spectral Asymmetry 32
5.3.4 Measurement Dependency on the Elevation 33
5.4 IQ Data Analysis 33
5.4.1 IQ Data Processing 33
5.4.2 Error Vector Magnitude 36
5.4.3 Correlation Peak Determination 37
5.4.4 IQ Data Filtering 39
5.4.5 IQ Data with Pwelch 39

6. Result and Analysis **40**
6.1 GPS BIIR12 L1 40
6.2 GPS BIIR12 L2 45
6.3 GPS BIIRM6 L1 47

6.4 GPS BIIR12 L1 with Elevation Plot 54
6.5 GPS BIIRM6 L1 with Elevation Plot 60

7. Analysis with Filtering **65**
7.1 GPS BIIR12 L1 with Chebychef Filtering 66
7.2 GPS BIIR12 L1 with FIR Filtering 75

8. Signal Deformation Analysis **85**
8.1 Non-Linear Power Amplification 85
8.2 Dispersive Behavior of the Front-End 88
8.3 Offset of the Constant Component 93

9. Conclusion **97**

Appendix **99**
A1. Spectrum_Programm 99
A1.1 Spectrum_theory_calibrierung 99
A1.2 Spectrum_antennapattern_elevation 99
A2. IQ_Programm 99
A2.1 IQ_processing 99

Bibliography **100**

1. Introduction

The Institute of Communication and Navigation of the German Aerospace Center (DLR) established an independent monitoring station for the analysis of GNSS signals in September 2005. The deep space antenna is 30 meter and located at the DLR Weilheim. This antenna has a broadband circular polarized feed, which raises the GNSS signal above the noise level. Very precise measurement can be obtained with the aid of an online calibration system, a real-time spectrum analyzer and a signal evaluation facility.

Figure 1.1: 30m High Gain Antenna at Weilheim

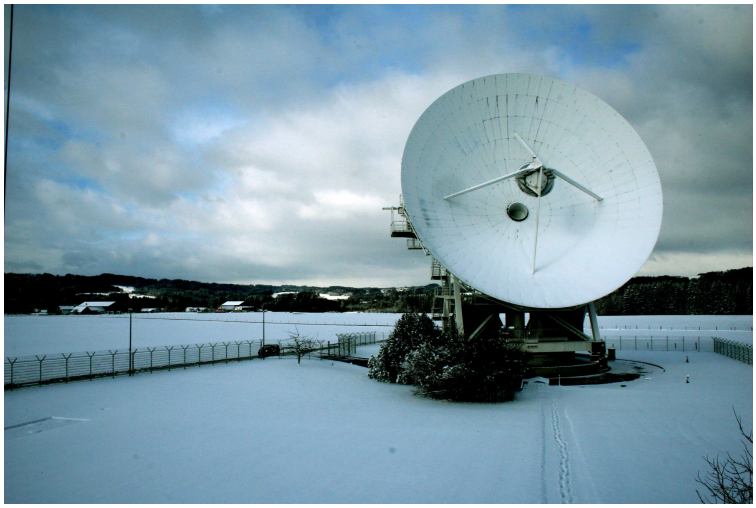

Figure 1.2: 30m High Gain Antenna at Weilheim

The aim of this thesis is to analyze the measurement signals from the Global Positioning System (GPS), the US Satellites Navigation System. The analysis focuses on the signal characteristics on both time and frequency domain. In frequency domain the power spectral density, the asymmetry of the power in the bandwidth, and the variation of the power over the elevation are determined. In time domain the characteristic derived from the IQ measurement data such as IQ constellation, eye diagram, error vector magnitude, correlation function and discrimination functions, which leads to the conclusion of the transmitted signal quality, are determined. Finally the causes of signal impairment such as filter, linear amplifier, distortion of the front-end and offset of the constant component are studied.

After this introduction, chapter 2 gives an overview of the GPS system. The system architecture with short descriptions of each satellite generation is described. The details of the signal components as well as the derivation of the power spectral theory are also discussed in detail.

Chapter 3 describes the definition of the energy of the signal as a basic knowledge for the power of the signal. The correlation function is introduced, since this function is an important part in the acquisition process and will be later investigated later. A short description of the correlation peak deformation is given. The derivation of the signal power level and their related parameter are defined with the purpose of evaluating the power spectral density.

Then, chapter 4 introduces the code modulation and sub modulation, which are used in GPS. Their power spectral densities are also given.

Chapter 5 deals with the measurement facility, absolute calibration, spectral data processing such as spectral calibration, spectral comparison with theoretical spectrums derived from chapter 2 and 4, asymmetry test of the signal, and power over elevation. The IQ data processing is also explained including terms related to quantifying the IQ data, such as error vector magnitude, phase error, magnitude error, and modulation error ratio. The process after IQ data processing such as correlation function, discrimination function, filtering, and using pwelch function in MATLAB are described.

Chapter 6 analyses the GPS measurement signal obtained from the processes in the last chapter. The legacy signal from GPS BIIR 12 in both L1 and L2 band are chosen for examination. For the modernized signal of BIIRM 6 only the L1 signal is analyzed. The power over elevation plots and antenna pattern for these signals are presented.

In chapter 7, the signal distortion, correlation peak distortion and discriminator distortion due to different filter and bandwidth are evaluated.

Chapter 8 analyzes the causes of the signal deformation, like non-linear power amplification, dispersive behavior of the signal front-end and offset of the constant component.

Finally, chapter 9 summarizes the main results and suggests for future work.

2. Introduction to the Global Positioning System (GPS)

The United States' Satellite Navigation System was first developed in 1973 by the U.S. Department of Defense (DoD) on purpose of estimating the position, velocity, and time. The first satellite was launched in 1978 and the system operation is declared in 1995. Two kinds of service are offered:

- Standard Positioning Service (SPS) for peaceful and civil use
- Precise Positioning Service (PPS) for the DoD authorized users.

2.1 System Architecture

GPS consists of three segments.

- The first one is the **Space Segment**, which comprises the baseline constellation of 30 satellites fielded in nearly circular orbits with a radius of 26,560 km. The orbital period lasts 11 hours 58 minutes. The satellites are arranged in six orbital planes inclined at 55^{o} relative to equatorial plane. The identification of each satellite composed of a letter identifies the orbital plane and a number identifies the satellite number in a plane.

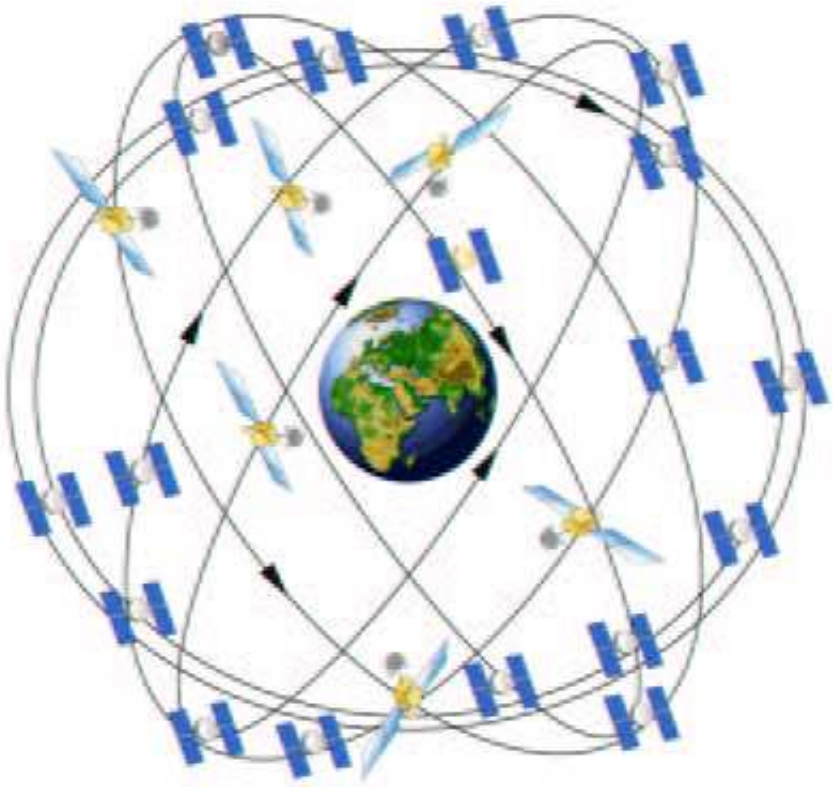

Figure 2.1: GPS satellite constellation (Source [36])

There are 7 phases of development of GPS, based on the order of operation; these are

- Block I (Initial Concept Validation Satellites) : They were the developmental prototypes to validate the initial GPS concept.
- Block II (Initial Production Satellites) : The enhancement was obtained due to the experience from Block-I. The AS[1] and SA[2] were added.
- Block IIA (Upgraded Production Satellites) : This block is very similar to Block II, but there are some system enhancements such as equipment of mutual communication.
- Block IIR (Replenishment Satellites) : They are totally compatible upgraded and replacement to Block II, Block IIA. The system support C/A, P(Y) code on L1, P(Y) code on L2 with additional ultra-high-frequency (UHF) crosslink capability and sufficient power capacity.
- Block IIR-M (Modernized Replenishment Satellites) : new functionality were built into the satellites of Block IIR, which were waiting to be sent in orbits. These new functionalities are: increasing of L-band[3] signal power, providing two new military M-codes on L1 and L2, providing a new civilian L2C-code on L2.
- Block IIF (Follow-On Sustainment Satellites) There are some requirements to improve the performance such as new civil signal L5 at the frequency of 1176.45 MHz.
- Block III (Next Generation Satellites) They are expected to provide sub meter accuracy, greater timing accuracy, a system integrity solution, a high data capacity inter satellite crosslink capability, and higher signal power to meet military anti-jam requirements.

The user can observe at minimum four satellites at a time, which is the least number required to estimate the user position (3 dimensions) and receiver clock bias.
The pseudorange measurement is based on the time of transmission and receipt of signals

$$\rho(t) = c[t_u(t) - t^s(t-\tau)] \tag{2.1}$$

whereas c is the velocity of light, the term $t^s(t-\tau)$ is the emission time, $t_u(t)$ is the arrival time measured by the user's receiver clock, and τ is the transit time. After all factors are determined, the equation is as follows:

$$\rho(t) = r + c[\delta t_u - \delta t^s] + I_\rho + T_\rho + \epsilon_\rho \tag{2.2}$$

whereas r is the true range to the satellite, δt_u is the receiver clock bias, δt^s is the satellite clock bias, I_ρ and T_ρ are the delays associated with the transmission of the signal through the ionosphere and troposphere, ϵ_ρ is the unmodeled error such as modeling error and measurement error.
The satellites broadcast ranging signals and navigation data allow the users to measure their pseudoranges and to estimate their position in passive, which means the user does not send a signal to the satellite. This enables an unlimited number of users.

- The second segment is the **Control Segment**, which deals with the management of the satellite operation. The most important part is the *Master Control Segment* (MSC), located at the Schriever Air Force Base near Corolado Springs, Corolado. It operates the system and provides command and control function. The *monitor stations* track signals continuously from different

[1] AS is referred to Anti-Spoofing. The encrypted P-code is referred to as a Y-code, which is commonly called P(Y)-code. Its main purpose was to protect a user from fake GPS signals from the enemy.

[2] SA is referred to Selective Availability. Its purpose was to degrade the performance of the signal for the civil users. The SA was deactivated on 2 May 2000.

[3] frequency in the band of 1-2 GHz

locations around the world in longitude. They are unmanned and are operated remotely from the Master Control Station. They are equipped with GPS receivers with cesium standards, meteorological instruments, and communication gear to transmit the measurement to the Master Station via ground and satellite links. *Ground antennas* co-located with some of the monitor stations. They communicate with the satellites via S-band[4] radio links and are also operated remotely from the Master Control Station, to receive telemetry from the satellites on the status of its subsystems and function, to uplink commands, and to upload data to update the navigation message broadcast by the satellites.

- The last segment is the **User Segment**. It is typically referred to as a GPS receiver, processing the L-band signals transmitted from the satellites to determine the PVT (Position,Velocity, and Time). Today they are embedded in many items such as cellular telephones, PDAs, and automobiles. The legacy PPS receivers generally track C/A code on L1, then transition to P(Y) code on both L1 and L2. On the other hand, the legacy SPS receivers can track only C/A code on L1. The receivers for the modernization signal called YMCA perform the acquisition on M-code signal directly and the dual frequency is enabled. Forthcoming L1C, L2C, and L5 receivers will track signals on the respective frequency. For more details of this section please see [1], [2], [14].

2.2 Signals

GPS satellites transmit the signals using radio frequencies called L1 and L2. They are frequencies in the L-band, covering frequency between 1 GHz and 2 GHz. The center frequency of L1 is *1575.42 MHz* and of L2 is *1227.60 MHz.* Actually the satellites transmit two on other frequencies called L3 and L4, which are used for the nuclear detection system (NDS) and the NDS analysis package (NAP). The L5 transmits at a center frequency of *1176.450 MHz.* The used L5 band is located on the same band of the military services for information and transmission, distance measuring equipment (DME) and the tactical air navigation (TACAN) for aeronautical use.

There are 3 signals transmitted on L1, named coarse/acquisition (C/A) code for civil users, precision (P(Y)) for the DoD authorized users, and Military (M). The signals L1Cd, L1Cp will be in modernization plan. The signal on L2 named P is for the DoD-authorized users. The other new signals on L2 for the BIIR-M satellites are L2C and M. The new signals L5I and L5Q will be transmitted on L5. Each signal consists of three components

- **Carrier**: RF sinusoidal signal with frequency f_{L1} or f_{L2} or f_{L5}.
- **Ranging code**: a unique sequence of 0s and 1s assigned to each satellite. The code is called pseudo-random noise sequence or PRN codes. The main benefit of using PRN spread spectrum is that the satellites can transmit their signals continuously without time sharing or offset at the same frequency without interfering each other, because the PRN codes are orthogonal to each other, which can be seen by weak cross-correlation function. Therefore each satellite can be distinguished by its code. The PRN code is nearly uncorrelated with itself except for zero shifts, which can be seen from auto-correlation function with steep side lobes. This enables the receiver to measure the code phase with high precision and to distinguish the signal from multipath signals of more delay than one chip width.

[4] frequency band of 2-4 GHz

– The PRN for a C/A code is a sequence of 1,023 chips, which is repeated each millisecond. Its chipping rate is 1.023 MHz (Mcps). From the chip rate we can tell that the null-to-null bandwidth is 2.046 MHz (two times code rate) which is much greater than the bandwidth required for the data messages, therefore it is said that PRN sequences spread the code spectrum.
The C/A code is a Gold code generated by two 10 bits linear feedback shift register (LFSR). The characteristic polynomial is

$$G_1 = 1 + x^3 + x^{10} \tag{2.3}$$

$$G_2 = 1 + x^2 + x^3 + x^6 + x^8 + x^9 + x^{10} \tag{2.4}$$

with the initial state of 1 to each register. The G_2 sequence is delayed by an integer number of chips τ to produce unique code sequence as can be seen in figure 2.2.

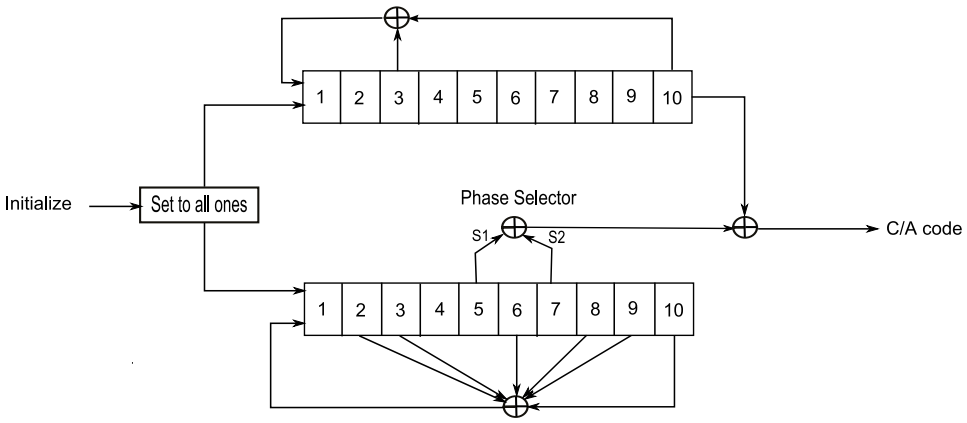

Figure 2.2: C/A PRN code generator (Source [1])

– The PRN for a P(Y) code is encrypted and very long about 10^{14} chips. Its chip rate is 10.23 Mcps or about 38.058 weeks long, which is partitioned into 37 segments of period 1 week. It is generated by four 12-bit LFSR, which are regularly short cycled to their initial state (more detail see [14]). The long period of P(Y) code makes the acquisition not easy without a priori information. Consequently the C/A code is used first for the coarse acquisition and then lock the information onto P(Y) code by the military receiver.
– The PRN for L2C code is composed of the L2CM and L2CL. Both signals are generated with the same 27-stage LFSR with different initial load of register. The L2CM register is reset every 10,230 chips, therefore the code has a period of 10,230 chips or 20 ms. Then it is modulated with navigation message of 25 bps, which forward error correction convolution (FEC) encode with rate 1/2 to 50 bps stream. The L2CL is the 75 times longer with the period of $767,250$ chips or 1.5 ms. It is used as pilot channel. The pilot channel is a channel without data message used to enhance the operation at low signal to noise ratio (SNR). Each code has 511.5 kbps chipping rate. L2CM and L2CL are two balanced code with the same number of ones and zeros and time multiplexed to the 1.023 Mpcs L2C-code, which at last BPSK modulated on to L2 frequency.
– The PRN for M code are planned to offer higher performance and security. They are transmitted at higher power without interfering with C/A and P(Y) code in the same band. They

are modulated to L1 and L2 carrier frequency using BOCs(10,5) modulation scheme. The meaning of BOCs(10,5) is, that it is a binary offset carrier signal with subcarrier frequency 10.23 MHz, and spreading code rate of 5.115 MHz (see Chapter 4 for details of BOC). Because of the higher rate the spreading code of the M signals power occurs at higher frequency and does not degrade the performance of P(Y) and C/A receivers. The acquisition for M code is designed to be autonomous, so that the receiver can acquire the M code without access to C/A or P(Y), therefore M code is more robust against jamming[5][11].

– The L5C codes are planned to be used for safety of life application and for civil uses. They are composed of L5I (in-phase) modulated with navigation message and L5Q (quadrature) used as pilot channel without time multiplexing. These codes are QPSK modulated to carrier frequency. The code rate has been specified to 10.23 Mcps and the period is $10,230$ chips for 1 millisecond. The PRN codes are generated from a pair of M sequence generator, which are

$$G_1 = 1 + x^9 + x^{10} + x^{12} + x^{13} \tag{2.5}$$

$$G_2 = 1 + x + x^3 + x^4 + x^6 + x^7 + x^8 + x^{12} + x^{13} \tag{2.6}$$

both with initial states of all 1s and the periods of 8191. The L5C are SV codes not Gold codes because their period of 10230 is not equal to $2^n - 1$, therefore a way to compute the end sequence is not like for Gold codes. Firstly the G_1 period is shorten to 8190, which is prime to 8191. The product of these two codes if left to their full completion would have period of $8191 \times 8190 = 67,084,290$ chips, but the initial state is reset after 10,230 chips, for the first generator it is reset to all 1 and the second generator it is reset to initial state k. Therefore the family of codes can be generated by varying the initial state of the second generator k as

$$G_k = G10230_1 \times G10230_2(k) \tag{2.7}$$

– The L1C code is planned to be the modernized civil signal on L1 block III composed of L1Cd data channel and L1Cp pilot channel. In an agreement between US government and European Commission, it was decided to use BOCs(1,1) modulation as baseline, but there is also further recommendation on using MBOC(6,1,1/11) [2].

- **Navigation data**: a binary code message consisting of data on the satellite health status, ephemeris (satellite position and velocity), clock bias parameters and an almanac (reduced-precision ephemeris data). The data rate is low just about 20 ms per bits (50 bps) compared to the chipping rate, to guarantee a low bit error rate (BER).

Each PRN code is combined with the navigation data using modulo-2 addition. Thereafter the code is modulated with the carrier. Normally, the code is modulated with binary phase shift keying (BPSK), in which the symbol 0 maps to 1 and symbol 1 maps to -1 or if the signal state change such as 1 to -1 and vice versa, the phase of the carrier is shifted by π. But in the modernization plan some signals are also modulated with BOC.

Two signals on L1 which are P(Y) and C/A are modulated on in-phase and quadrature (shifting in-phase by 90^{o}) components respectively. The signal from kth satellite can be modeled as

[5] operation of drowning the navigation signals in high power signals to cause loss of lock and avoid reacquisition

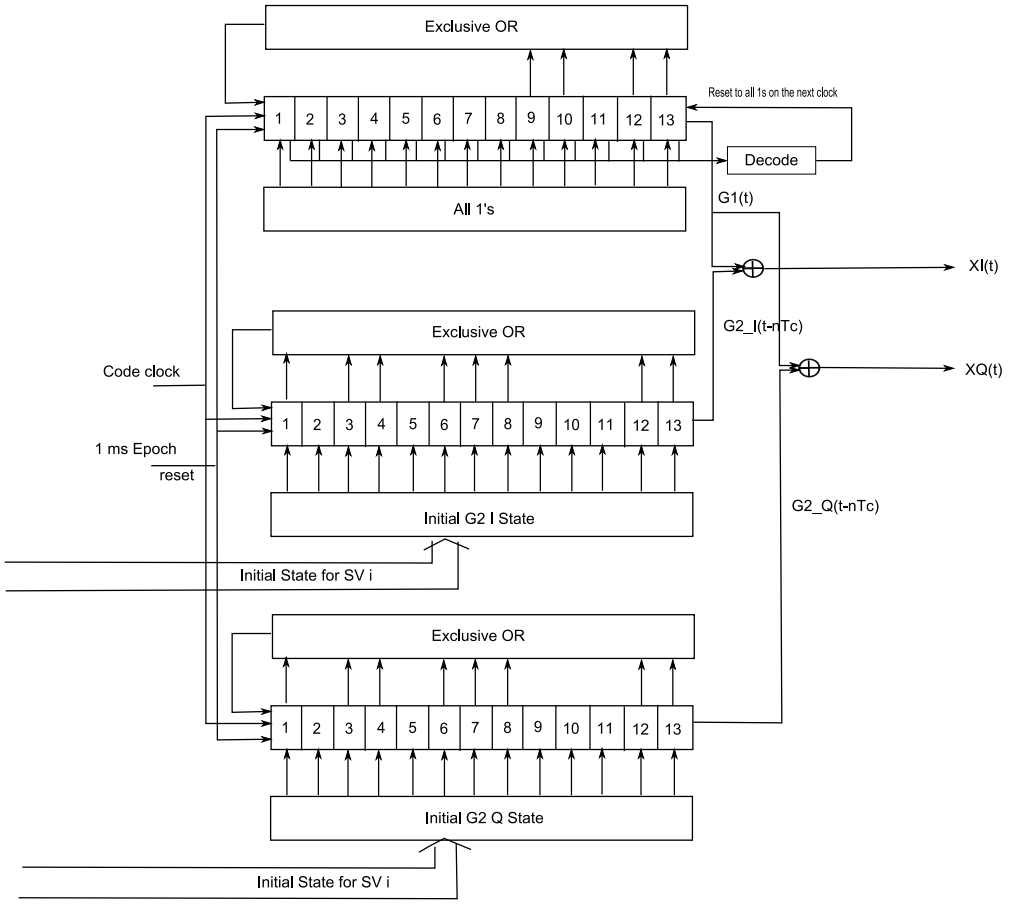

Figure 2.3: L5 PRN code generator (Source [16])

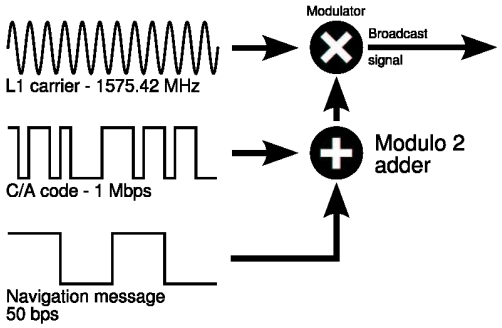

Figure 2.4: GPS L1 signal modulation scheme (Source [37])

$$
\begin{aligned}
s_{L1}^{(k)}(t) = & \sqrt{2P_C}x^{(k)}(t)D^{(k)}(t)\cos(2\pi f_{L1}t + \theta_{L1}) \\
& + \sqrt{2P_{Y1}}y^{(k)}(t)D^{(k)}(t)\sin(2\pi f_{L1}t + \theta_{L1}) \\
& + \text{new military M code} \\
& + \text{new L1C civil code}
\end{aligned}
\tag{2.8}
$$

where P_C and P_{Y1} are signal power for signal carrying C/A and P(Y) codes respectively; $x(k)$ and $y(k)$ are the C/A and P(Y) PRN code sequences assigned to satellite number k; $D(k)$ denotes

the navigation data bit stream; f_{L1} is the carrier frequencies of L1; and θ_{L1} is phase offset. The modulated C/A signal spreads over 2 MHz, P(Y) signal spreads around 20 MHz and centered at the carrier frequency. They can be de-spread later at a receiver, if the ranging code is known.

The signals for L2 can be modeled as

$$\begin{aligned} s_{L2}^{(k)}(t) = & \sqrt{2P_Y} y^{(k)}(t) D^{(k)}(t) \sin(2\pi f_{L2} t + \theta_{L2}) \\ & + \sqrt{2P_c} RC^{(k)}(t) \mathcal{F}\{D_{L2}^{(k)}(t)\} \cos(2\pi f_{L2} t + \theta_{L2}) \\ & + \text{new military M code} \end{aligned} \tag{2.9}$$

whereas RC means replacement code, which can be L2CM or L2CL. The first component contains the existing Y component. The second line contains the new signal at L2 and the third line is for military code. The $F\{D(t)\}$ means Forward Error Correction encoding [3].

A new civil signal planned for L5 can be described mathematically as

$$\begin{aligned} s_{L5}^{(k)}(t) = & \sqrt{2P_G} NH_{10}(t) g_1^{(k)}(t) \mathcal{F}\{D^{(k)}(t)\} \cos(2\pi f_{L5} t + \theta_{L5}) \\ & + \sqrt{2P_G} NH_{20}(t) g_2^{(k)}(t) \sin(2\pi f_{L5} t + \theta_{L5}) \end{aligned} \tag{2.10}$$

whereas $g_1(t)$ and $g_2(t)$ are ranging code of 10,230 chips long for in-phase and quadrature component respectively. NH means Neumann-Hoff codes modulated to extend the length of $g_1(t)$ to 102,300 chips and $g_2(t)$ to 204,600 chips. The data bits are coded with forward error correction convolution code (FEC) to improve BER, the output of the rate 1/2 code data is 100 bps. The $NH_{10}(t)g_1(t)$ code period is 10 ms long equal to the duration of FEC navigation bits, while the $NH_{20}(t)g_2(t)$ has period of 20 ms. The $NH_{10}(t)$ sequence of 0000110101 and $NH_{20}(t)$ sequence of 00000100110101001110 are modulo-2 added to the in-phase and quadrature component respectively. The codes have minimal autocorrelation side lobes, improve cross correlation side lobes of PRN signal, resolve the bit timing clock, and reduces the spectral density to 100 or 50 Hz space line components instead of 1 kHz spacing [12],[16].

The improvement of the new signals on L2 and L5 over the existing civil signals on L1 can be concluded as [3]

- Faster signal on L5 of 10.23 MHz make the main peak in auto correlation function sharper by factor of 10, which improve the noise performance. The chip width is decreased; therefore the multipath with less delay can be distinguished.
- Longer codes on L2 and L5 produce lower correlation function side lobes, which reduce the probability of false lock during signal acquisition.
- Forward error correction (FEC) used to corrected bit decision error suffered while demodulating the data message.
- Data-free channel or Pilot channel improves performance in low SNR environment. Since the navigation bits are not known a-priori, the received bit must be squared to strip the navigation codes, which also generate the quarrying loss due to noise. With the pilot channel, the ranging code can be obtained directly.

2.3 Spectral Analysis

- The analysis of C/A code from [1] firstly ignoring the data modulation and setting the phase offset to zero

$$s_1(t) = \sqrt{2P_c} x(t) \cos(2\pi f_{L1} t) \tag{2.11}$$

Then Fourier transforms the signal as

$$\mathcal{F}\{\sqrt{2P_c}x(t)\cos(2\pi f_{L1}t)\} = \frac{\sqrt{P_c}}{2}X(f-f_{L1}) + \frac{\sqrt{P_c}}{2}X(f+f_{L1}) \tag{2.12}$$

The spectrum of the ranging code $X(f)$ is approximated by considering only one period of the code

$$\begin{aligned}
\mathcal{F}\{x_1(t)\} &= \mathcal{F}\{p(\frac{t}{T_c})\sum_{n=0}^{N-1}x_n\delta(t-T_c)\} \\
&= \mathcal{F}\{p(\frac{t}{T_c})\}\mathcal{F}\{\sum_{n=0}^{N-1}x_n\delta(t-T_c)\} \\
&= T_cP(fT_c)\int_{-\infty}^{\infty}\sum_{n=0}^{N-1}x_n\delta(t-nT_c)\exp(-j2\pi ft)dt \\
&= T_cP(fT_c)\sum_{n=0}^{N-1}x_n\exp(-j2\pi fnT_c) \\
&= T_c\sqrt{N}P(fT_c)\frac{1}{\sqrt{N}}\sum_{n=0}^{N-1}x_n\exp(-j2\pi fnT_c) \\
&= T_c\sqrt{N}\mathrm{sinc}(\pi fT_c)X_{code}(f)
\end{aligned} \tag{2.13}$$

whereas $P(f)$ is the Fourier transform of the rectangular chip waveform, and $X_{code}(f)$ is the Fourier transform of the code $x_{n=0}^{N-1}$

$$X_{code}(f) = \frac{1}{\sqrt{N}}\sum_{n=0}^{N-1}x_n\exp(-j2\pi fnT_c) \tag{2.14}$$

The spectrum of a chip waveform is the sinc function. It takes a maximum value at $f=0$ and fall to 0 at $1/Tc$, therefore the null-to-null bandwidth is $2/Tc$, which is 2.046 MHz for C/A code. Combining carrier and ranging code results

$$\begin{aligned}
\mathcal{F}\{\sqrt{2P_c}x(t)\cos(2\pi f_{L1}t)\} = &\sqrt{\frac{P_cN}{2}}T_c\mathrm{sinc}(\pi(f-f_{L1})T_c)X_{code}(f-f_{L1}) \\
&+\sqrt{\frac{P_cN}{2}}T_c\mathrm{sinc}(\pi(f+f_{L1})T_c)X_{code}(f+f_{L1})
\end{aligned} \tag{2.15}$$

The shape of sinc function after carrier modulated is centered at f_{L1} and $-f_{L1}$.

- For the long ranging codes like in P(Y), the signal can be assumed as random. Therefore the energy is infinite, and there exists no Fourier transformation. Hence the **Power Spectral Density PSD)** is defined [1] as

$$S_Y(f) = \lim_{T\to\infty}\frac{E\{|Y_T(f,\xi)|^2\}}{T} \tag{2.16}$$

whereas $T = NT_C$ and N approach infinity then $T \to \infty$

$$|Y_T(f,\xi)|^2 = T_C^2 N \text{sinc}^2(\pi f T_C)|Y_{code}(f)|^2 \tag{2.17}$$

Only Y_{code} contains random variable then

$$E\{|Y_T(f,\xi)|^2\} = T_C^2 N \text{sinc}^2(\pi f T_C) E\{|Y_{code}(f)|^2\} \tag{2.18}$$

And the expectation of Y_{code} can be derived as

$$\begin{aligned} E\{|Y_{code}(f)|^2\} &= \frac{1}{N} E\{\sum_{m=0}^{N-1}\sum_{n=0}^{N-1} y_n \exp(-j2\pi f n T_C) y_m \exp(j2\pi f m T_C)\} \\ &= \frac{1}{N}\sum_{m=0}^{N-1}\sum_{n=0}^{N-1} E\{y_n y_m\} \exp(-j2\pi f(n-m)T_C) \\ &= \frac{1}{N}\sum_{n=0}^{N-1} \exp(-j2\pi f(n-n)T_C) \\ &= 1 \end{aligned} \tag{2.19}$$

Therefore

$$E\{|Y_T(f,\xi)|^2\} = T_C^2 N \text{sinc}^2(\pi f T_C) \tag{2.20}$$

And the PSD denotes

$$S_Y(f) = T_C \text{sinc}^2(\pi f T_C) \tag{2.21}$$

At last PSD with carrier modulated

$$S_Y(f) = \frac{T_C}{2}(\text{sinc}^2(\pi(f-f_L)T_C) + \text{sinc}^2(\pi(f+f_L)T_C)) \tag{2.22}$$

- The power spectral density of the short C/A ranging code, of which the period repeats twenty time per one navigation bit $T_b = 20NT_C$, is complicate to derive. Therefore it is only the last result shown (for derivation please see [1]).

$$\begin{aligned} S_{C/A}(f) &= \frac{T_B}{(NT_C)^2}|X_1(f)|^2 \sum_{l=-\infty}^{\infty} \text{sinc}^2(\pi T_B(f - \frac{l}{NT_C})) \\ \text{where} \quad |X_1(f)|^2 &= T_C^2 N \text{sinc}^2(\pi f T_C)|X_{code}(f)|^2 \end{aligned} \tag{2.23}$$

The PSD of the C/A code without carrier modulated consists of the $\text{sinc}^2(\pi f T_C)$ due to ranging code chips, $|X_{code}(f)|^2$ due to the repetition of ranging code, and the last sum term due to the repetition of data bits.

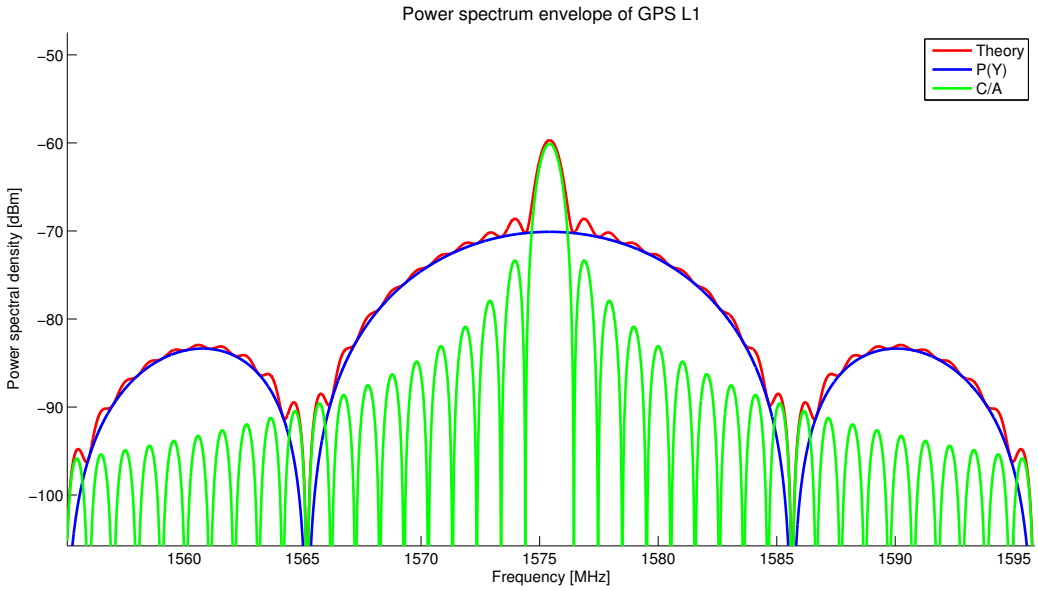

Figure 2.5: Generated envelope of power spectrum of GPS L1 for BIIA and BIIR satellites (uncalibrated)

Figure 2.5 shows the envelope of power spectrum of the old GPS L1 signal. For old GPS L2 signal there is no C/A code.

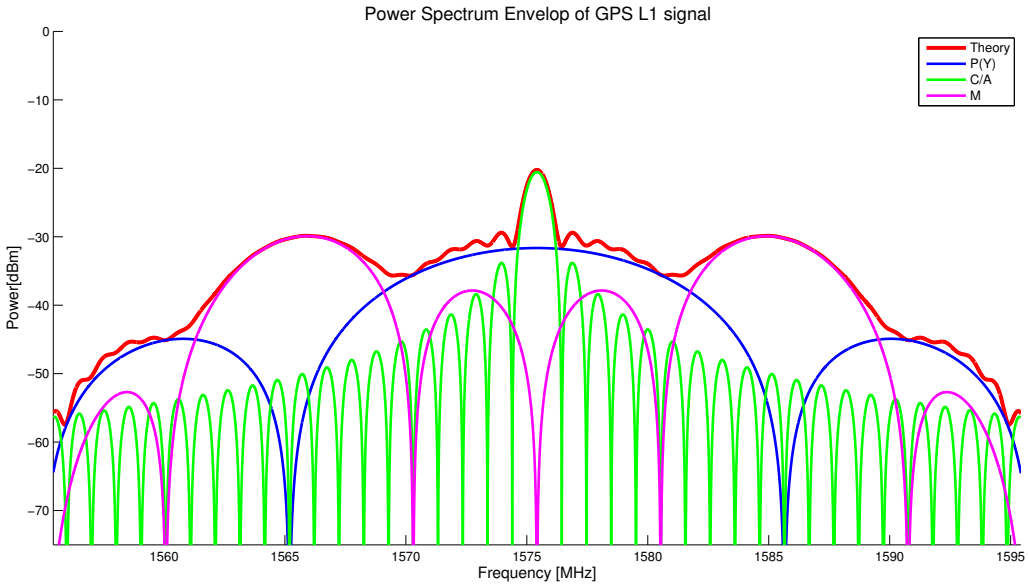

Figure 2.6: Generated envelope of power spectrum of GPS L1 for BIIRM satellites (uncalibrated)

Figure 2.6 shows the envelope of power spectrum of the GPS block BIIRM L1 signal which include military signal. For GPS block BIIRM L2 it looks the same but the center is located at the other frequency.

3. Signal Power and Correlation Function

3.1 Energy of the Signal

The analysis of the signal energy and power are considered separately depending on the characteristic of the signal. The facts from this section are derived from [17].

- The energy of the continuous-time aperiodic signal has finite energy, therefore it can be expressed according to Parseval's theorem as

$$E = \int_{-\infty}^{\infty} s^2(t)dt = \int_{-\infty}^{\infty} |S(f)|^2 df \tag{3.1}$$

  whereas $s(t)$ denotes signal in time domain, which represented by superposition of trigonometry functions of different phase, amplitude and frequency.

$$S(f) = \int_{-\infty}^{\infty} s(t)e^{-j2\pi ft}dt \tag{3.2}$$

  implies the Fourier transformation for aperiodic continuous signals. The term $|S(f)|^2$ indicates the power spectral density (PSD) in unit of Watt or commonly used in dBW. The term is named as $G(F)$ in the following text.
- The continuous time periodic signal has infinite energy, which will not be expressed in energy term. However the expression of average power is used

$$P = \frac{1}{T_p}\int_{T_p} s(t)^2 dt = \sum_{k=-\infty}^{\infty} |c_k|^2 \tag{3.3}$$

  whereas

$$c_k = \frac{1}{T_p}\int_{T_p} s(t)e^{-j2\pi kF_0 t}dt \tag{3.4}$$

  denotes Fourier series coefficient of kth harmonic component of the signal. T_p is the fundamental period of the signal, $F_0 = \frac{1}{T_p}$ is fundamental frequency. The term $|c_k|^2$ also denotes the power spectral density.
- The energy of discrete time aperiodic signal is

$$E = \sum_{n=-\infty}^{\infty} |s(n)|^2 = \frac{1}{2\pi}\int_{-\pi}^{\pi} |S(\omega)|^2 d\omega \tag{3.5}$$

  whereas

$$S(\omega) = \sum_{n=-\infty}^{\infty} s(n)e^{-j\omega n} \tag{3.6}$$

  is periodic function with period 2π.

- The energy of discrete time periodic signal is

$$E = \sum_{n=0}^{N-1} |s(n)|^2 = N \sum_{k=0}^{N-1} |c_k|^2 \tag{3.7}$$

and its power is

$$P = \frac{1}{N} \sum_{n=0}^{N-1} |s(n)|^2 = \sum_{k=0}^{N-1} |c_k|^2 \tag{3.8}$$

whereas

$$c_k = \frac{1}{N} \sum_{n=0}^{N-1} s(n) e^{-j2\pi kn/N} \tag{3.9}$$

N denotes the fundamental period, and c_k composed of N frequency components separated by $2\pi/N$ radians. c_k is a periodic sequence with fundamental period N, therefore $c_{k+N} = c_k$. The term $\frac{2\pi k}{N}$ can be denoted as ω_k

3.2 Correlation Property

The (cross-) correlation function is defined by

$$R(\tau) = \int_{-\infty}^{\infty} s_1(t) s_2(t+\tau) dt \tag{3.10}$$

The correlation function of two periodic signals both with period T is defined by

$$R(\tau) = \int_{0}^{T} s_1(t) s_2(t+\tau) dt \tag{3.11}$$

The function describes the degree of correspondence of two signals $s_1(t)$ and $s_2(t)$ as a function of the time shift τ between them. If $s_1 = s_2$, then the function is called autocorrelation function (ACF). The ACF is an even function with $R(\tau) = R(-\tau)$. At $\tau = 0$ this function corresponds to the Energy of the signal

$$E = R(0) = \int_{-\infty}^{\infty} s^2(t) dt = \int_{-\infty}^{\infty} |S(f)|^2 df \tag{3.12}$$

The power spectral density $G(f)$ is also defined to be Fourier transform of ACF as

$$G(f) = \int_{-\infty}^{\infty} R(\tau) e^{-j2\pi f\tau} dt \tag{3.13}$$

As an example a rectangular chip with amplitude A and chip long T_c has the ACF

$$R(\tau) = \begin{cases} A^2(1 - \frac{\tau}{T_c}) & \text{for } |\tau| \leq T_c \\ 0 & \text{else} \end{cases} \tag{3.14}$$

It can be Fourier transformed into

$$G(f) = A^2 T_c \text{sinc}^2(\pi f T_c) \tag{3.15}$$

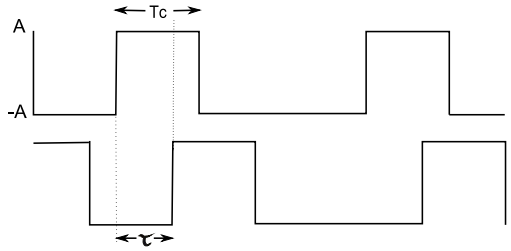

Figure 3.1: A random binary code

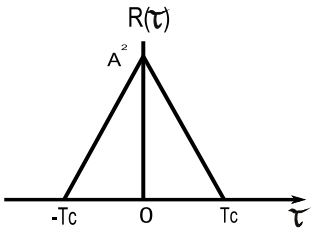

Figure 3.2: Autocorrelation function

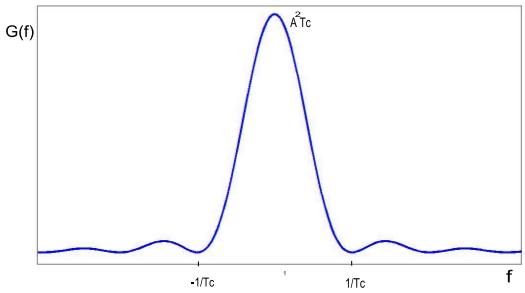

Figure 3.3: Power spectrum of random binary signal

Figure 3.1- 3.3 illustrate the results.

Now the PRN code generated using n bits LSFR is determined. The longest code sequence that can be produced before the output repeats is $N = 2^n - 1$, whereas this sequence refers to a maximum length code (M-sequence). The autocorrelation function of this code is the infinite series of triangular function with period NT_c, the correlation amplitudes outside the correlation interval are $-A^2/N$. The power spectral density has the same envelope like from figure 3.3 but there are line spectrum with spacing $1/NT_C$ due to the Fourier transform of periodicity characteristic, and the spectrum line at zero frequency is smaller than the envelope [14].

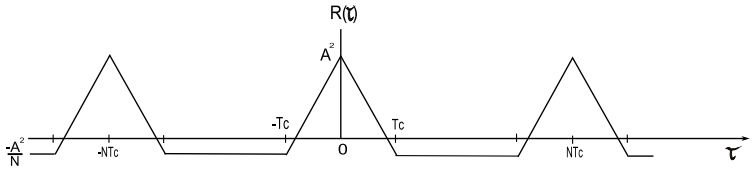

Figure 3.4: ACF of the PRN with maximum code length sequence

The M-sequence is not suitable to be used as a ranging code for GNSS signals because of the limited number of usable code and poor cross-correlation properties between different codes. Moreover, this sequence has side lobes for a short integration time (a few periods of code), which leads to false lock of correlation peak. For this reason, the Gold code is employed for GNSS ranging code. The autocorrelation function of GPS C/A, which is a Gold code of 10 chips LSFR, is shown in figure 3.5. It can be seen that it is not the uniform minimum correlation in the interval between the correlation intervals like in M-sequence, which is due to the imperfection of clock synchronization of two LSFR register[14].

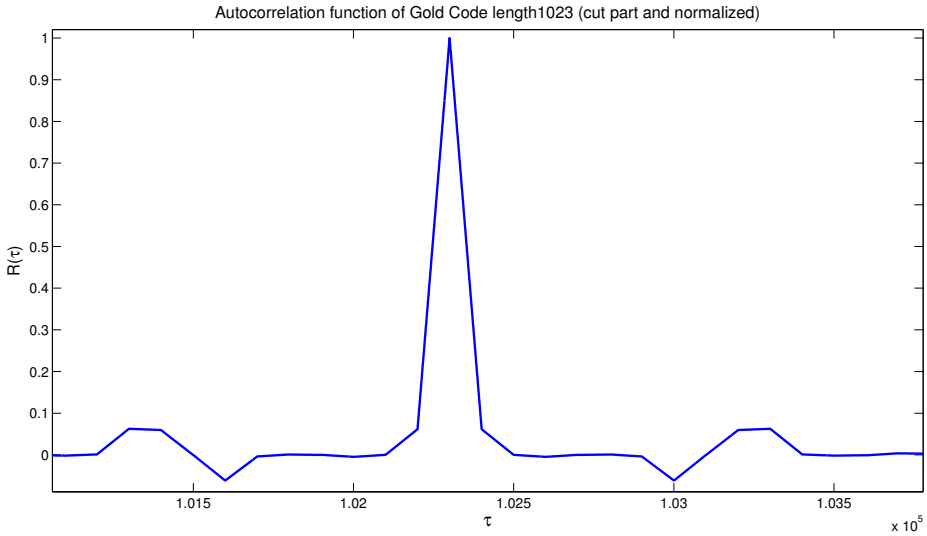

Figure 3.5: ACF of C/A code (cut part)

There is another method to derive the correlation function of discrete time signals called circular correlation described by [18]. Firstly the discrete time convolution of a system is introduced

$$y(n) = \sum_{m=0}^{N-1} x(m)h(n-m) \tag{3.16}$$

where $x(m)$ is an input signal and $h(n-m)$ is system response, whereas $h(n-m)$ is circular because the discrete operation is periodic. By taking the DFT of the equation results

$$\begin{aligned} Y(k) &= \sum_{n=0}^{N-1}\sum_{m=0}^{N-1} x(m)h(n-m)e^{(-j2\pi kn)/N} \\ &= \sum_{m=0}^{N-1} x(m)[\sum_{n=0}^{N-1} h(n-m)e^{(-j2\pi k(n-m))/N}]e^{(-j2\pi km)/N} \\ &= H(k)\sum_{m=0}^{N-1} x(m)e^{(-j2\pi km)/N} \\ &= X(k)H(k) \end{aligned} \tag{3.17}$$

This result is only for periodic convolution with N points output. It is not same as the linear convolution that has $2N-1$ points output. For correlation function of two discrete signals can be

written as

$$z(n) = \sum_{m=0}^{N-1} x(m)h(n+m) \tag{3.18}$$

whereas $h(n)$ denotes another signal. Thereafter the DFT is performed

$$\begin{aligned} Z(k) &= \sum_{n=0}^{N-1}\sum_{m=0}^{N-1} x(m)h(n+m)e^{(-j2\pi kn)/N} \\ &= \sum_{m=0}^{N-1} x(m)[\sum_{n=0}^{N-1} h(n+m)e^{(-j2\pi k(n+m))/N}]e^{(j2\pi km)/N} \\ &= H(k)\sum_{m=0}^{N-1} x(m)e^{(j2\pi km)/N} \\ &= H(k)X^{-1}(k) = H^{-1}(k)X(k) \end{aligned} \tag{3.19}$$

whereas $H^{-1}(k)$ represents the inverse DFT. If the $x(n)$ signal is real, $x(n) = x(n)^*$ where $*$ is the complex conjugate. Using this relation we get

$$|Z(k)| = |H^*(k)X(k)| = |H(k)X^*(k)| \tag{3.20}$$

and the correlation function denotes

$$R(m) = \mathcal{DFT}^{-1}(|H^*(k)X(k)|) = \mathcal{DFT}^{-1}(|H(k)X^*(k)|) \tag{3.21}$$

The circular correlation can reduced the computational time against the serial correlation.

The correlation function is fundamental for demodulation of GNSS signals. The acquisition correlates between the received signal and the locally generated replica and then search for the peak of the correlation to determine the Doppler frequency and code phase. The searching of the maximum correlation can be mathematically formulated as

$$\max_{\theta} R(\theta|r) \tag{3.22}$$

whereas R is the correlation function, θ is frequency or code phase.

The power spectral density, which is derived through Fourier transform of correlation function, is also a useful function to determine the channel bandwidth required to transmit the spread spectrum signal.

After the maximum correlation is found, the receiver switches to the tracking loop, which is mathematically formulated as

$$\frac{dR(\theta|r)}{d\theta} = 0 \tag{3.23}$$

The function is called **discriminator** function. This function is operated in different ways, the common notation for code tracking is

$$\frac{dR(\tau)}{d\tau} = \frac{R(\tau + \frac{d}{2}T_c) - R(\tau - \frac{d}{2}T_c)}{dT_c} \tag{3.24}$$

which is a result of early minus late correlation, whereas d denotes the correlation spacing.

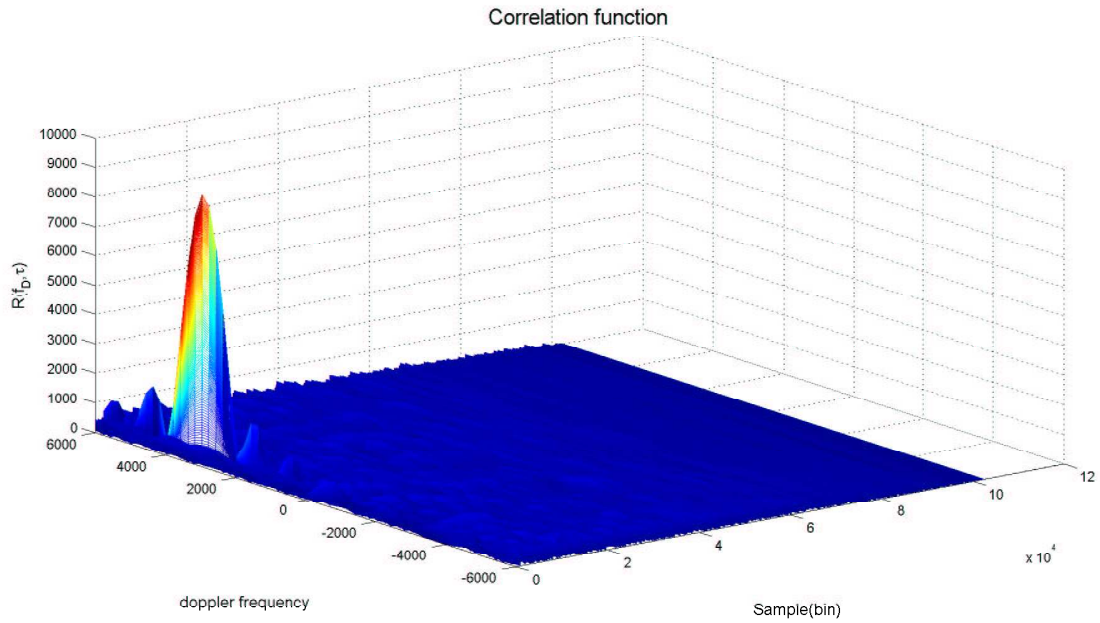

Figure 3.6: 2 dimensional correlation function of a measurement with generated PRN code

The discriminator function can detect the correlation peak with more accuracy than in searching operation, because the autocorrelation peak is normally deformed by noise and in band interference, furthermore the sharp peak is rounded due to filtering out the high frequency components. There is also a fact from many literatures that the narrow correlator spacing helps reducing the multipath interference [1], [2].

3.3 Correlation Peak Deformation

The correlation threats scenario for GPS L1 C/A signal agreed by the International Civil Aviation Organization (IC/AO) is called '2nd-Order Step' based model [19],[20]. It is composed of 3 parameters which are f_d (damped natural frequency), σ (damping), and Δ (lead/lag), whereas $\sigma = \zeta\omega_0$ (the product of the damping ratio ζ and the natural frequency ω_0) and $f_d = \frac{1}{2\pi}\sqrt{1-\zeta^2}$. The model is separated into 3 types as

- Digital: causes a shift in correlation peak, therefore the model included only Δ. It is caused by code modulation imperfections such as duty cycle.
- Analog: normally causes correlation peak asymmetry. This is caused by satellites filter band limiting, asymmetry and (phase) non-linearity. There is no Δ included.
- Combination: all parameters included

These 3 types of the model can be seen in figure 3.7.

3.4 Signal Power Level

The signal power received at the receiver is very weak at only about 10^{-16} Watt, thus it is more convenient to express this wide range power level in logarithmic scale, defined as

$$\left.\frac{P_1}{P_0}\right|_{dB} = 10\log\frac{P_1}{P_0} \tag{3.25}$$

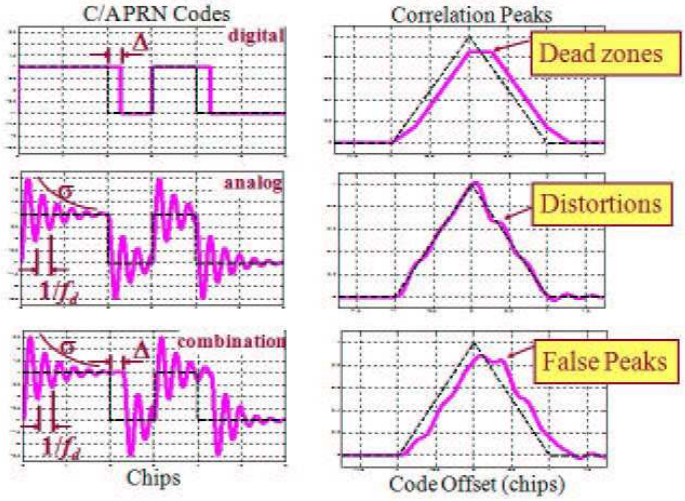

Figure 3.7: Threats model for signal deformation (Source: [20])

where P_1 and P_0 are power to be compared. Absolute value can be expressed similarly in relation to 1 watt or 1 milliwatt in unit of dBW or dBm, respectively. The received signal at 10^{-16} Watt is then equal to -160 dBW.

The antenna reactivity is described by variation of antenna gain G, which is interrelation with effective antenna area A_E

$$G = 4\pi A_E \frac{f^2}{c^2} \tag{3.26}$$

whereas f is the frequency, c is the velocity of light. G_r denotes gain of the receiver, and G_s gain of the transmitter. According to [1] the power at the receiver is

$$P_r = \frac{P_s G_s}{L_A}(\frac{\lambda}{4\pi R})^2 \qquad \text{[Watts]} \tag{3.27}$$

L_A is the power loss due to signal propagation through the atmosphere, R denotes the distance between transmitter and receiver, whereas $(\frac{4\pi R}{\lambda})^2$ determines free space loss error L. The term $P_s G_s$ is called equivalent isotropic radiated power (EIRP).

The equation that include the gain and any losses from the receiver is described as

$$C = \frac{P_s G_s G_r}{L_A L_r}(\frac{\lambda}{4\pi R})^2 = \frac{P_s G_s G_r}{L_A L_r}(\frac{c}{4\pi R f})^2 \qquad \text{[Watts]} \tag{3.28}$$

4. Code Modulation / Sub Modulation

4.1 BPSK (Binary Phase-Shift Keying)

BPSK uses two phases which are separated by 180° and so can also be termed 2-PSK. It does not particularly matter exactly where the constellation points are positioned, only that the two phases are 180° difference to each other. Figure 4.1 shows the IQ constellation of BPSK on the real axis, at 0° and 180°. This modulation is the most robust of all the PSKs since it takes serious distortion to make the demodulator reach an incorrect decision. It is, however, only able to modulate at 1 bit/symbol and so is unsuitable for high data-rate applications when bandwidth is limited [39].

The reference frequency for GNSS signal is normally f_0 = 1.023 MHz. The legacy GPS L2 signal is BPSK with chip rate 10.23 MHz denoted as BPSK(10). The power spectral density is given in equation (2.22)

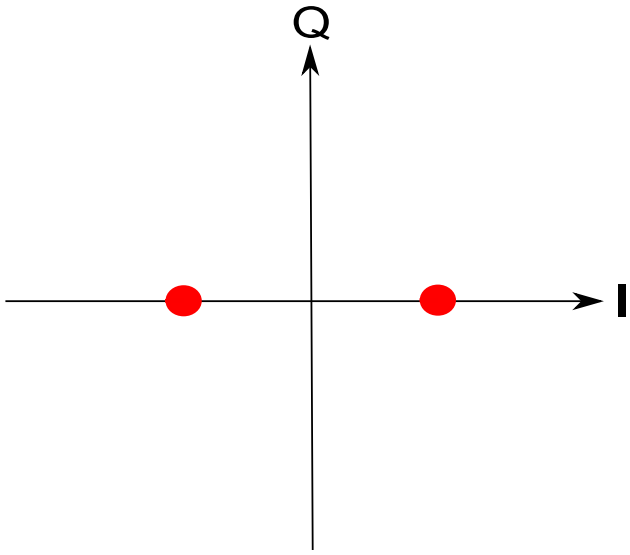

Figure 4.1: BPSK constellation

4.2 QPSK (Quadrature Phase-Shift Keying)

QPSK uses four points on the constellation diagram, equispaced around a circle. With four phases, QPSK can encode two bits per symbol, twice the rate of BPSK. This can be used either to double the data rate compared to a BPSK system while maintaining the bandwidth of the signal or to maintain the data-rate of BPSK but halve the bandwidth needed.

The legacy GPS L1 signal is QPSK modulated with C/A code chip rate of 1.023 MHz and P(Y) code chip rate of 10.23 MHz with 3dB power different .

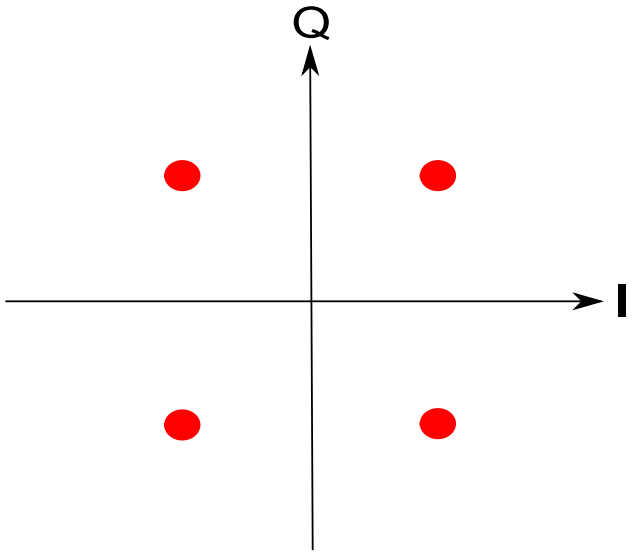

Figure 4.2: QPSK constellation

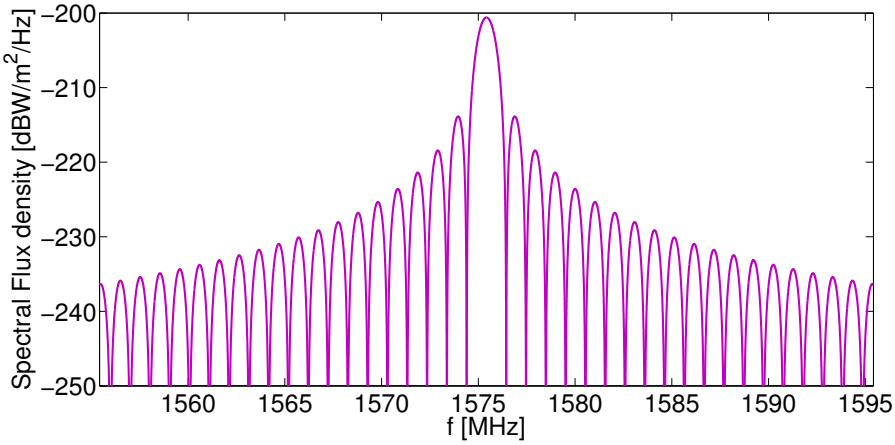

Figure 4.3: Power spectral density C/A

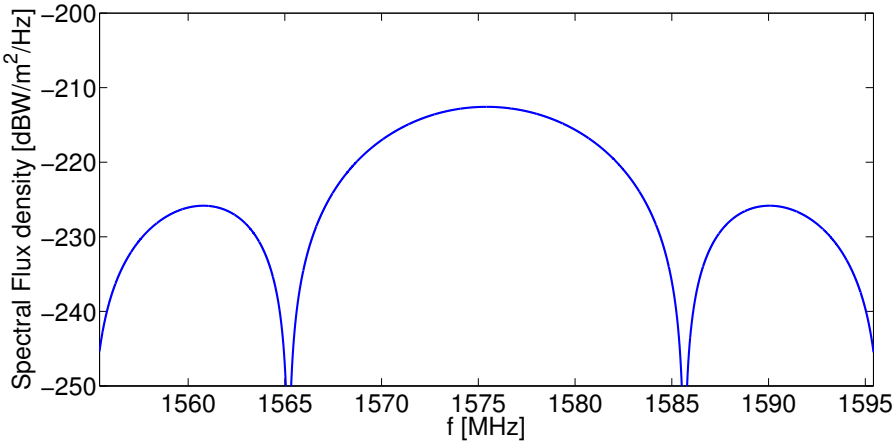

Figure 4.4: Power spectral density of P(Y)

4.3 BOC (Binary Offset Carrier)

The Binary offset carrier (BOC) modulates the PRN code with a rectangular subcarrier of frequency f_s, which splits the power spectral density main lobe of the BPSK modulation into two symmetric side lobes around the center frequency. This type of code modulation is used in the modernization planned for GPS and Europe's Galileo.

The reference frequency for GNSS signal is $f_0 = \frac{1}{T} = 1.023$ MHz and

$$T_s = \frac{T}{m} \tag{4.1}$$

$$T_c = \frac{T}{n} \tag{4.2}$$

$$k = \frac{2T_c}{T_s} \tag{4.3}$$

denotes BOC(m,n). k is positive odd or even number of half periods of the sub-carrier during one code chip. The BOC with rectangular subcarrier sine waveform is expressed as BOCs, whereas the code with rectangular subcarrier cosine waveform is expressed as BOCc.

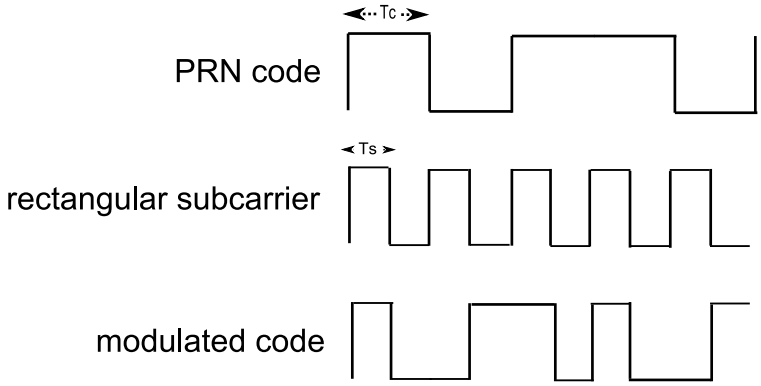

Figure 4.5: Binary offset carrier with rectangular subcarrier sine waveform modulation BOCs(1,1)

The expression of BOC signal is defined in [8] as:

$$s(t) = \exp(-i\theta) \sum_k a_k \mu_{nT_s}(t - knT_s - t_0) c_{T_s}(t - t_0) \tag{4.4}$$

where a_k is the data-modulated spreading code, $c_{T_s}(t)$ is the subcarrier-a periodic function with period $2T_s$, $\mu_{nT_s}(t)$ is a spreading symbol, here a rectangular pulse with time support equal to nT_s, and n is the number of half-periods of the subcarrier during which the spreading code value remains the same. The quantities θ and t_0 reflect arbitrary offsets in phase and time respectively.

An equivalent notation describes a bi-phase BOC modulation as a PSK modulation with unconventional spreading symbol shape, so that the complex envelope can be written as

$$s_{BOC(f_s,f_c)}(t) = \exp(-i\theta) \sum_k a_k q_{nT_s}(t - knT_s - t_0) \qquad \text{for n even} \tag{4.5}$$

$$s_{BOC(f_s,f_c)}(t) = \exp(-i\theta) \sum_k (-1)^k a_k q_{nT_s}(t - knT_s - t_0) \qquad \text{for n odd} \tag{4.6}$$

with spreading symbol

$$q_{nT_s}(t) = \sum_{m=0}^{n-1} (-1)^m \mu_{T_s}(t - mT_s) \tag{4.7}$$

so that $q_{nT_s}(t)$ consists of n half-cycle of a square wave, that is, n alternating values of $+1$ and -1. Whenever n is even, $q_{nT_s}(t)$ is a balance symbol (average value of zero).

The normalized power spectral density of signal with BOC is referred to [8]

$$G_{BOCs}(f) = \frac{1}{T_c}\left(\frac{\sin(\frac{\pi f T_c}{n})\sin(\pi f T_c)}{\pi f \cos(\frac{\pi f T_c}{n})}\right)^2 \qquad \text{for n even} \tag{4.8}$$

$$G_{BOCs}(f) = \frac{1}{T_c}\left(\frac{\sin(\frac{\pi f T_c}{n})\cos(\pi f T_c)}{\pi f \cos(\frac{\pi f T_c}{n})}\right)^2 \qquad \text{for n odd} \tag{4.9}$$

$$G_{BOCc}(f) = \frac{1}{T_c}\left(\frac{\sin(\pi f T_c)}{\pi f \cos(\frac{\pi f T_c}{n})}\{\cos(\pi f \frac{T_c}{n}) - 1\})\right)^2 \qquad \text{for n even} \tag{4.10}$$

$$G_{BOCc}(f) = \frac{1}{T_c}\left(\frac{\cos(\pi f T_c)}{\pi f \cos(\frac{\pi f T_c}{n})}\{\cos(\pi f \frac{T_c}{n}) - 1\})\right)^2 \qquad \text{for n odd} \tag{4.11}$$

It must be noted that the expression does not take into account the periodicity of PRN code used in GNSS signals, which results in spectrum lines spaced by inverse of the code period. These equations can be determined as the envelope of them.

Figure 4.7 through 4.12 show the Power Spectral Density of three different BOC modulations. As can be noticed the sum of the number of main lobes and side lobes between the main lobes is n. The zero crossing of each main lobe are spaced by twice the code rate $(2 * f_c)$ and the zero crossings of each side lobe are at code rate fc, in addition it can be noticed that the BOCc has only small side lobes around the carrier, on contrary to BOCs that has side lobes concentrated around the carrier frequency. It can be said that the BOC moves the signal power away from the band center so that more signals can be transmitted in that band with less interfering each other.

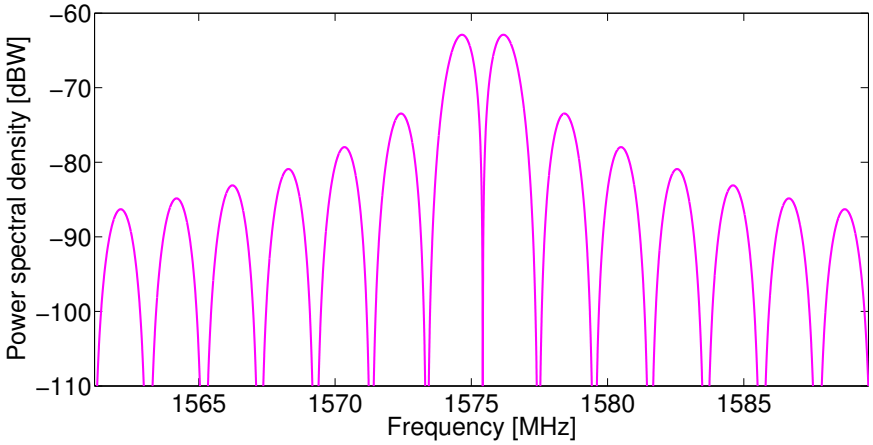

Figure 4.6: Binary offset carrier modulation of BOCs(1,1)

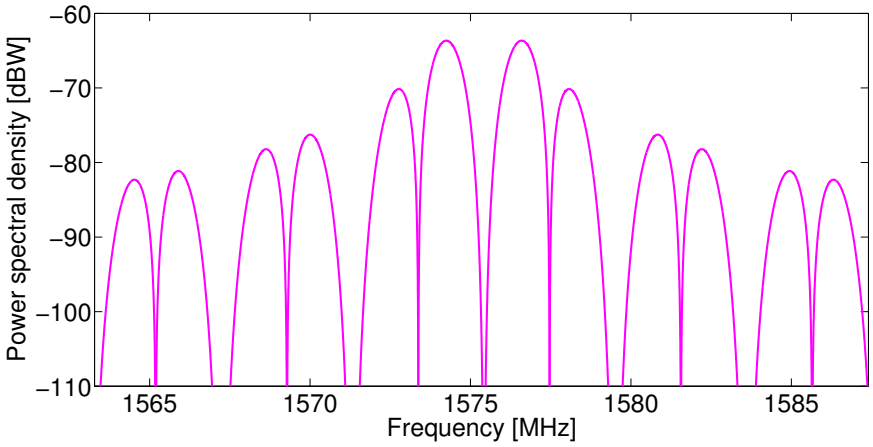

Figure 4.7: Binary offset carrier modulation of BOCc(1,1)

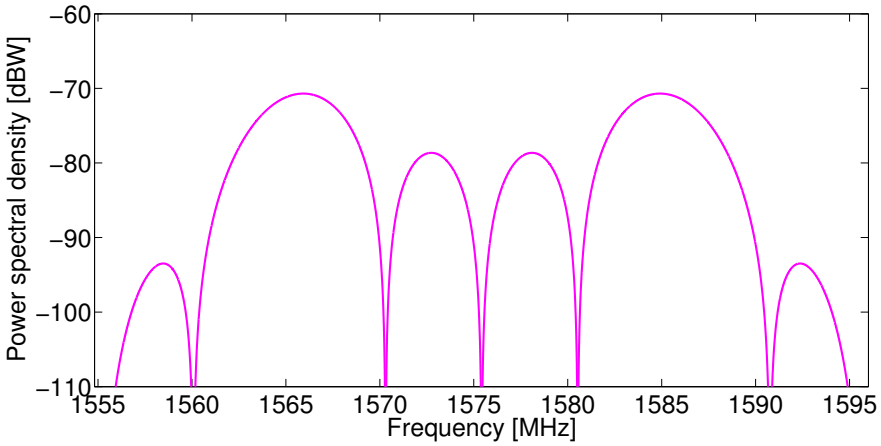

Figure 4.8: Binary offset carrier modulation of BOCs(10,5)

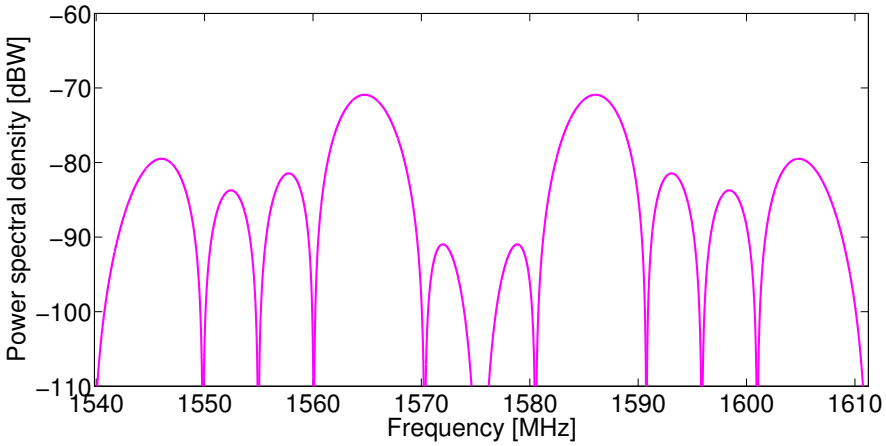

Figure 4.9: Binary offset carrier modulation of BOCc(10,5)

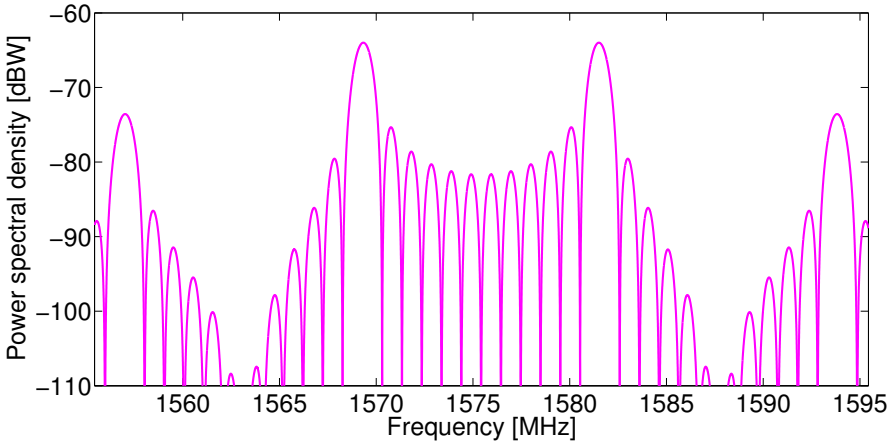

Figure 4.10: Binary offset carrier modulation of BOCs(6,1)

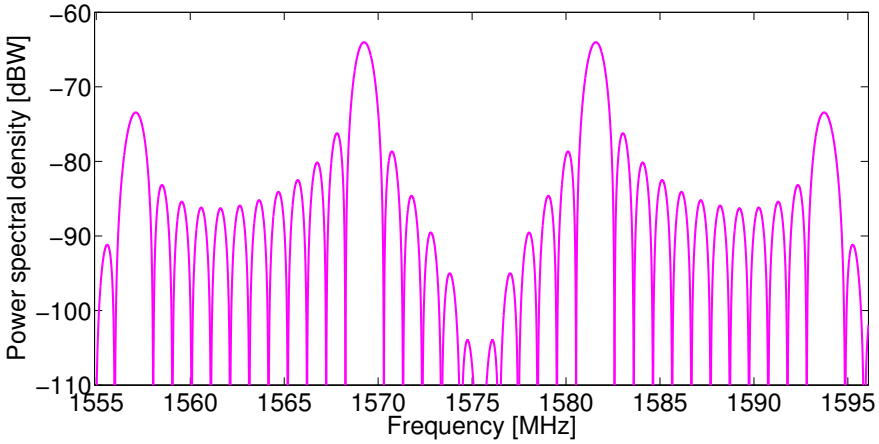

Figure 4.11: Binary offset carrier modulation of BOCc(6,1)

Some advantages of BOC modulation are better tracking performance due to the larger bandwidth, interference mitigation due to separation of the main lobes. The disadvantage of this modulation is that the auto correlation function has many maxima, the number of the peak are equal to $2n - 1$ and separated by T_s, which makes it ambiguous in acquisition.

4.4 MBOC (Multiplexed Binary Offset Carrier)

MBOC was recommended to be used in GPS L1C and Galileo L1OS, thereby a small amount of power is placed at higher frequency to improve tracking performance. The power spectral density of MBOC(6,1,1/11), which is general and have been studied extensively, reads [9]

$$G_{Signal}(f) = \frac{10}{11} G_{BOC(1,1)}(f) + \frac{1}{11} G_{BOC(6,1)}(f) \tag{4.12}$$

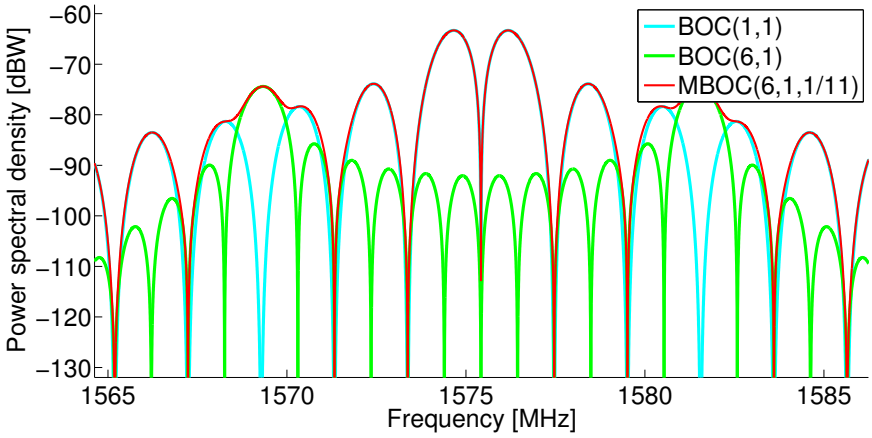

Figure 4.12: PSD of MBOC(6,1,1/11)

The time waveforms used to produce MBOC(6,1,1/11) power spectral density can be either time-multiplexed BOC (TMBOC) or composite BOC (CBOC). In case of TMBOC the pilot and data components of signal can be formed using different spreading time series, and the total signal power can be distributed differently between pilot and data components, therefore there are many different TMBOC-based implementations. The design of TMBOC placement for L1C signal is completed [9] results

$$\begin{aligned} G_{Pilot}(f) &= \frac{29}{33} G_{BOC(1,1)}(f) + \frac{4}{33} G_{BOC(6,1)}(f) \\ G_{Data}(f) &= G_{BOC(1,1)}(f) \\ G_{MBOC(6,1,1/11)}(f) &= \frac{3}{4} G_{Pilot}(f) + \frac{1}{4} G_{Data}(f) \\ &= \frac{10}{11} G_{BOC(1,1)}(f) + \frac{1}{11} G_{BOC(6,1))}(f) \end{aligned} \tag{4.13}$$

whereas 75% of the power is placed on the pilot component, 25% of the power is placed on the data component, the pilot component comprises 29/33 of BOC(1,1) and 4/33 of BOC(6,1).

5. Measurement and Processing

After the successful work of DLR in establishing the L-band receiver equipments to the 30 meter antenna and analyzing the signals as published in [23], [25] and [26], GPS signals were recorded over the last year in the L-band.

5.1 Measurement Facility

The antenna at Weilheim is 30 meters in diameter with a gain of 50 dB. This raising the navigation signals above the noise floor. The antenna has a small 3dB half-beam width of 0.5°. The antenna is a shaped Cassegrain system with an elevation over azimuth mount. The antenna has a parabolic reflector of 30 m diameter, a hyperbolic sub-reflector with a diameter of 4 meter, and the adapted L-band feed.

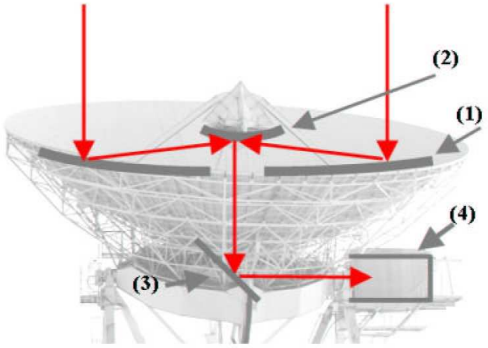

Figure 5.1: The shaped Cassegrain system : (1)parabolic reflector of 30m diameter; (2)hyperbolic sub-reflector with a diameter of 4 meter; (3)sub-reflector; (4)Cabin with feeder and measurement equipment (Source [25])

The signals are measured and recorded using a real-time vector analyzer connected to a computer capable for post-processing and storage of data. The data is processed with MATLAB.

5.2 Absolute Calibration

5.2.1 System Gain Calibration

The system gain (G_r) for the receiving path is derived from the frequency response, which is determined by a network analysis. The network analysis is connected to an electrically calibrated kit to perform remote calibration.

The calibrated pilot signal used to measure and evaluate with the real time spectrum analyzer is generated from a frequency stabilized signal generator in combination with power meter. The signal generator and power meter are coupled to the radio frequency chain using a precise calibrated coupler.

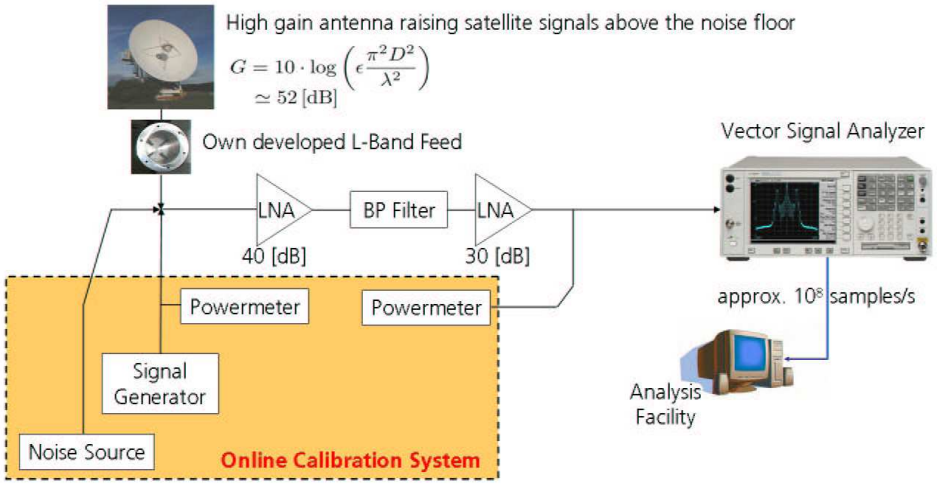

Figure 5.2: Measurement set up overview (Source [26])

5.2.2 Antenna Gain Calibration

The well known reference sources such as natural sources like radio stars or artificial sources like geostationary satellites are used to determine the antenna gain (G). The antenna gain for this 30 meters antenna is calibrated using radio star Cassiopeia A (Cass A) as the standard reference source. This star emits the strongest radio signal in the northern hemisphere and a wide range frequency enabling the calibration in a wideband. The relation between the gain of the antenna and the noise temperature of the receiving system G/T can be measured with the help of the well known flux density of Cass A. Figure 5.3 shows the resulting antenna gain. Details of the measurement and calibration set up are given in [25].

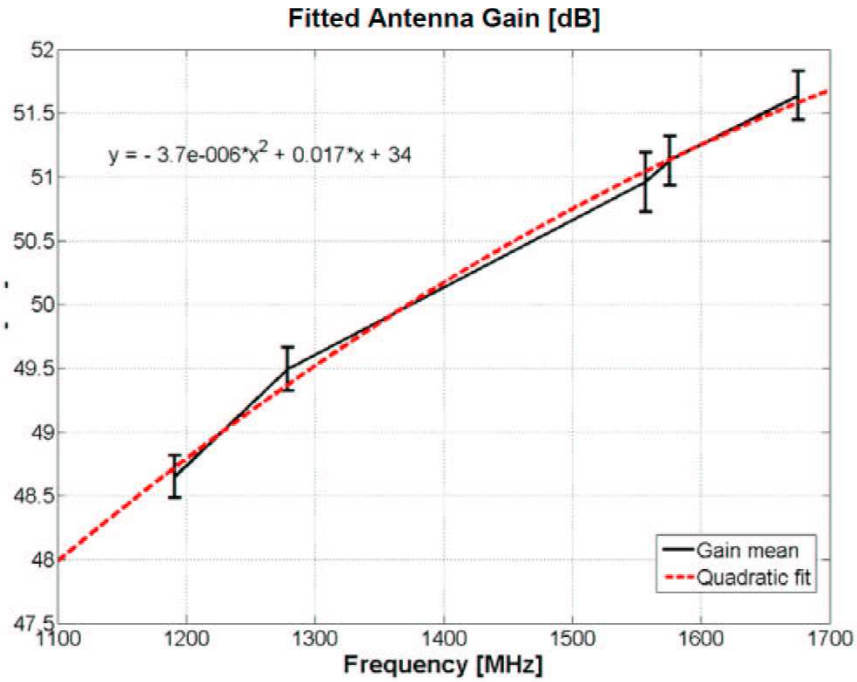

Figure 5.3: Calculated means antenna gain (Source [25])

5.3 Spectral Analysis

5.3.1 Spectral Calibration

The measurement data consists of many parameters such as measurement frequency, peak voltage, resolution bandwidth, maximum frequency, minimum frequency, center frequency, etc. First of all, the power spectral density is calculated with

$$Y_{PSD} = \frac{U_{RMS}^2}{R} \frac{1}{\text{ResolutionBandwidth}} \quad \text{[Watts/Hz]} \tag{5.1}$$

whereas $U_{RMS} = U_{peak}/\sqrt{2}$ is the root mean square voltage, R is the system impedance which equal to 50 Ω in this system.

The equation (3.26) can be transformed to get the effective area of the antenna

$$A_E = \frac{c^2}{4\pi f^2} G \qquad [\text{m}^2] \tag{5.2}$$

whereas G is the antenna gain, f is the frequency, c is the velocity of light.

The spectral flux density at the front of the antenna is calculated with

$$Y_{PSD_{front}} = \frac{Y_{PSD}}{A_E G_r} \qquad [\text{Watts/Hz/m}^2] \tag{5.3}$$

whereas G_r is the system gain.

5.3.2 Comparison with Theoretical Spectrums

The theoretical spectra are generated depending on the frequency band, satellite's generation. Each component in the band is generated according to the PSD equation, for example the P(Y) code is generated from equation (2.22). Only the positive frequency component which is the band center frequency is shown. The C/A theoretical spectrum is generated in the same way but with chip rate of 1.023 MHz, the equation (2.23) is not used because only the spectrum envelope is examined. For military code (M) and Intermodulation product (IM) (see Section 6.3) the spectra of BOC(10,5) and BOC(10,10) are generated using equation (4.8) with the shift to the center frequency.

Now we have all theoretical signal components, but the scaling S of each component to fit for the measured spectral flux density is not found. So 4 points from the smoothed data are chosen to form the linear equation with 4 variables. The chosen points are the point at center frequency: b, the point at which M code is maximum: d, 1/4 distance between the first and the second point: r, and 1/2 distance between the first and the second point: s. The points at b and d are chosen because they are at the center frequency of C/A and M code respectively, while the point r makes the theoretical spectrum matching two side lobes near the center frequency of the measurement, and the point s is the point in the middle of the first two points.

$$S = \begin{pmatrix} \text{fit}Y \\ \text{fit}C/A \\ \text{fit}M \\ \text{fit}IM \end{pmatrix} \tag{5.4}$$

$$H = \begin{pmatrix} PY(b) & C/A(b) & M(b) & IM(b) \\ PY(d) & C/A(d) & M(d) & IM(d) \\ PY(r) & C/A(r) & M(r) & IM(r) \\ PY(s) & C/A(s) & M(s) & IM(s) \end{pmatrix} \tag{5.5}$$

$$M = \begin{pmatrix} \text{smooth}Y(b) \\ \text{smooth}Y(d) \\ \text{smooth}Y(r) \\ \text{smooth}Y(s) \end{pmatrix} \tag{5.6}$$

$$S = H^{-1}M \tag{5.7}$$

After the scaling S is solved, the measured PSD vs. the theoretical spectrum is plotted, as well as the smoothed data compared with the theoretical spectrum. It must be noted that for the old generation of signal there exists 2 components for the L1 band or 1 component for the L2 band, therefore the order of the equation is reduced.

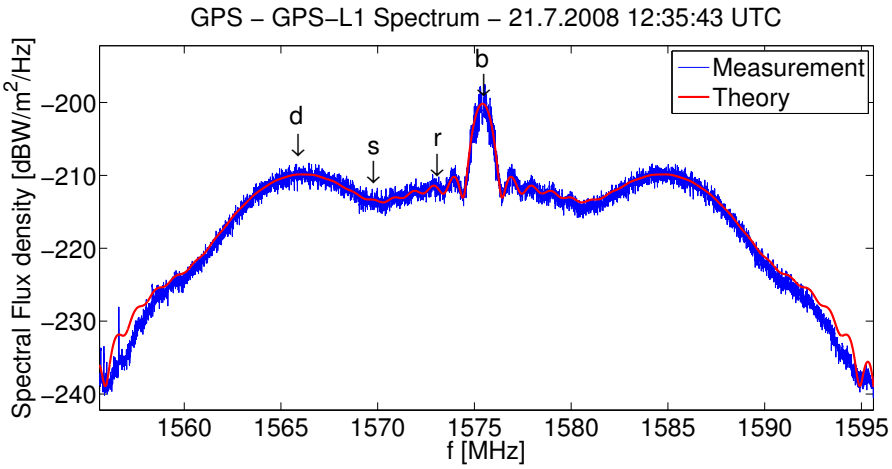

Figure 5.4: The measurement data compared with theoretical spectrum

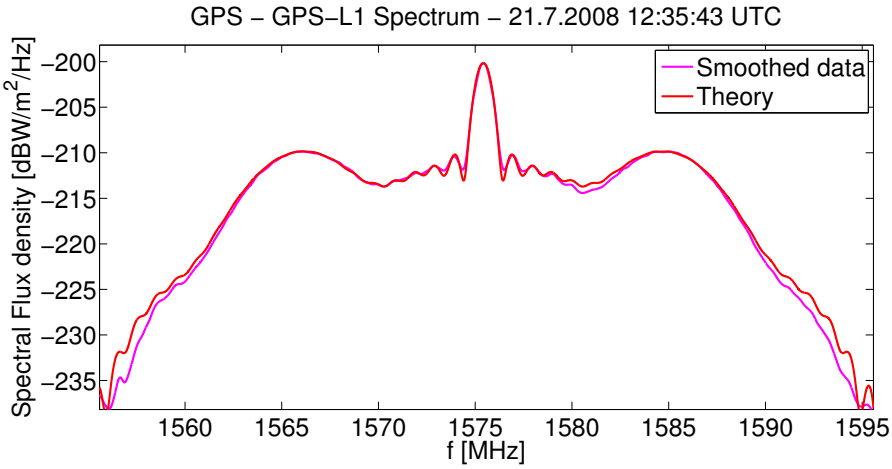

Figure 5.5: The smoothed measurement data compared with theoretical spectrum

The standard deviation of the smoothed measured data is

$$SD = \sqrt{(Y_{PSD_{smooth}} - \mathcal{E})^2} \tag{5.8}$$

whereas the $\mathcal{E}$ is the expected value, which denoted here as the theoretical spectrum. This is to show at which frequency the calculated scaling offset works suboptimal. An example of the standard deviation of the smoothed measured data can be seen in figure 5.6.

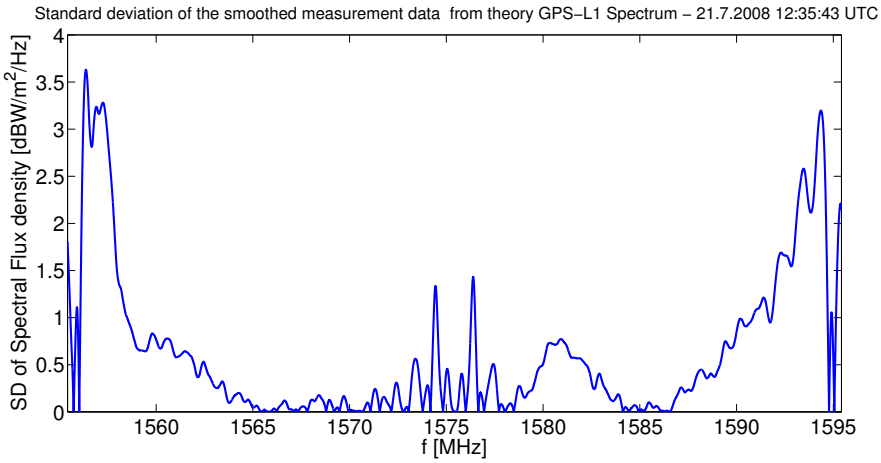

Figure 5.6: The standard deviation of the smoothed measurement from the theoretical spectrum

5.3.3 Spectral Asymmetry

The spectral flux different of the right and the left side with 0.1 MHz bandwidth at different frequency position are calculated and plotted with the lower bound frequency. The figure 5.7 shows the analytical scheme. From this analysis the different of the power at each frequency from center

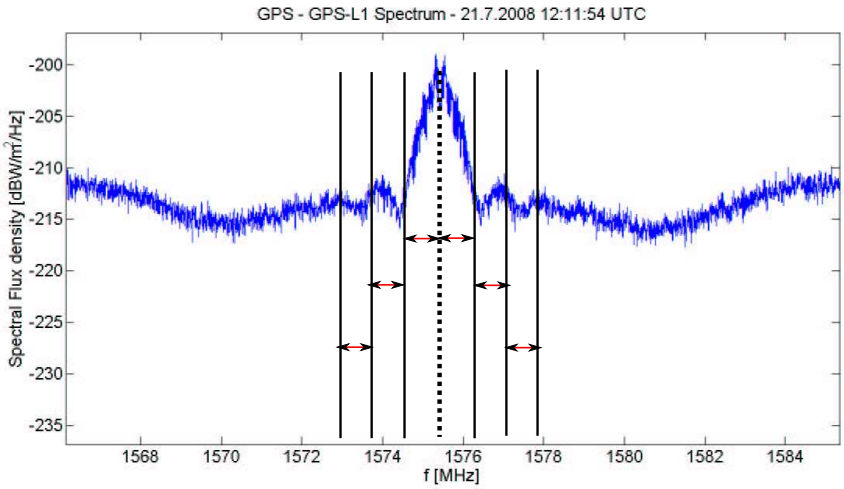

Figure 5.7: Asymmetry analysis scheme

frequency can be determined.

5.3.4 Measurement Dependency on the Elevation

The equivalent isotropic radiated power (EIRP) is plotted over the satellite elevations. The EIRP is calculated as a spectral flux of the used GPS bandwidth compensated with the path loss.

$$EIRP = Y_{PSD_{front}} + L_{pathLoss} \qquad \text{[dBW]} \tag{5.9}$$

The elevation and range of the satellites are obtained from the TLE data, which is the two line elements format giving the satellites path.

The antenna pattern is plotted as a function of EIRP over the Nadir angle ϕ, which is the angle between the direction pointing directly below a satellite and the direction pointing to the receiver position.

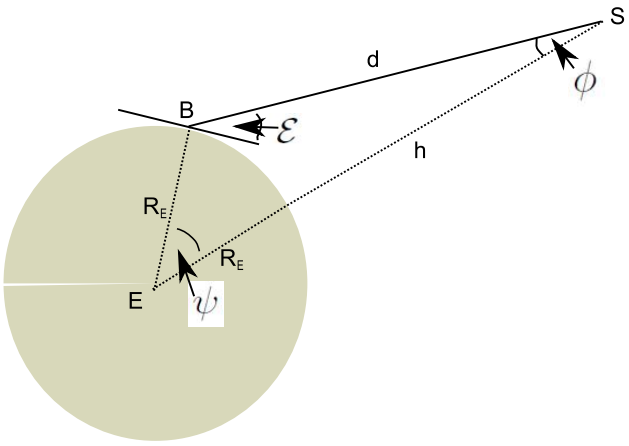

Figure 5.8: Satellite geometry

In figure 5.8 E is the earth center, S is the satellite position, R_E is the earth radius, d is the slant range, ϵ is the elevation, ψ is the angle of the earth center, and h is the orbit altitude.

The Nadir angle can be calculated from the Law of Sines as

$$\phi = \arcsin\left(\frac{R_E}{R_E + h}\cos(\epsilon)\right) \tag{5.10}$$

The asymmetry of the signal, the spectral flux density and the power of 1 MHz bandwidth at the M code peak can also be plotted over the elevation.

5.4 IQ Data Analysis

5.4.1 IQ Data Processing

The parameter needed from the saved .mat file for this analysis are the sampling time denoted as XDelta and the signal voltage saved in complex number, whereas the real part of the signal voltage means in-phase component and imaginary part of the signal voltage means quadrature component. The signal is already down-converted to baseband, however this signal still cannot be plotted, because there is a frequency offset called Doppler frequency caused by satellite's movement. The phase rotation in the IQ plot due to Doppler frequency can be seen in figure 5.9.

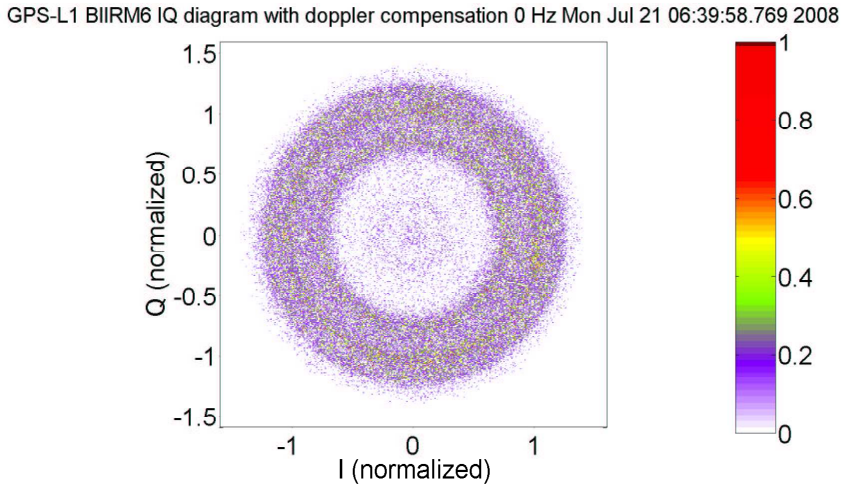

Figure 5.9: IQ constellation plot of raw data without Doppler compensation

The received signal after down conversion to baseband is modeled as

$$\begin{aligned} s(t) = A(t)\cos(\theta(t) + \phi(t) + \psi(t)) \\ + A(t)\sin(\theta(t) + \phi(t) + \psi(t)) \end{aligned} \tag{5.11}$$

whereas $A(t)$ is a magnitude of the signal affected by AWGN, $\theta(t)$ is the ideal phase of the transmitted symbol, $\phi(t)$ is the component affected by the frequency offset, and $\psi(t)$ is the phase error due to AWGN. The frequency offset component is assume to have a linear characteristic defined by

$$\phi(t) = at + b \tag{5.12}$$

where a is the parameter which defines the phase rotation due to Doppler frequency and b is the initial phase offset.

To find the Doppler frequency, the acquisition method based on FFT search algorithm using circular correlation as explained in section 3.2 is implemented. As commonly known the C/A code is used for the coarse acquisition because of the short integration time and faster processing. The C/A PRN signal is pre-generated for each satellite using LSFR and saved to be instantly used. The sampling frequency f_s is needed to find the number of samples to be processed within 1 ms, whereas 1 ms corresponds to a period of C/A PRN code. The sampling time is needed to generate the processed time vector. The PRN pre-generated code is up sampled to the same number of to be processed data. Thereafter an FFT search algorithm using the zero padding technique[1] described in [21] is done, whereas 1 ms data correlated with replica of the first half of the PRN code padded another half with zeros, and the correlation of 1 ms data with the first half padded with zeros and another half with second half of the PRN code are search within the Doppler frequency range. The code phase and Doppler frequency of the maximum correlation is the value desired for later processing.

The achieved Doppler frequency is still not fine enough to generate the IQ plot. Hence the fine frequency estimation method described in [18] is performed. The approach to find the fine frequency resolution is through phase relation of the correlation of the carrier wipe off signal and

[1]The zeros padding method is first introduced to be used with acquisition of GALILEO satellite signal where the secondary code exists, but it is also usable for other type of code without secondary code.

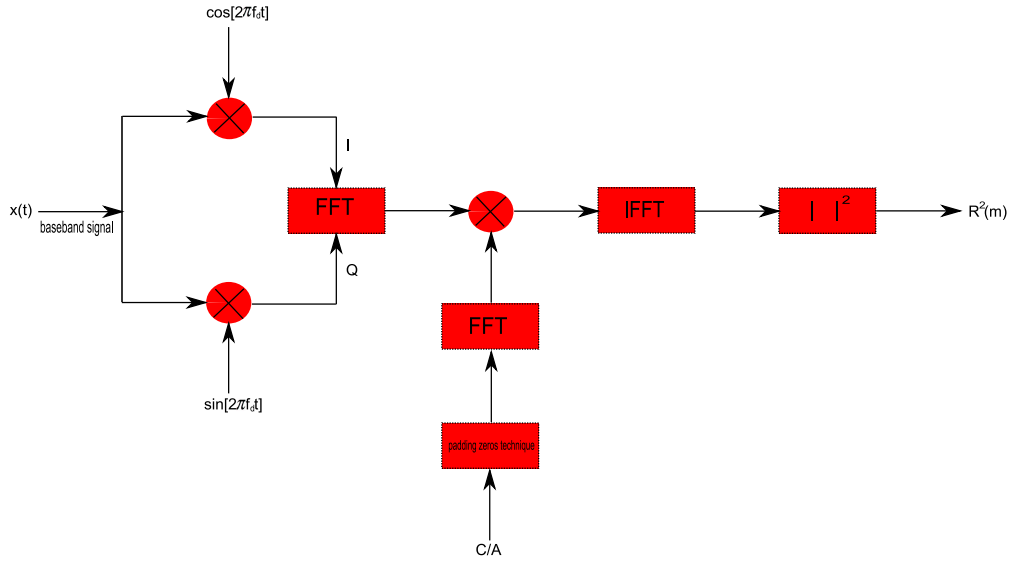

Figure 5.10: FFT correlation with zeros padding technique

code in 1 ms of data at time m and consecutively thereafter at n.

$$\theta_m(k) = \tan^{-1}\left(\frac{Im(X_m(k))}{Re(X_m(k))}\right) \tag{5.13}$$

$$\theta_n(k) = \tan^{-1}\left(\frac{Im(X_n(k))}{Re(X_n(k))}\right) \tag{5.14}$$

These two phase angles can be used to find the fine frequency as

$$f = \frac{\theta_n(k) - \theta_m(k)}{2\pi(n-m)} \tag{5.15}$$

whereas the threshold to bound the accuracy of the frequency, the 2π phase transition due to $\arctan$ ambiguity, and π phase transition due to navigation data must be taken into account. After doing this the fine frequency is estimated for all of the intervals and then corrects the coarse frequency. The term $2\pi f$ is equivalent to a from equation (5.12) and can correct the phase rotation of the signal.

Still there is the initial phase offset to be searched. Here the statistical method is required, where angle of the point in the constellation with maximum probability to the real axis is calculated and the complete constellation is rotated with this angle. Thereafter the points are compared with the ideal points defined by Interface Specification and rotated to the most probable constellation. The signal is now expressed as

$$\begin{aligned} s(t) = {} & A(t)\cos(\theta(t) + \psi(t)) \\ & + A(t)\sin(\theta(t) + \psi(t)) \end{aligned} \tag{5.16}$$

where the error due to AWGN still exist. Finally the IQ constellation can be plotted and the further processing of the IQ data can be done from this point.

5.4.2 Error Vector Magnitude

Error Vector Magnitude is a measure used to quantify the performance of a digital radio transmitter or receiver in a communication system using digital modulation. The imperfection in the implementation such as noise, phase noise, carrier suppression, and distortion makes the constellation points deviated from the ideal constellation. Error vector represents the difference between the measured signal and a reference. EVM is the magnitude of error vector. Magnitude Error and Phase Error are the magnitude and phase difference of signal and reference [22].

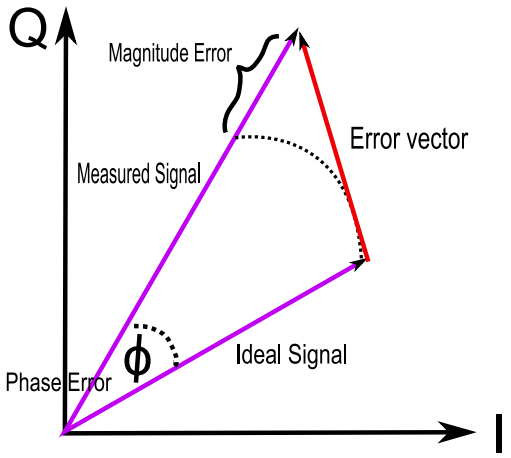

Figure 5.11: Error Vector Magnitude and related quantities (Source:[22])

$$MagnitudeError = \sqrt{I^2 + Q^2} - \sqrt{I_{ideal}^2 + Q_{ideal}^2} \tag{5.17}$$

$$PhaseError = \arctan\frac{Q}{I} - \arctan\frac{Q_{ideal}}{I_{ideal}} \tag{5.18}$$

$$EVM = \sqrt{(I - I_{ideal})^2 + (Q - Q_{ideal})^2} \tag{5.19}$$

$$EVM_{RMS} = \sqrt{\frac{\sum_{j=1}^{N}[(I - I_{ideal})^2 + (Q - Q_{ideal})]^2}{\sum_{j=1}^{N}(I_{ideal}^2 + Q_{ideal}^2)}} \tag{5.20}$$

The Error Vector Magnitude is a function used to decide the phase to be rotated to an ideal constellation.

The Modulation Error Ratio (MER) is a measure of the signal to noise ratio in a digital modulation defined as [38]

$$MER = \frac{\sum_{j=1}^{N}[(I_{ideal})^2 + (Q_{ideal})]^2}{\sum_{j=1}^{N}[(I - I_{ideal})^2 + (Q - Q_{ideal})^2]} \tag{5.21}$$

MER is closely related to signal-to-noise ratio. It includes all imperfections including deterministic amplitude imbalance, quadrature error and distortion, while noise is random by nature.

5.4.3 Correlation Peak Determination

The correlation of the IQ data with the reference code signal is processed and normalized with the square root of IQ power multiplied by C/A reference code power as define in [23]

$$R(\tau) = \frac{\int_0^{T_p} s_{IQ}(t) s_{Ref}(t+\tau) dt}{\sqrt{(\int_0^{T_p} |s_{IQ}|^2 dt)(\int_0^{T_p} |s_{Ref}|^2 dt)}} \tag{5.22}$$

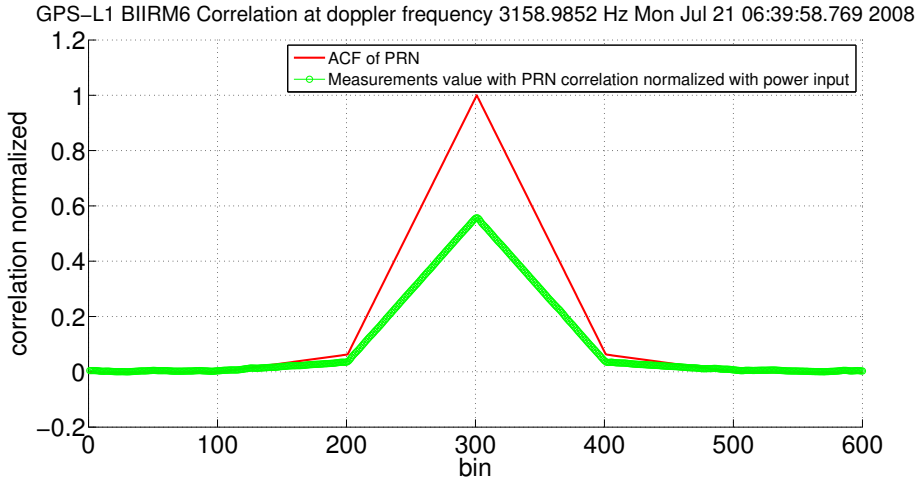

Figure 5.12: Correlation of signal with PRN normalized as in the equation compared with ACF of PRN

As seen in figure 5.12 the power of the correlation is not equal to 1 because the IQ data contains the imaginary part, in which the C/A code does not exist.

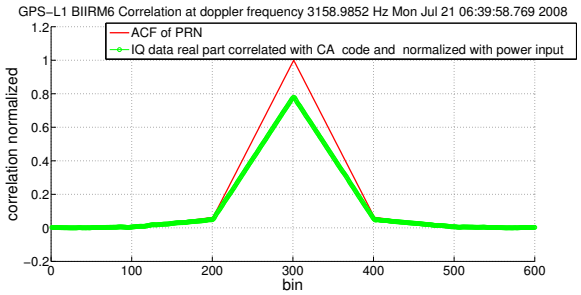

Figure 5.13: IQ data real part correlated with C/A code and normalized with the square root of real part IQ power multiplied by C/A power

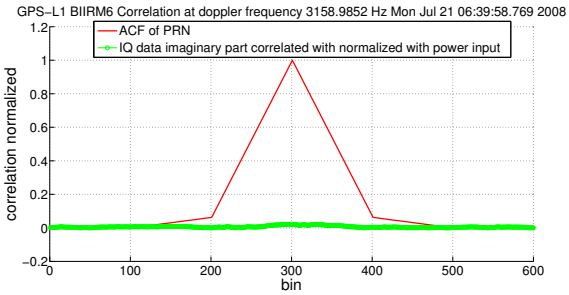

Figure 5.14: IQ data imaginary part correlated with C/A code and normalized with the square root of imaginary IQ power multiplied by C/A power

In figure 5.13 the normalized correlation is about 0.8, which is more than in the figure 5.12, but it is still not equal to 1 due to the phase distortion of the in-phase and quadrature component. In imaginary part of 5.14 it shows no correlation.

Later every correlation function is normalized with the square root of complex IQ power multiplied by C/A reference code power.

The correlation plots of the real and imaginary data are used to check if the rotated constellations are in the right position. Since the phase of C/A signal carrier lag the P signal by 90 degree as mentioned in [24], either the real or imaginary part must be correlated with the C/A code as shown in figure 5.15.

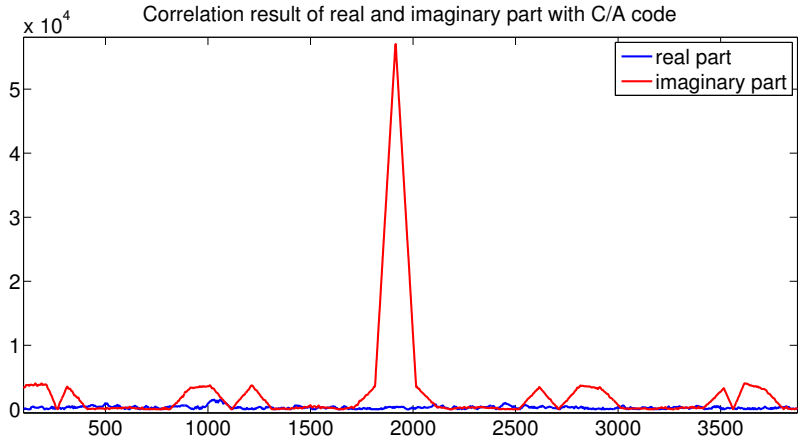

Figure 5.15: Correlation result of real and imaginary part with C/A code

The imbalance of the correlation peak is also plotted, in which each bin of the left and right side of maximum correlation point are subtracted. The left bin can be interpreted as early chip and the right bin can be interpret as late chip in the discriminator function.

$$\frac{dR(\tau)}{d\tau} = \frac{R(\tau + \frac{d}{2}T_c) - R(\tau - \frac{d}{2}T_c)}{dT_c} \tag{5.23}$$

Here we vary d, fix τ at the optimal position, and neglect the denominator. This is compared with the ideal PRN peak where the value is always balanced and results to zero error value. The interval of interest is normally between the non-zero correlation peaks that is about 100 bins.

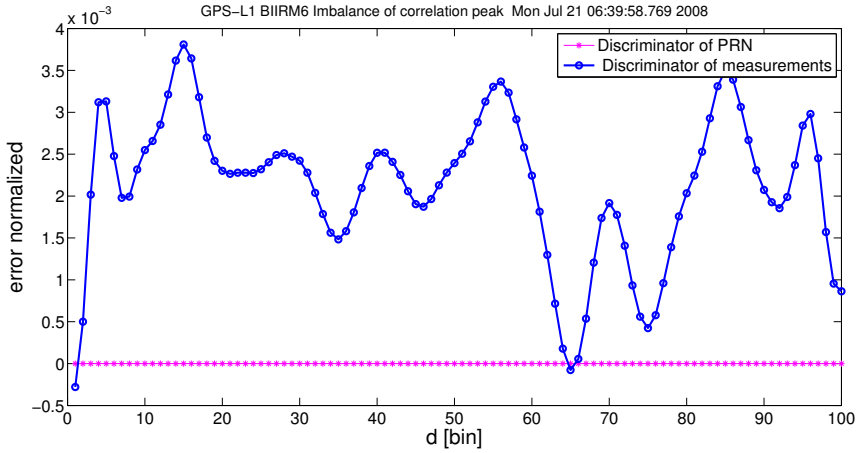

Figure 5.16: The imbalance of the correlation peak: left minus right from maximum point

Two different S-Curves and their lock point bias are generated. The early minus late power mode S-Curve is a function of

$$\mathrm{SCurve}(\tau, d) = R_I(\tau - \frac{d}{2})^2 + R_Q(\tau - \frac{d}{2})^2 - R_I(\tau + \frac{d}{2})^2 - R_Q(\tau + \frac{d}{2})^2 \tag{5.24}$$

The dot product mode S-Curve is a function of

$$\mathrm{SCurve}(\tau, d) = (R_I(\tau - \frac{d}{2}) - R_I(\tau + \frac{d}{2})R_I(\tau) + (R_Q(\tau - \frac{d}{2}) - R_Q(\tau + \frac{d}{2})R_Q(\tau) \tag{5.25}$$

The lock point bias $\tau_{bias}(d)$ is the time , in which the discriminator crosses zero. It indicates the accuracy of the discriminator function.

$$\mathrm{SCurve}(\tau_{bias}(d), d) = 0 \tag{5.26}$$

From the lock point bias, the error of the Tracking process can be estimated.

$$S(d) = c\tau_{bias}(d) \qquad \text{[meter]} \tag{5.27}$$

whereas S is the distance error and c is the velocity of light.

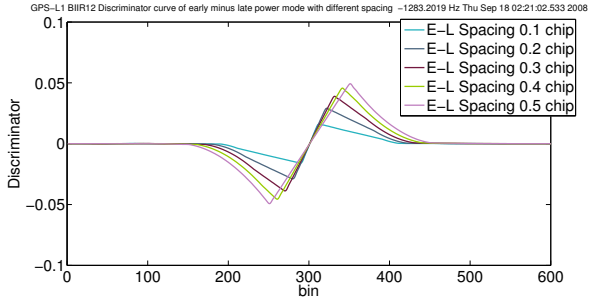

Figure 5.17: S-Curve of early minus late power discriminator

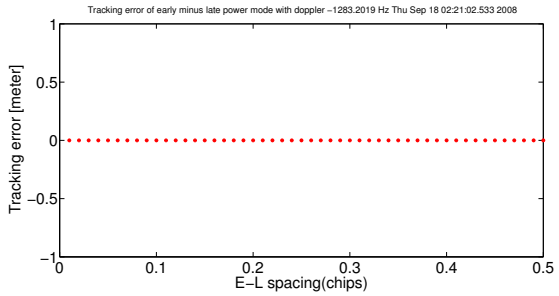

Figure 5.18: Tracking error of early minus late power discriminator

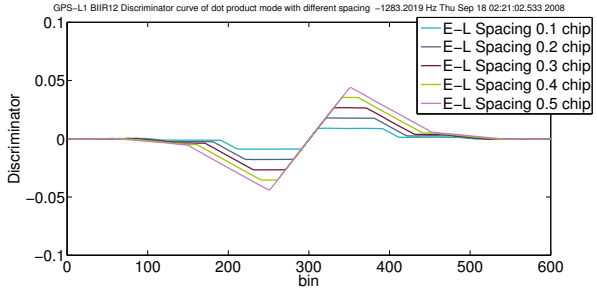

Figure 5.19: S-Curve of early dot product discriminator

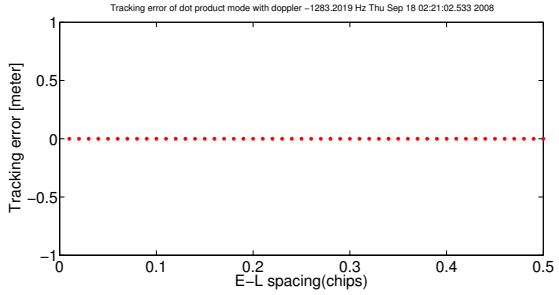

Figure 5.20: Tracking error of dot product discriminator

5.4.4 IQ Data Filtering

Some types of filter are designed such as Chebychev filter, Cauer filter und FIR filter using MATLAB function. The IQ data are filtered by the designed filters. Thereafter the spectrums, the IQ constellations and the correlation characteristics can be determined.

5.4.5 IQ Data with Pwelch

After the IQ data is rotated to the possible constellation, the power spectral density can be generated using 'pwelch' function in MATLAB. The complex PSD, real part PSD, and imaginary part PSD can be generated and analyzed comparing with theoretical PSD in the same way as described in 5.3.2.

6. Result and Analysis

6.1 GPS BIIR12 L1

The IQ constellation of GPS satellites of block BIIA and BIIR in L1 band can be generated directly because the Interface Specification [24] states that the nominal composite L1 signal phase are at 0°, -70.5°, +109.5° and 180° to each other due to a 3 dB power difference. From this point the error vector magnitude can also be calculated, because the ideal constellation is known.

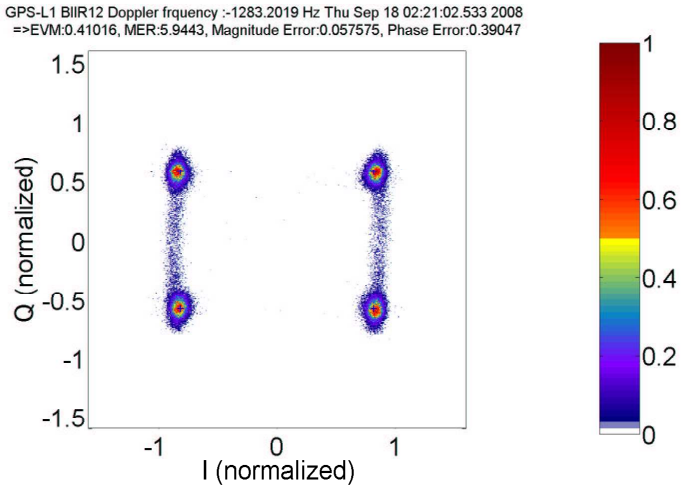

Figure 6.1: IQ Constellation of GPS BIIR12 L1 signal

It can be seen from figure 6.1 that the transitions in the quadrature phase occur more often than in the in-phase, therefore in the quadrature channel must be coded with a faster code, which is P(Y). The symbols + in this figure show the ideal constellation points.

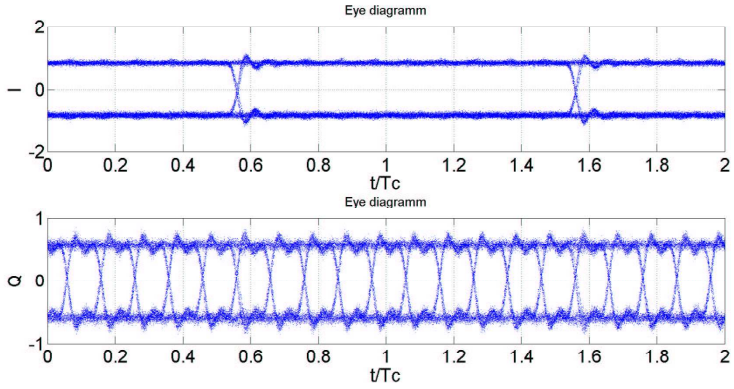

Figure 6.2: Eye diagram of GPS BIIR12 L1 signal

From figure 6.2 two periods of C/A code are shown. It can be seen that the C/A code, of which the code rate is 1.023 MHz and has code period ten times the P(Y) code, are modulated to the

in-phase channel. Whereas the P(Y) with code rate of 10.23 MHz is modulated to the quadrature channel. At the beginning of each code phase the overshoots can be seen due to bandwidth limitation but on contrary to the Gibbs Phenomenon they are nearly absent at the end of the pulse.

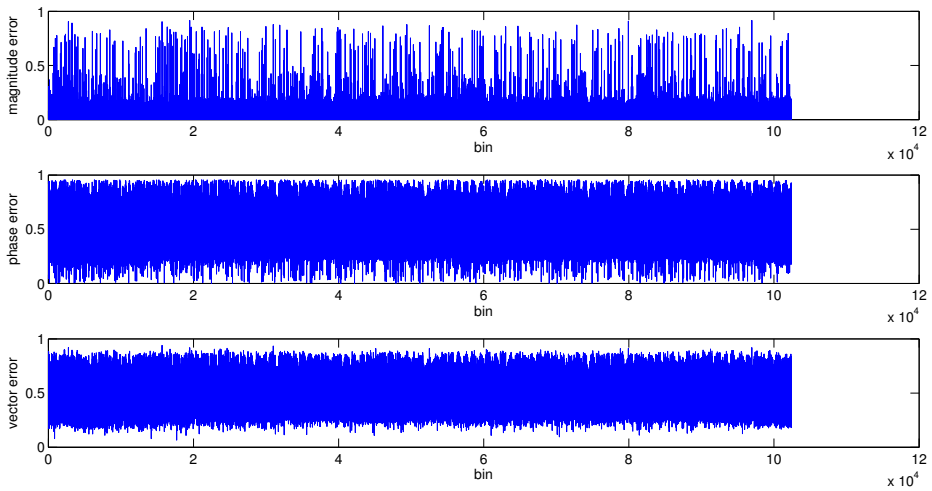

Figure 6.3: Error vector magnitude and related quantities of GPS BIIR12 L1 signal for 1 C/A code period

In figure 6.3 the values variate for the entire interval. The magnitude error varies mostly to about 0.25 in contrast the the phase error and the vector error, which vary to 0.5 or more. The root mean squares of these values given in the figure 6.1 are equal to 0.4106 for EVM, 5.9443 for MER, 0.057575 for magnitude error and 0.39047 for phase error. These values give a general survey of the signal.

The Error vector magnitude and related quantities of the measured GPS L1 signal of different satellites are not much different from each other as seen in figure 6.4 and 6.5. This could be due to the purity of the signal and the perfection of the rotated IQ constellation. The EVM and related quantities are used later to determine to quality of the signal after distortion such as after filtering.

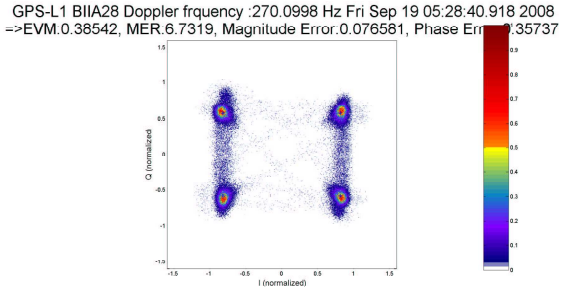

Figure 6.4: IQ diagram and EVM of the L1 GPS BIIA28

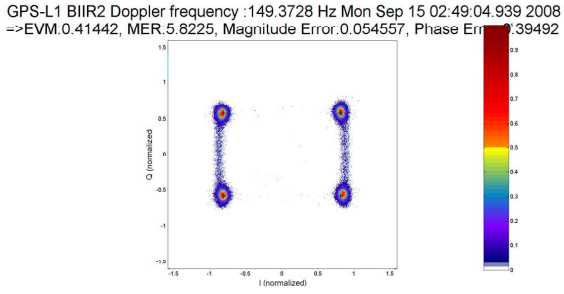

Figure 6.5: IQ diagram and EVM of the L1 GPS BIIR2

In figure 6.6 and 6.7 the measurement and theoretical signal are compared, the interested bandwidth is 1565.19 MHz-1585.65 MHz which is the bandwidth of GPS L1 [24]. The measurement signal lies quite well on the theoretical signal. On the right band side the measurement lies a little bit under the theory. The standard deviation of the smoothed signal and theoretical signal is very low and well distributed over the bandwidth.

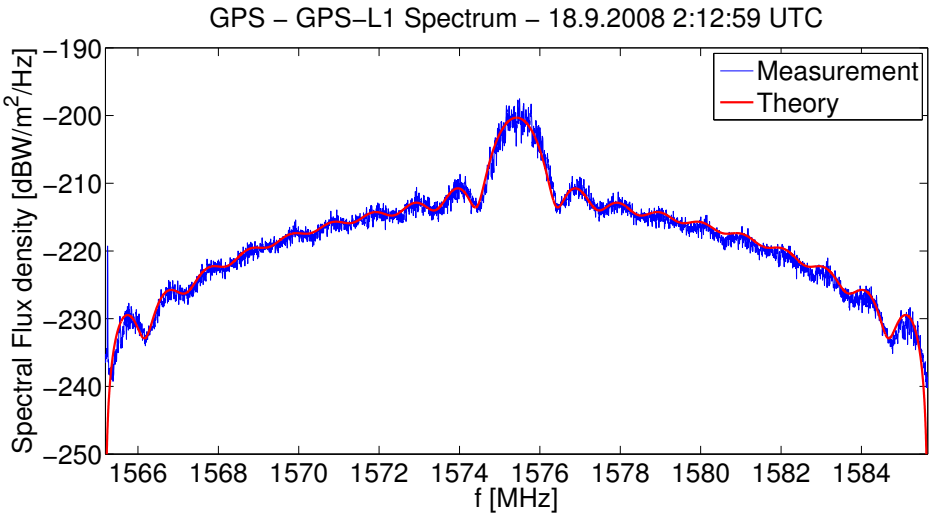

Figure 6.6: Measurement signal compared with theory of GPS BIIR12 L1 signal

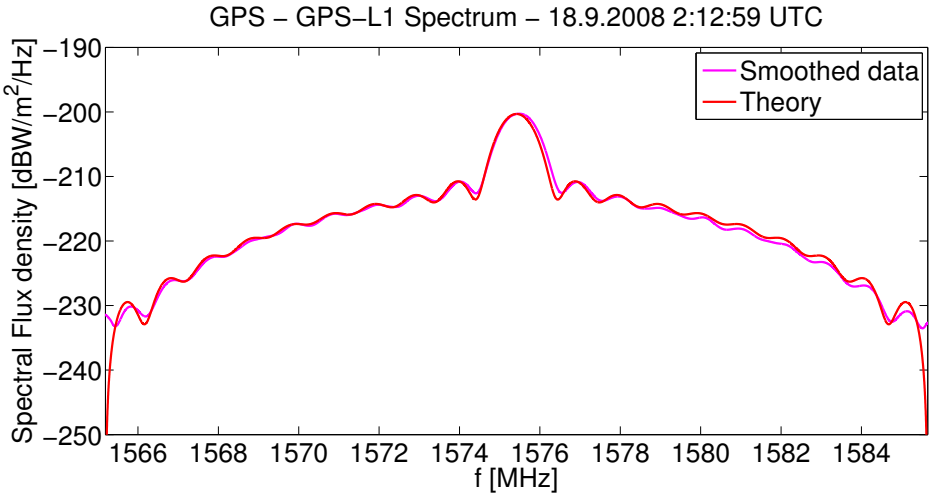

Figure 6.7: Smoothed measurement signal compared with theory of GPS BIIR12 L1 signal

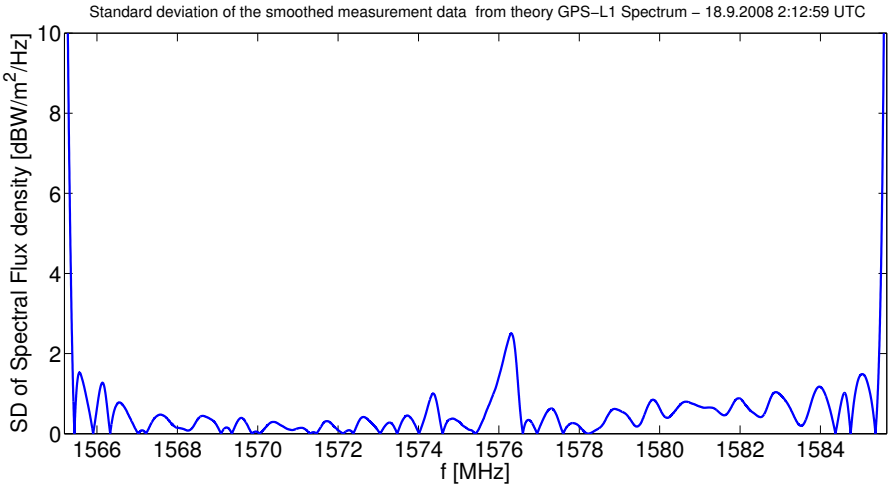

Figure 6.8: SD of the smoothed measurement signal and theory of GPS BIIR12 L1 signal

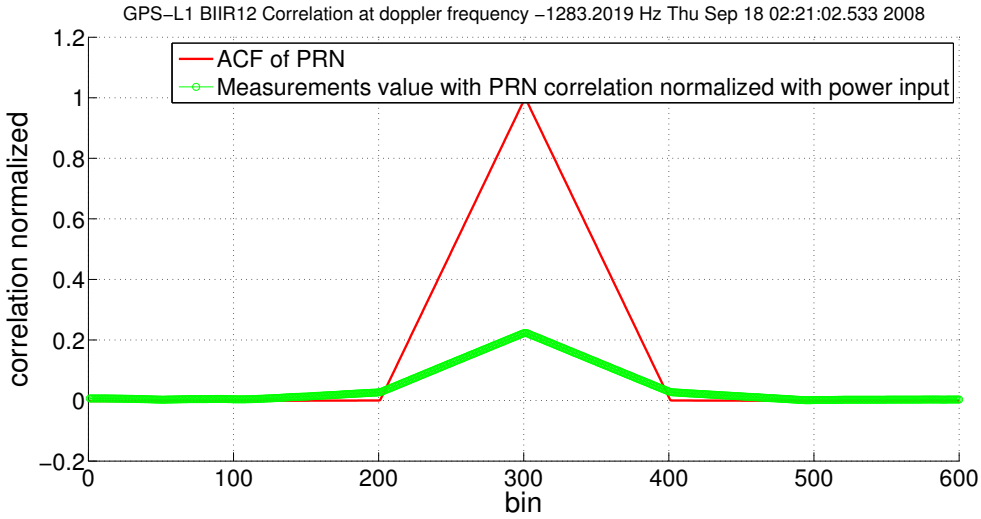

Figure 6.9: Correlation normalized with input power of GPS BIIR12 L1

From figure 6.9 the correlation peak of the signal compared with the correlation of generated C/A code is shown. The normalized correlation peak of about 0.23 indicates that there is quite a lot of power not correlated to C/A code in this measurement.

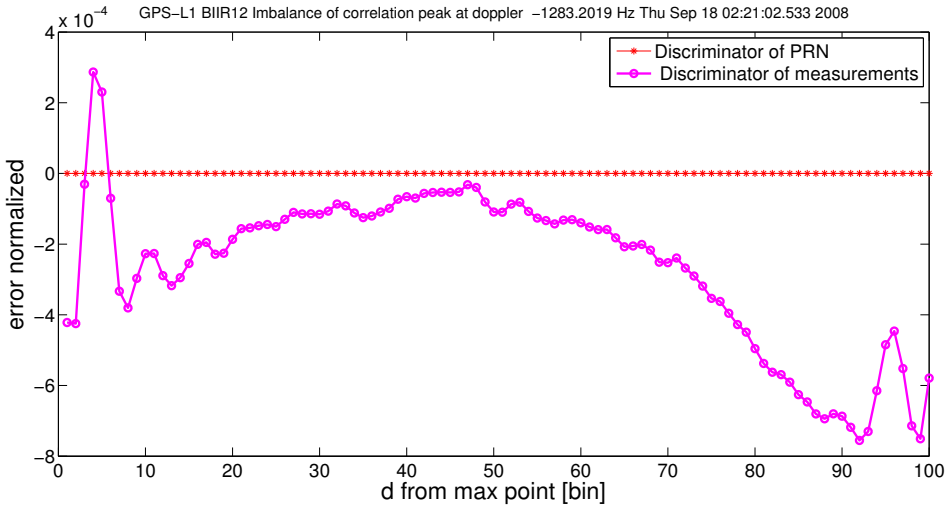

Figure 6.10: The imbalance of the correlation peak of GPS BIIR12 L1

The imbalance show that the late bin has more power than the early bin for mostly of the interval on contrary to the ideal discriminator, where the early and late power bin are equal.

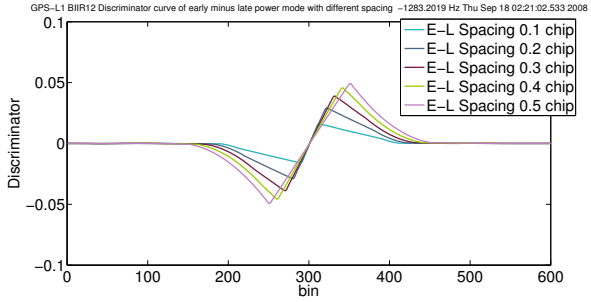

Figure 6.11: S-Curve of early minus late power discriminator

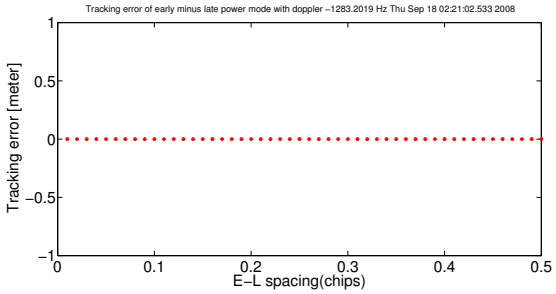

Figure 6.12: Tracking error of early minus late power discriminator

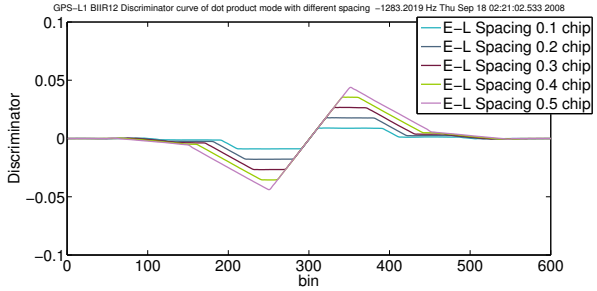

Figure 6.13: S-Curve of early dot product discriminator

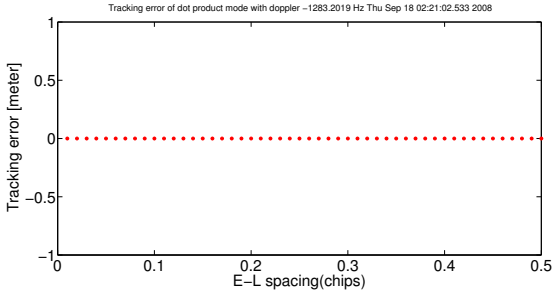

Figure 6.14: Tracking error of dot product discriminator

From figure 6.11- 6.14 the discriminator functions are shown, the tracking error of the discriminators are all exactly at zero, which means there is no error in tracking process for the chosen spacings.

6.2 GPS BIIR12 L2

The Doppler compensation of this band is a bit more complex because the PRN code of P(Y) is too long, therefore the Doppler frequency is calculated using the satellite position from TLE data. The IQ constellation of GPS satellites of block BIIA and BIIR in L2 band composed of only P(Y) code which is BPSK. Therefore the ideal constellation points are on 1 and -1. The most transitions are not through zero and look like an eye.

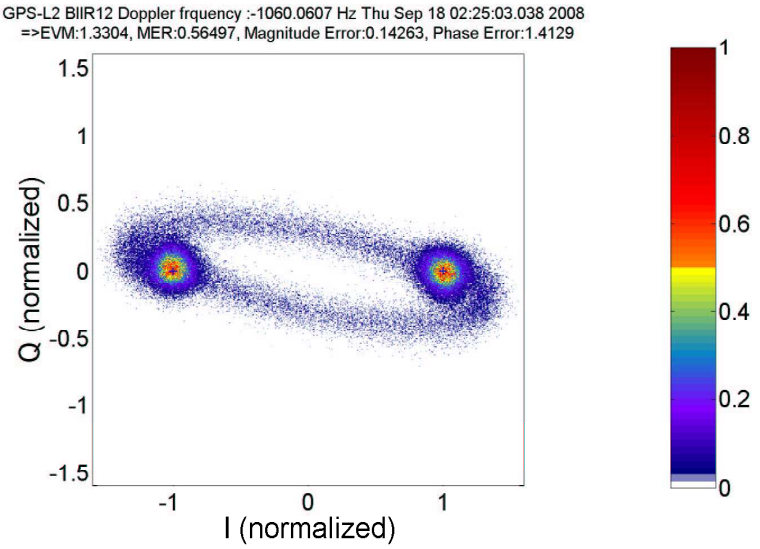

Figure 6.15: IQ Constellation of GPS BIIR12 L2 signal

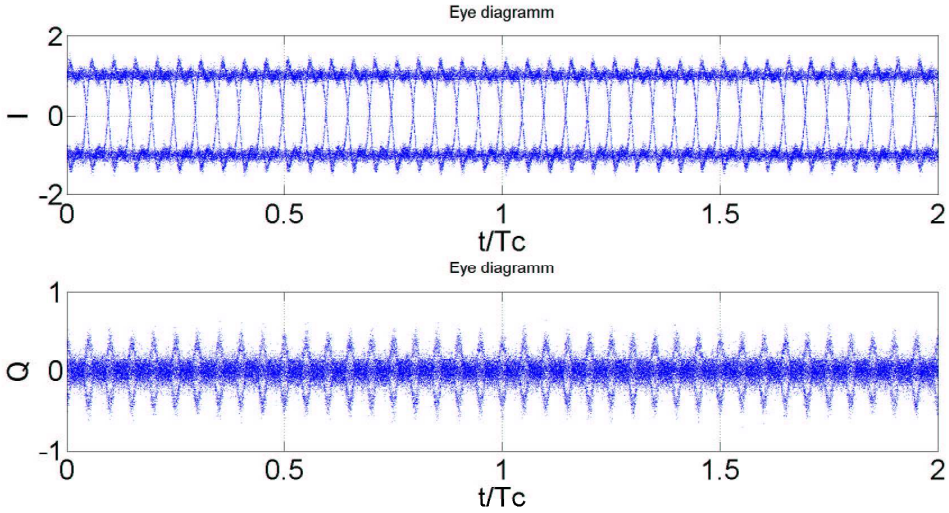

Figure 6.16: Eye diagram of GPS BIIR12 L2 signal

The eye diagram in figure 6.16 is generated with the period of L2CM code, which has code rate 511.5 kHz but still does not exist in this old satellite generation. As seen, the P(Y) code is modulated to the in-phase channel with code rate of 10.23 MHz, which is 20 times faster than L2CM code. In quadrature the teeth are seen due to the transitions which do not go through zero.

In fig 6.17 and 6.18 the measurement and theoretical signal are compared, the interested bandwidth is 1217.37 MHz - 1237.83 MHz which is the bandwidth of GPS L2 [24]. The power spectral

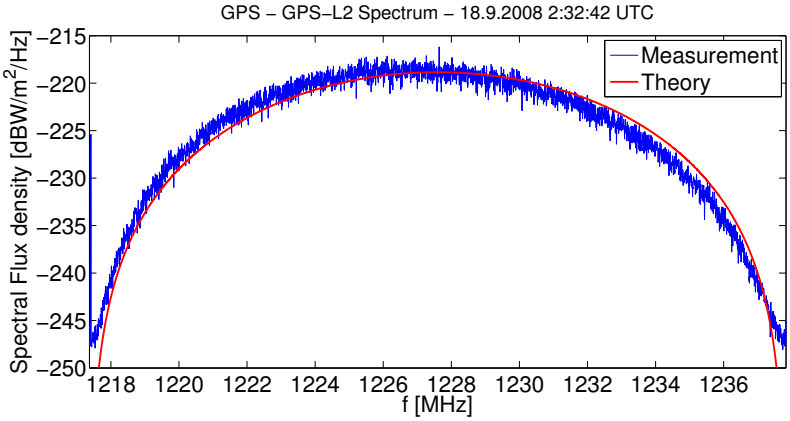

Figure 6.17: Measurement signal compared with theory of GPS BIIR12 L2 signal

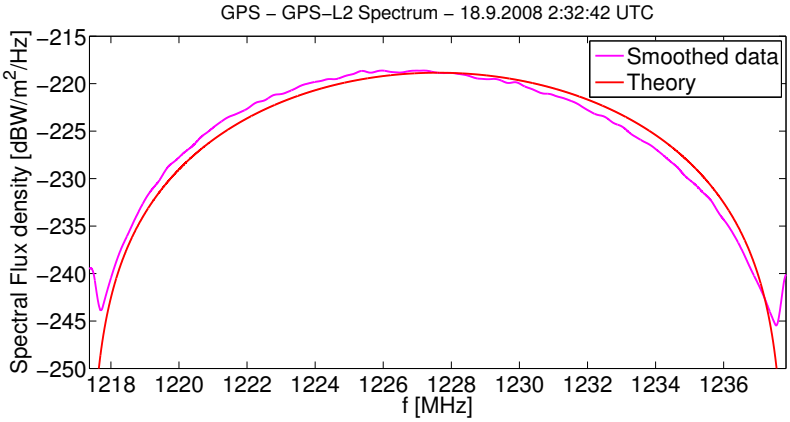

Figure 6.18: Smoothed measurement signal compared with theory of GPS BIIR12 L2 signal

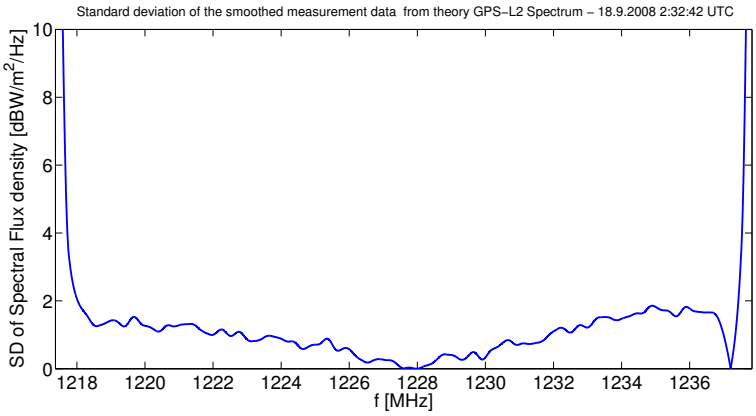

Figure 6.19: SD of the smoothed measurement signal and theory of GPS BIIR12 L2 signal

densities show asymmetries where the left side of the center frequency has more power than the right side. The asymmetry of the signal could be caused by to the dispersive behavior of the front-end, which will be investigated in section 8.2.

The standard deviation of the smoothed signal and theoretical signal shows the point where the offset is calculated which is at the center frequency; there the SD is lowest and increasing to the bound.

6.3 GPS BIIRM6 L1

The L1 signals from satellites of block BIIRM are transmitted with the new added M code, which is a BOC(10,5). As published in [31] and [32] , the Coherent Adaptive Subcarrier Modulation (CASM) proposes to put the P code signal and the M code in the in-phase component and the C/A code in the quadrature component with the Intermodulation (IM) product, whereas the IM product is the product of the three desired signals balanced by the modulation indexes. The IM product is a BOC(10,10) subcarrier.

These signals are considered as Interplex and can be written as

$$\begin{aligned} s(t) = \sqrt{2}(\sqrt{P_I}s_2(t)\cos(m) - \sqrt{P_Q}s_3(t)\sin(m))\cos(2\pi f_c t + \phi) \\ -\sqrt{2}(\sqrt{P_Q}s_1(t)\cos(m) + \sqrt{P_I}s_1(t)s_2(t)s_3(t)\sin(m))\sin(2\pi f_c t + \phi) \end{aligned} \tag{6.1}$$

whereas P_I is the power of the initial signal in in-phase, P_Q is the power of initial signal in quadrature, m is the modulation index, which is not set. $s_1(t)$, $s_2(t)$ and $s_3(t)$ is the C/A, P(Y) and M code, respectively.

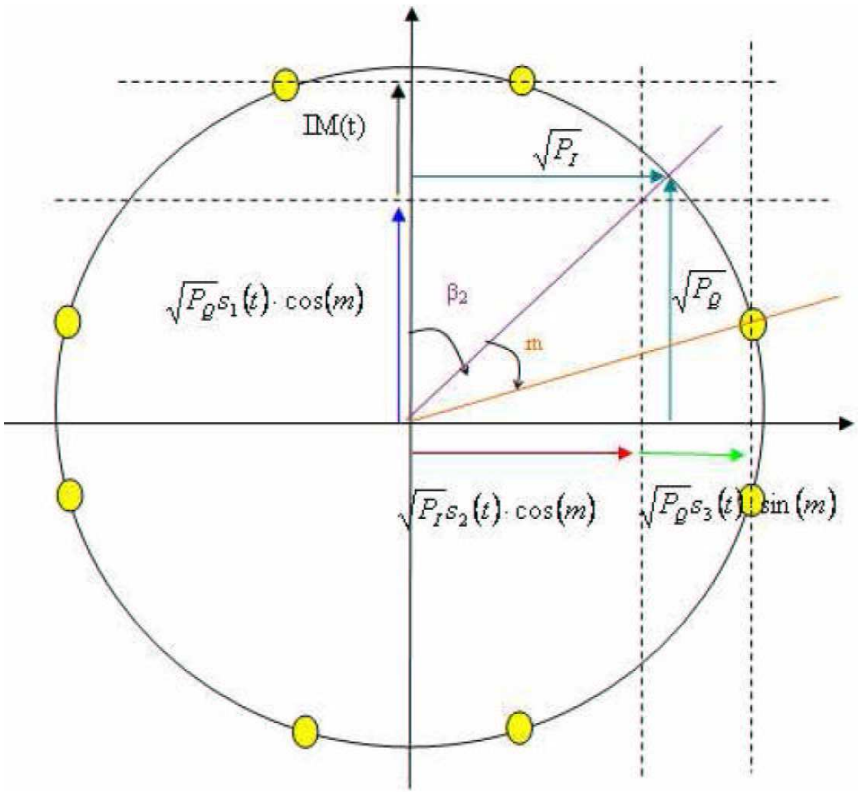

Figure 6.20: GPS Interplex modulation constellation (Source:[31])

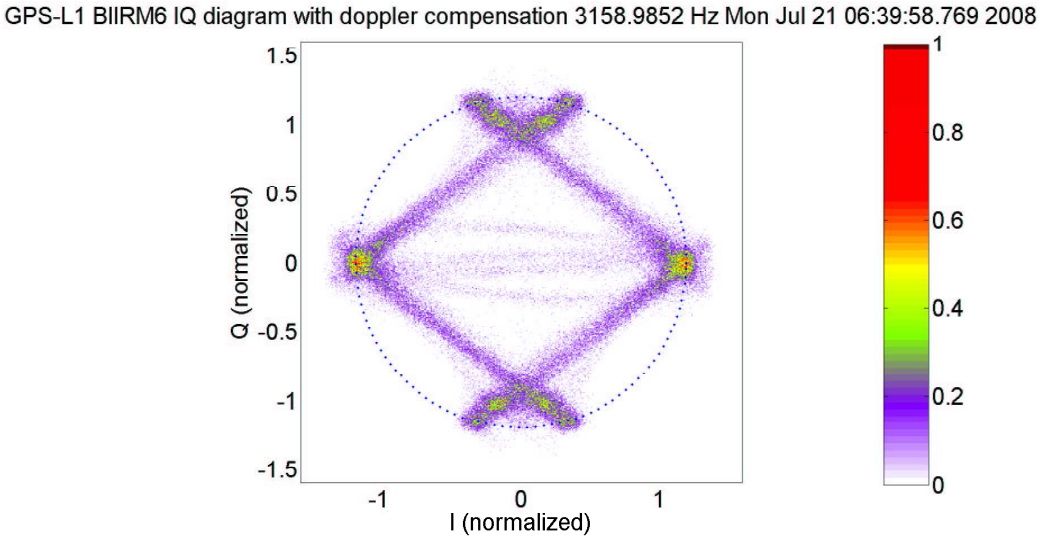

Figure 6.21: IQ Constellation of GPS BIIRM6 L1 signal

It can be seen from figure 6.21 that IQ constellation could be 6 points not 8 likes introduced. The points at (1.2, 0) and (-1.2, 0) in real axis have more probability than other points, maybe because the constellation goes through these points twice.

Next the rotated IQ is correlated with C/A code PRN7. The correlation in in-phase as well as in quadrature component are shown in figure 6.22. The correlation on the quadrature component shows high correlation, which means the C/A code are modulated to the quadrature phase, as proposed in [31].

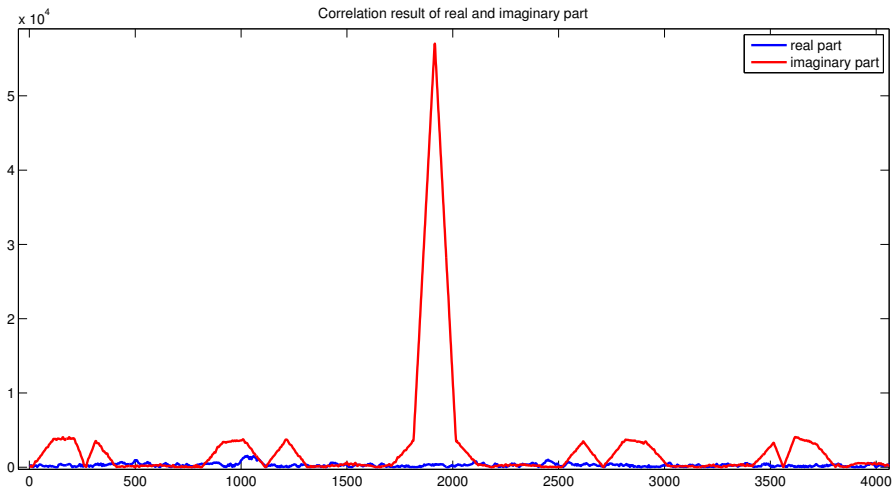

Figure 6.22: Correlation of BIIRM6 to C/A code PRN7

The spectrum density from the rotated IQ are generated using pwelch function in MATLAB and compared with generated theoretical spectrum as seen in figure 6.23- 6.25. The calculated portion of each code component is given in the figure title.

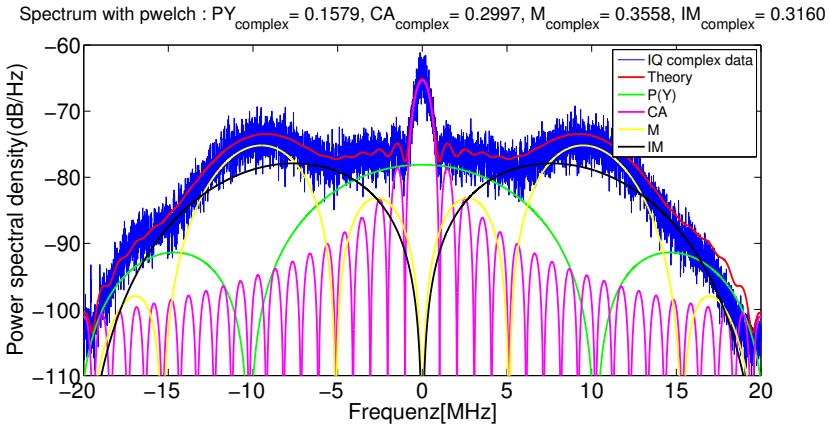

Figure 6.23: BIIRM6 complex PSD with pwelch function

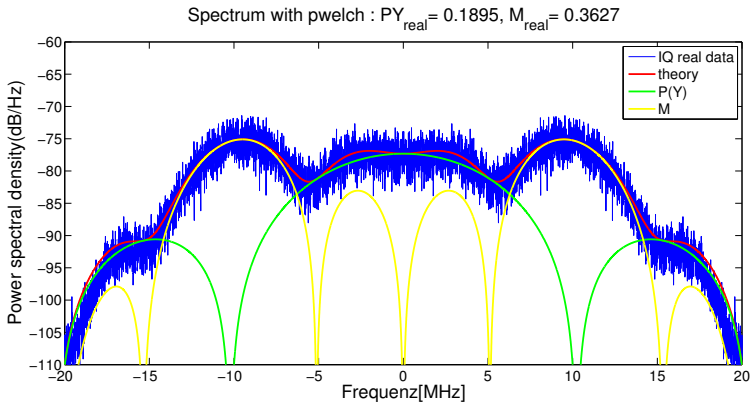

Figure 6.24: BIIRM6 real PSD with pwelch funktion

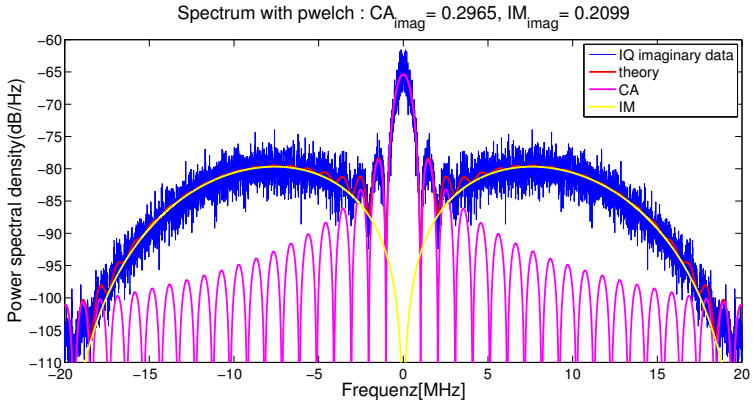

Figure 6.25: BIIRM6 imaginary PSD with pwelch function

From figure 6.24 the in-phase of the rotated IQ data is composed of P(Y) and M code.

From figure 6.25 the quadrature phase of the rotated IQ data is composed of C/A and IM product.

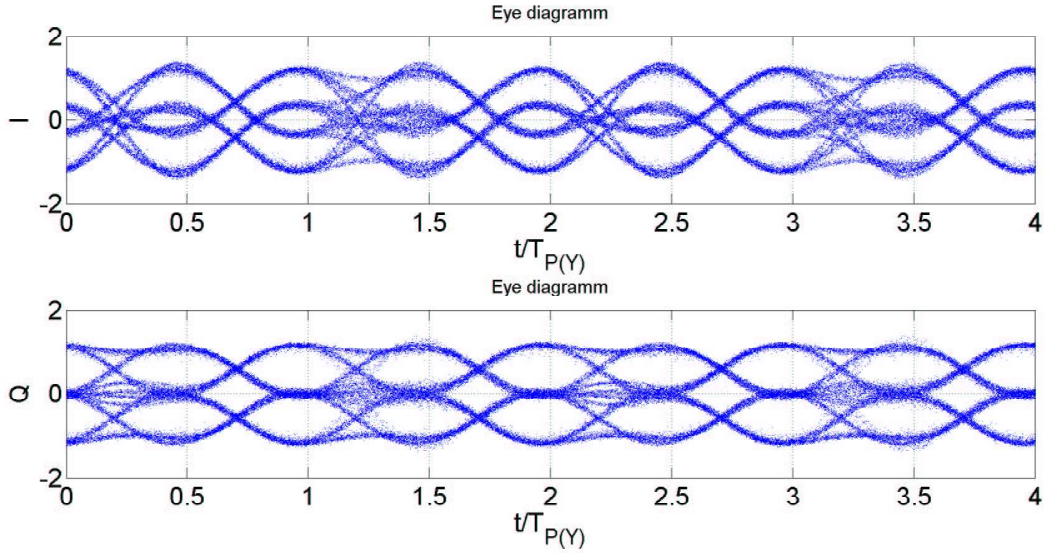

Figure 6.26: Eye diagram short time of GPS BIIRM6 L1 signal

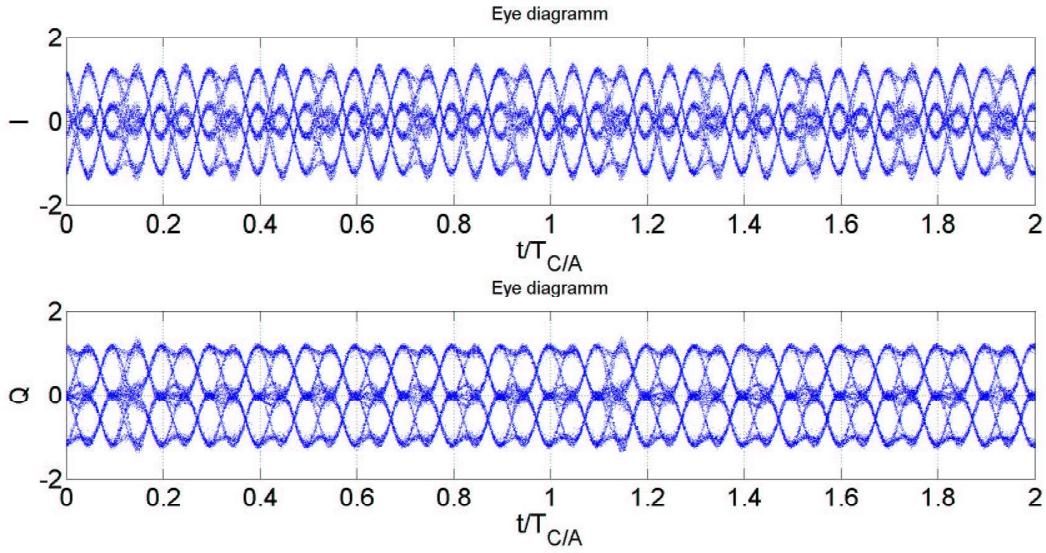

Figure 6.27: Eye diagram long time of GPS BIIRM6 L1 signal

From the definition of BOC(10,5), there are 20 subcarrier transitions in a period of C/A code ($k = \frac{2*10f_0}{f_0}$) , 2 subcarrier transitions for a period of P(Y) code ($k = \frac{2*10f_0}{10f_0}$) , and 4 subcarrier transitions for a period of itself ($k = \frac{2*10f_0}{5f_0}$). From the definition of BOC(10,10), which is the IM product, there are 2 subcarrier transitions in a period of itself ($k = \frac{2*10f_0}{10f_0}$). The number of subcarrier transitions to C/A and P(Y) are the same as by BOC(10,5).

First the in-phase component is determined in figure 6.26. The M code chip transitions are separated by 4 subcarrier, which associated the change $1.2 \rightarrow -0.3$, $-0.3 \rightarrow 1.2$, $-1.2 \rightarrow 0.3$ and $0.3 \rightarrow -1.2$. The transitions of P(Y) could be seen every 2 subcarrier transitions but without the transition of $1.2 \rightarrow 1.2$, $-1.2 \rightarrow -1.2$, which are the M code chip boundary.

The quadrature component in figure 6.27 is determined. The first overshoot is the beginning of the C/A code chip like in the old satellites, then count to 20 transitions of BOC(10,5) subcarrier,

there exists another overshoot. There are 2 subcarrier transitions between the code chip boundaries, which denote the component of IM product.

The interplex equation is rewritten for inspection

$$\begin{aligned} s(t) = \sqrt{2}(\sqrt{P_I}s_2(t)\cos(m) - \sqrt{P_Q}s_3(t)\sin(m))\cos(2\pi f_c t + \phi) \\ -\sqrt{2}(\sqrt{P_Q}s_1(t)\cos(m) + \sqrt{P_I}s_1(t)s_2(t)s_3(t)\sin(m))\sin(2\pi f_c t + \phi) \end{aligned} \tag{6.2}$$

Although the parameter m in the equation (6.2) is not set and the power in in-phase and quadrature is not known, we want to investigate the code and the transition in eye diagram.

Firstly we set the equation in in-phase part with the unknown parameter

$$coeff_{P(Y)} = \sqrt{2}\sqrt{P_I}\cos m \tag{6.3}$$

and

$$coeff_M = \sqrt{2}\sqrt{P_Q}\sin m \tag{6.4}$$

Then try out with the maximum value in in-phase eye diagram, which is approximately 1.2, and the value -0.3. Set $P(Y) = M = 1$ in the equation

$$1.2 = coeff_{P(Y)}P(Y) - coeff_M M \tag{6.5}$$

and set $P(Y) = 1$ and $M = -1$ in the equation

$$-0.3 = coeff_{P(Y)}P(Y) - coeff_M M \tag{6.6}$$

After solving the equations the $coeff_{P(Y)}$ is equal to 0.45, and $coeff_M$ is equal to -0.75.

The figure 6.28 shows the eye diagram simulated with MATLAB. The transitions of the simu-

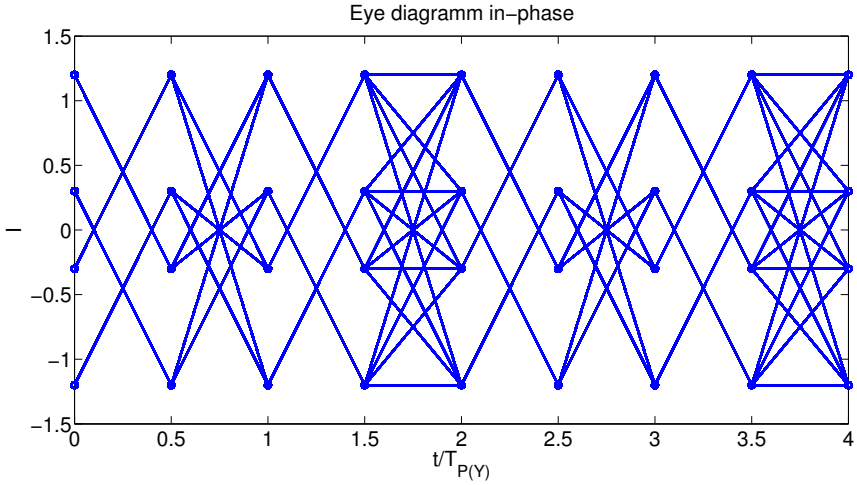

Figure 6.28: In-phase eye diagram short time of the simulated L1 signal

lation correspond to the transitions in the in-phase eye diagram of figure 6.26.

Secondly we set the equation in quadrature part with the unknown parameter

$$coeff_{C/A} = \sqrt{2}\sqrt{P_Q}\cos m \tag{6.7}$$

and

$$coeff_{IM} = \sqrt{2}\sqrt{P_I}\sin m \tag{6.8}$$

Then try out with the maximum value in quadrature eye diagram, which is approximately 1.2, and the value 0. Set $C/A = 1$ and $IM = -1$ in the equation

$$1.2 = -(coeff_{C/A}C/A + coeff_{IM}IM) \tag{6.9}$$

and set $C/A = IM = 1$ in the equation

$$0 = -(coeff_{C/A}C/A + coeff_{IM}IM) \tag{6.10}$$

After solving the equation the $coeff_{C/A}$ is equal to -0.6, and $coeff_{IM}$ is equal to 0.6.

The figure 6.29 shows the eye diagram simulated with MATLAB. The transitions of the simu-

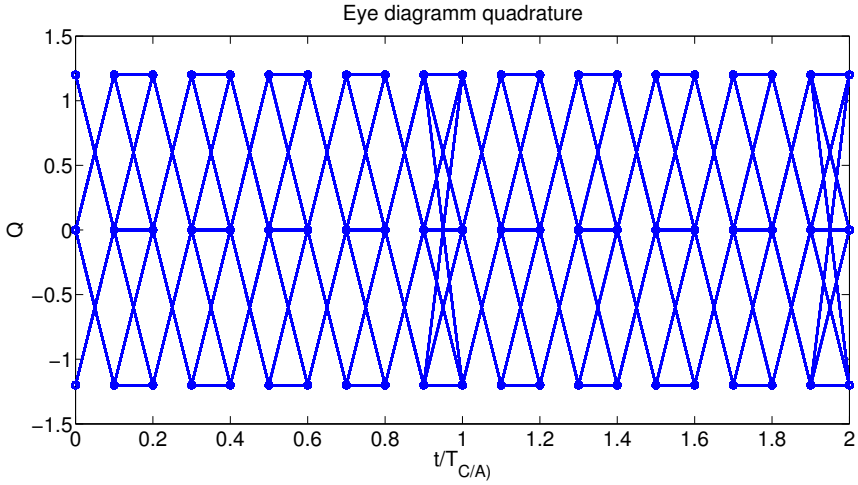

Figure 6.29: Quadrature eye diagram long time of the simulated L1 signal

lation correspond to the transitions in the quadrature eye diagram of figure 6.27.

Thereafter the simulated in-phase and quadrature signals are plotted, that results the IQ diagram as seen in figure 6.30. The simulated IQ diagram corresponds to the measurement IQ diagram, which has 6 ideal points. It must be noted that all the simulation are derived from the estimated

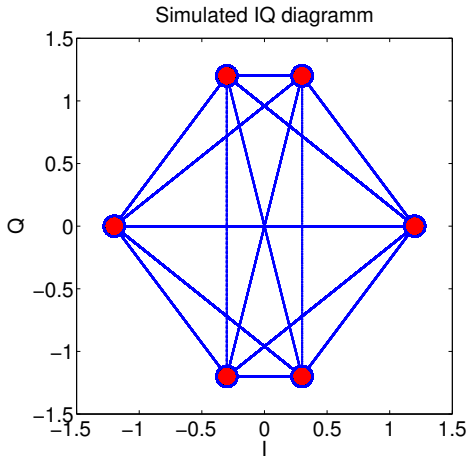

Figure 6.30: Simulated IQ diagram

values. If the exact values can be detected, the parameter m can be solved from the equation.

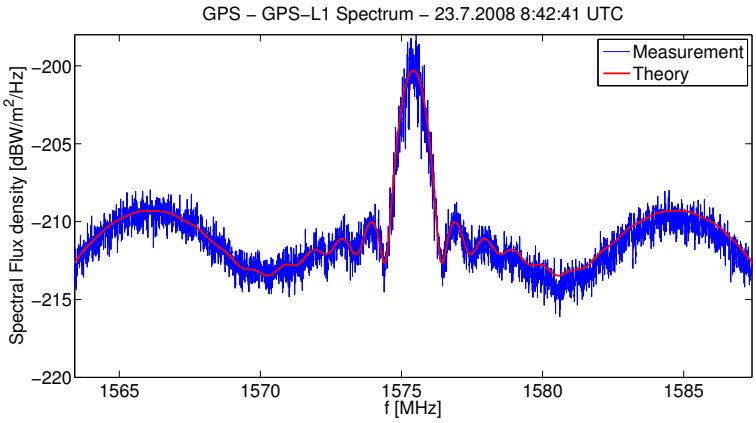

Figure 6.31: Measurement signal compared with theory of GPS BIIRM6 L1 signal

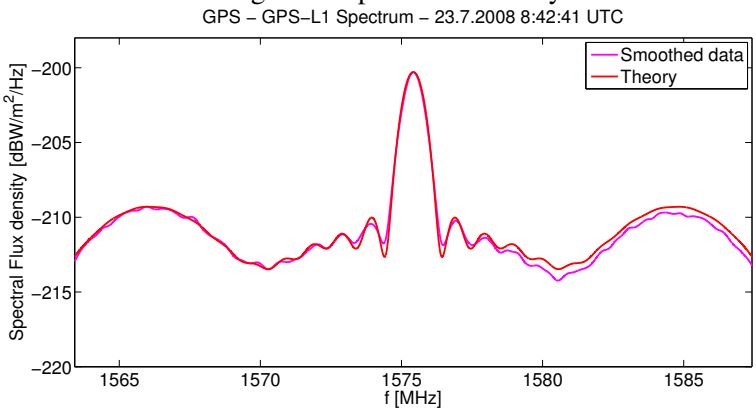

Figure 6.32: Smoothed measurement signal compared with theory of GPS BIIRM6 L1 signal

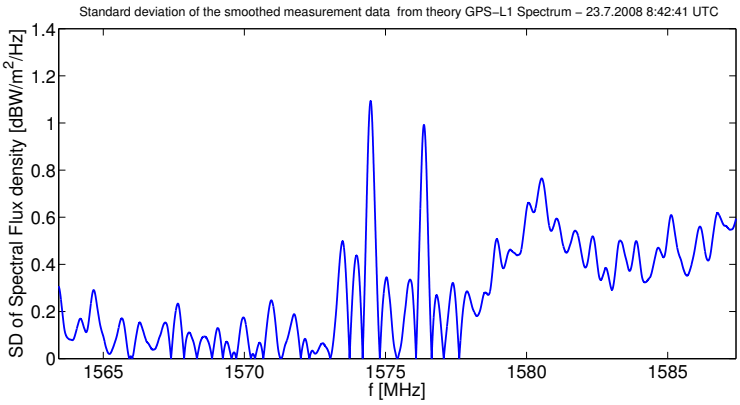

Figure 6.33: SD of the smoothed measurement signal and theory of GPS BIIRM6 L1 signal

In Fig 6.31 and 6.32 the measurement and theoretical signal are compared, the interested bandwidth is 1563.42 MHz - 1587.42 MHz which is the 24 MHz bandwidth of GPS L1. The spectral power densities show asymmetries where the left side of the center frequency has more power than the right side. The standard deviation of the smoothed signal and theoretical signal shows that the right side band deviates from the theoretical signal, because the curve scaling are solved with the left side band.

6.4 GPS BIIR12 L1 with Elevation Plot

The set of BIIR12 L1 measurement data are recorded from 14.00 UTC to 20.00 UTC on 23 January 2009. The EIRP is calculated and plotted over the elevation angle.

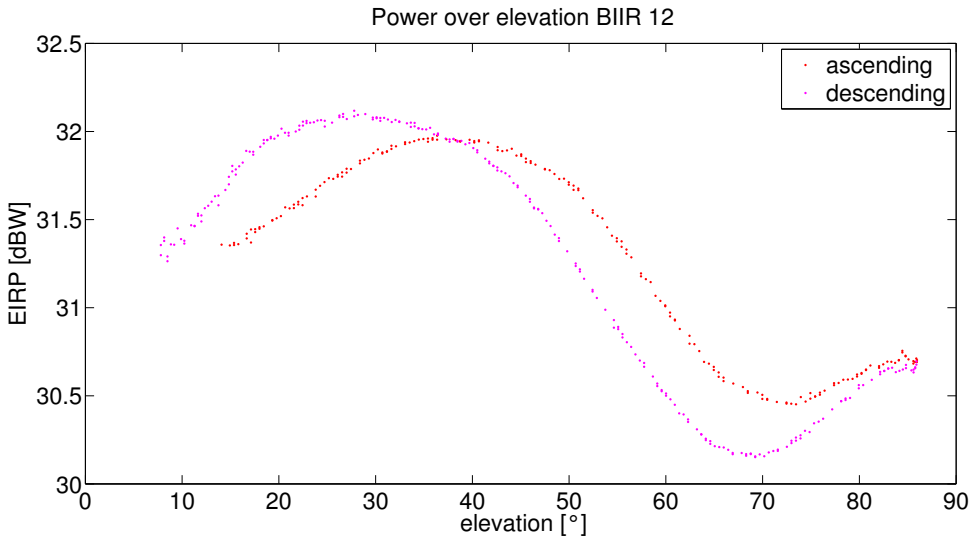

Figure 6.34: GPS BIIR12 L1 power over elevation plot

The maximum EIRP power was measured with 32.12 dBW at an elevation of 27.78° as the satellite is descending. The minimum EIRP is 30.15 dBW at an elevation of 69.23° also as the satellite is descending. The curve looks like an s-shape that after the minimum power the power increases until the maximum elevation reached.

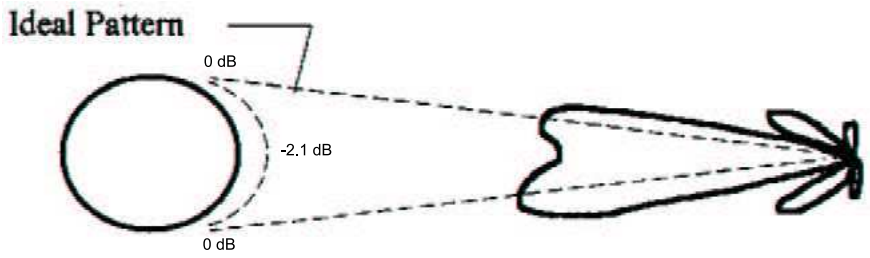

Figure 6.35: Ideal antenna pattern (Source:[35])

It is written in [33], that the path loss is minimum at 90° elevation and maximum at the horizon. The difference in path loss caused by the variation in path length is about 2.1 dB as shown in figure 6.35. The users should receive maximum signal when the satellite is approximately at an elevation of 40°.

In figure 6.34 the maximum signal power at around 40° elevation as the satellite is ascending corresponds to the theory. But as the satellite is descending, the maximum signal is not at 40° elevation, which could be due to the satellite path that does not pass the zenith and causes the variation in azimuth and range as seen in figure 6.36 and 6.37.

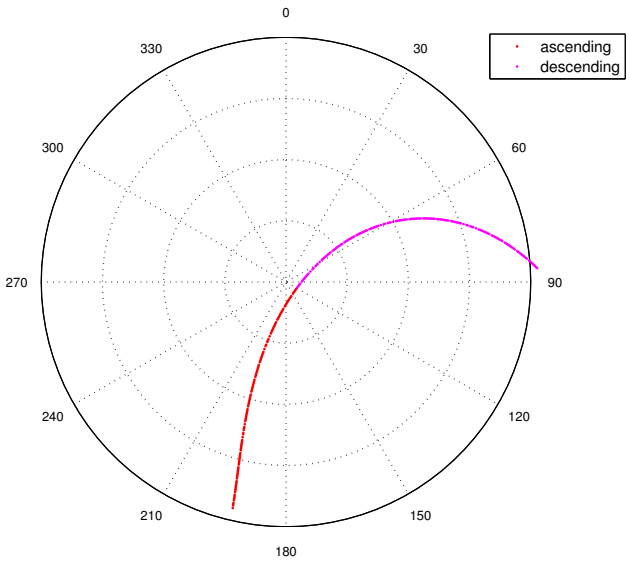

Figure 6.36: Elevation over azimuth on polar plot

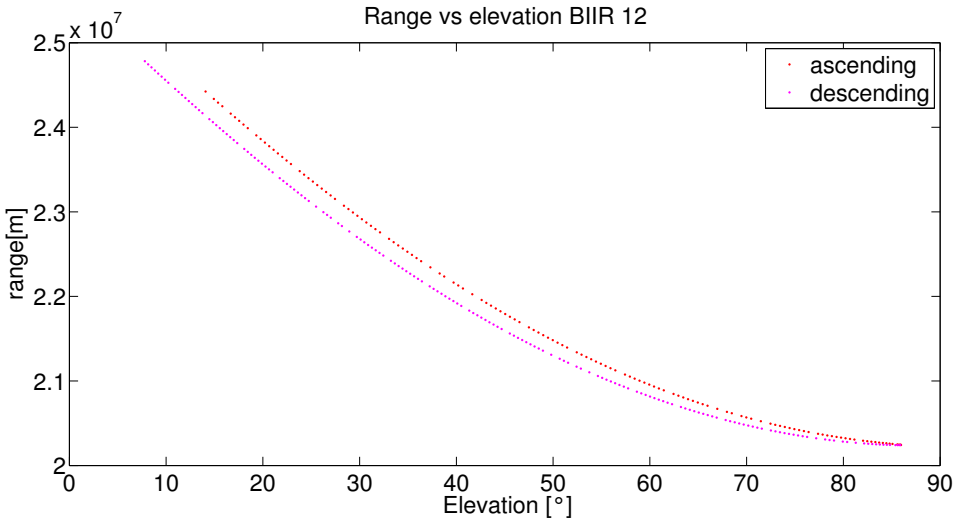

Figure 6.37: Range over elevation

In figure 6.37 the difference between the range of the ascending and descending satellite at elevation of 30° is about 240 km, which is enough to cause the difference of the power signal of ascending and descending satellite.

As described in [35] the antenna gain of the GPS L-band satellite antenna, which consists of two concentric rings of elements, depends on the phase angle between the outer and inner elements ϕ. The maximum gain is achieved in a plane that is defined by the plane that intersects two elements of the center quad. The minimum is in the plane that is 45° from maximum.

The other two actions that produce slight variations in gain are the Noon turn maneuver around the nadir axis, which keeps the space vehicle's solar arrays in a sun-pointing orientation, and the effect of the position of the solar arrays that the angle between the bulkhead and the solar array changes as the solar array tracks the sun. These actions cause the satellite to rotate around the z-axis, which is the antenna direction pointing toward the earth, called yaw angle.

Figure 6.38 and 6.39 show the yaw angle over the azimuth and elevation respectively. It can be seen that after 70˚ elevation as the satellite is descending the yaw angle changes dramatically from around 300˚ to around 160˚. This change causes the difference of the antenna gain pattern as described in [35].

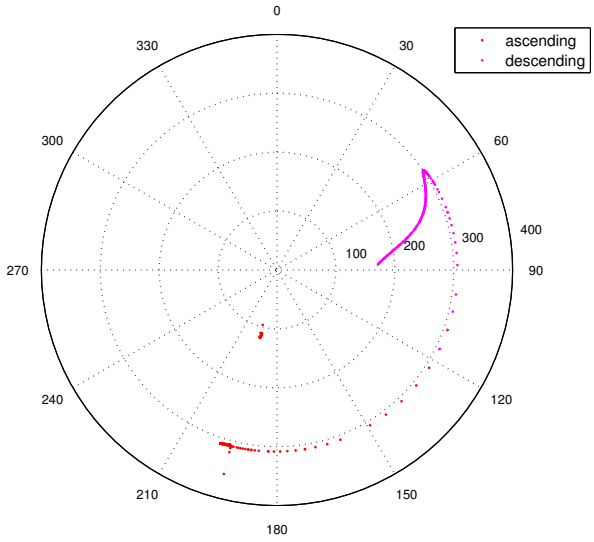

Figure 6.38: yaw angle over the azimuth

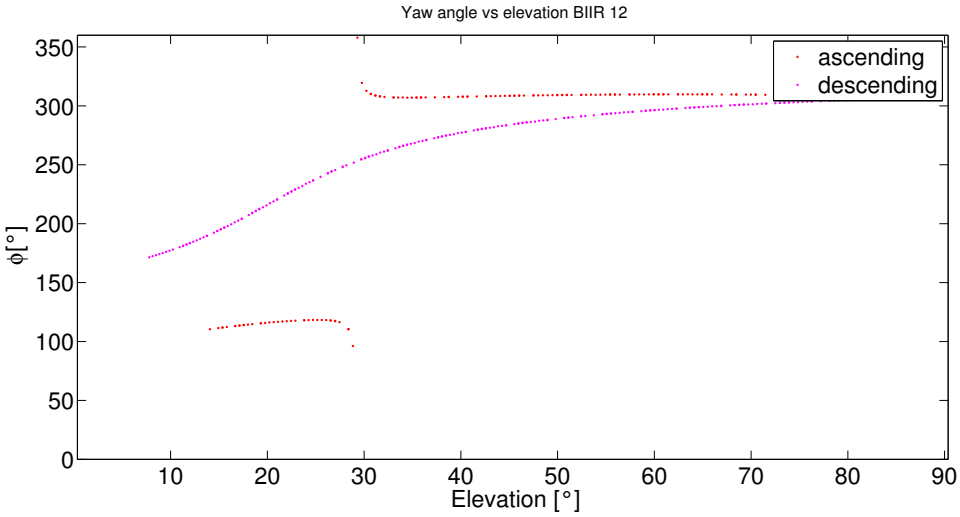

Figure 6.39: yaw angle over elevation

All the facts mentioned above can be the causes of the variation in the power signal between satellite ascending and descending.

In figure 6.41 the antenna pattern of L1 GPS BIIR12 is compared with the theoretical gain pattern from [35] fitted at 10˚ nadir angle. The antenna pattern is not well fitted to the theoretical gain pattern. It must be noted that the theoretical pattern is based on the Block I NAVSTAR GPS L-band antenna, which is the old generation of GPS satellite.

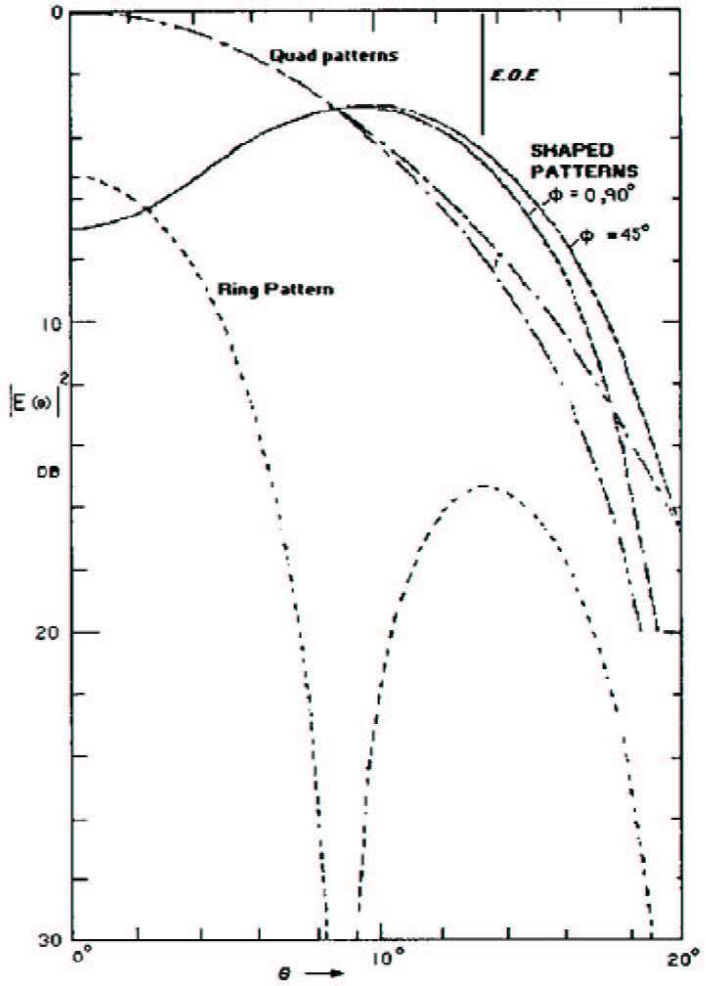

Figure 6.40: Inner, outer, and composite antenna gain pattern(Source:[35])

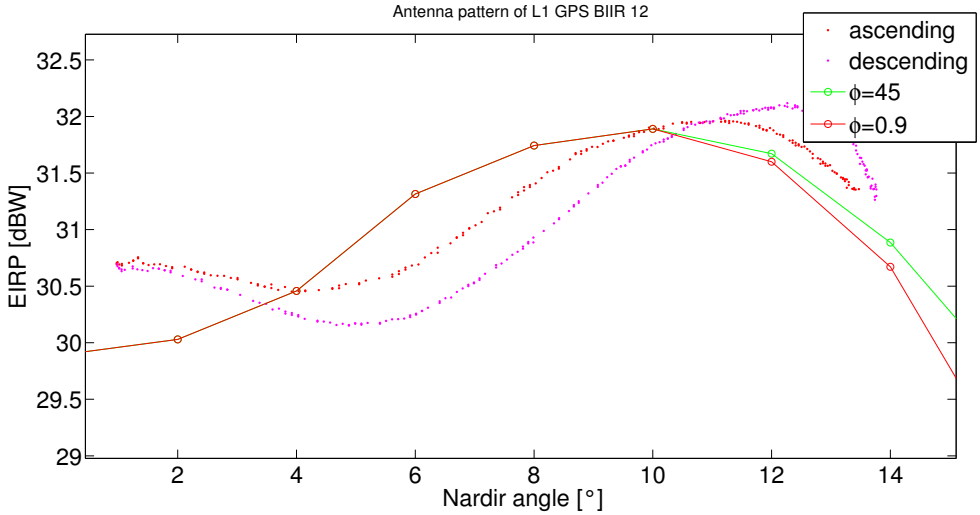

Figure 6.41: Antenna pattern compared to the theoretical antenna gain pattern from [35]

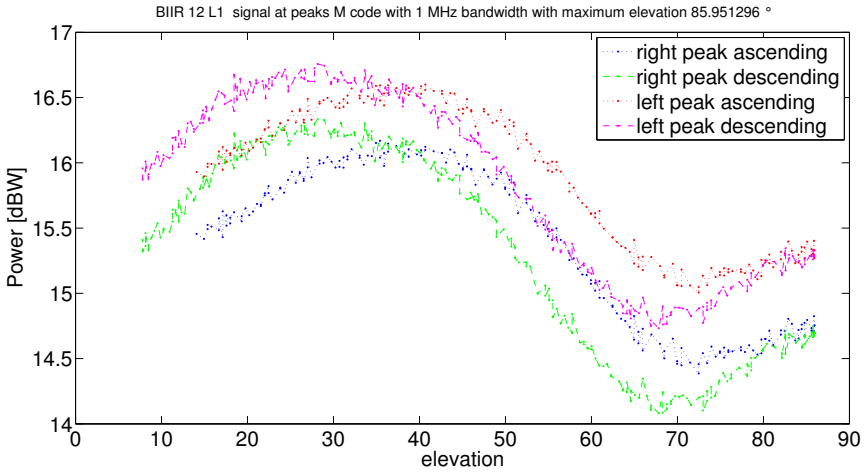

Figure 6.42: GPS BIIR12 L1 signal of 1 MHz bandwidth at 5.115 MHz right and left from center bandwidth over elevation plot

The figure 6.42 shows the left side band has about 2 dB more power than the right side band for all the period of record. The curve has the same shape as the plot in figure 6.34.

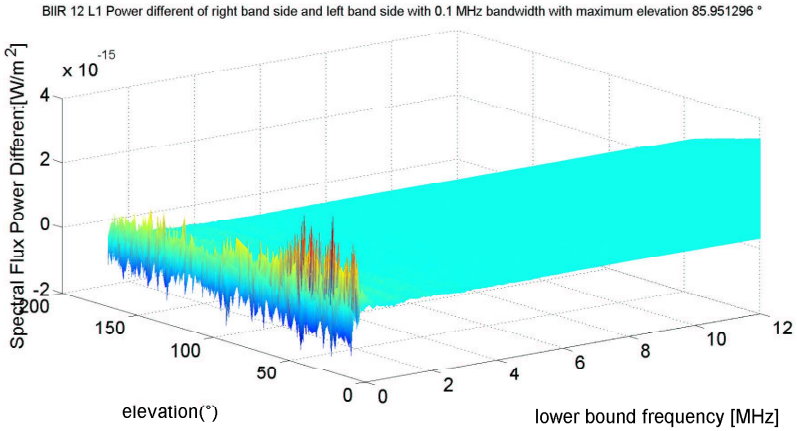

Figure 6.43: GPS BIIR12 L1 spectrum asymmetry plot with elevation

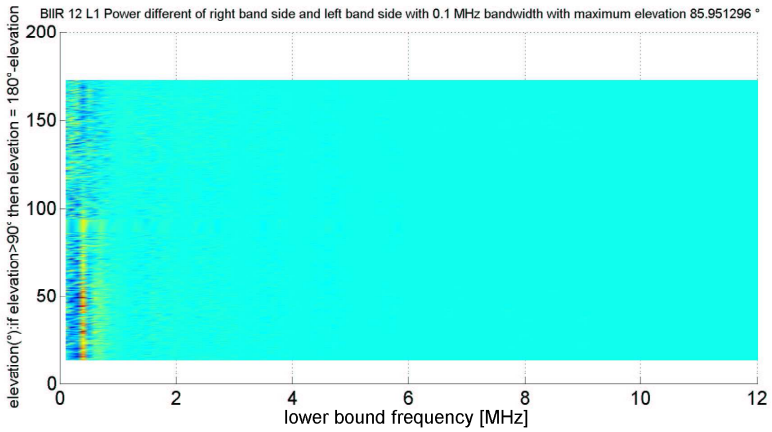

Figure 6.44: GPS BIIR12 L1 spectrum asymmetry plot with elevation top view

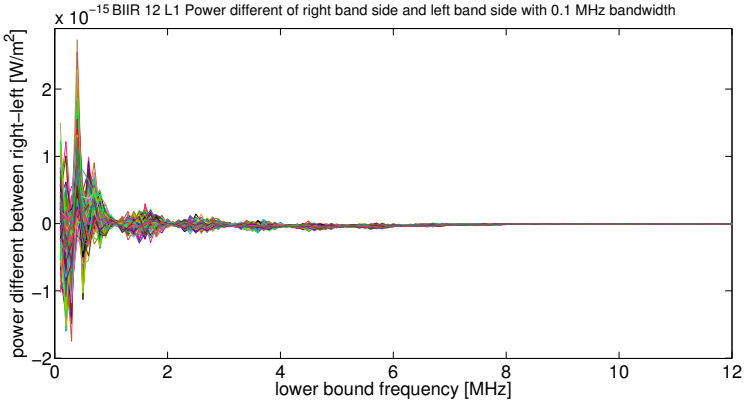

Figure 6.45: GPS BIIR12 L1 spectrum asymmetry plot with elevation side view

Figures 6.43 - 6.45 show that the power asymmetry is more around the center frequency and decreases to the frequency bound.

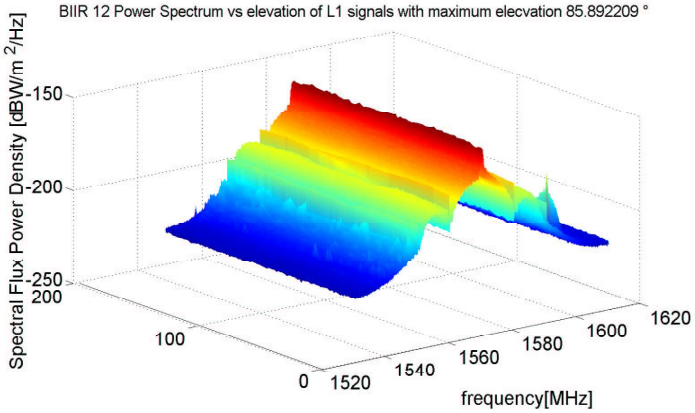

Figure 6.46: GPS BIIR12 L1 power spectral density plot with elevation

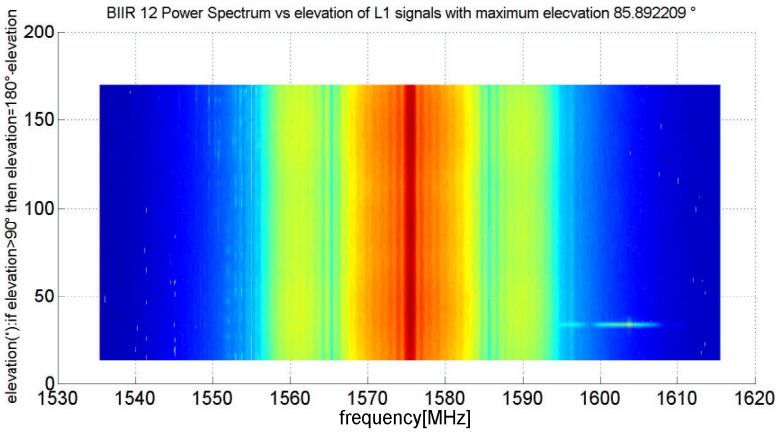

Figure 6.47: GPS BIIR12 L1 power spectral density plot with elevation top view

At last the power spectral density is plotted with elevation. With this plot, the purity of signal can be observed for the time of recorded. It can be seen that there is also out of band interference at elevation of 40°. But in the bandwidth of L1 the signal looks clean.

6.5 GPS BIIRM6 L1 with Elevation Plot

The set of BIIRM6 L1 measurement data are recorded from 16.30 UTC to 22.30 UTC on 27 January 2009. The EIRP are calculated and plotted over the elevation angle. The maximum EIRP

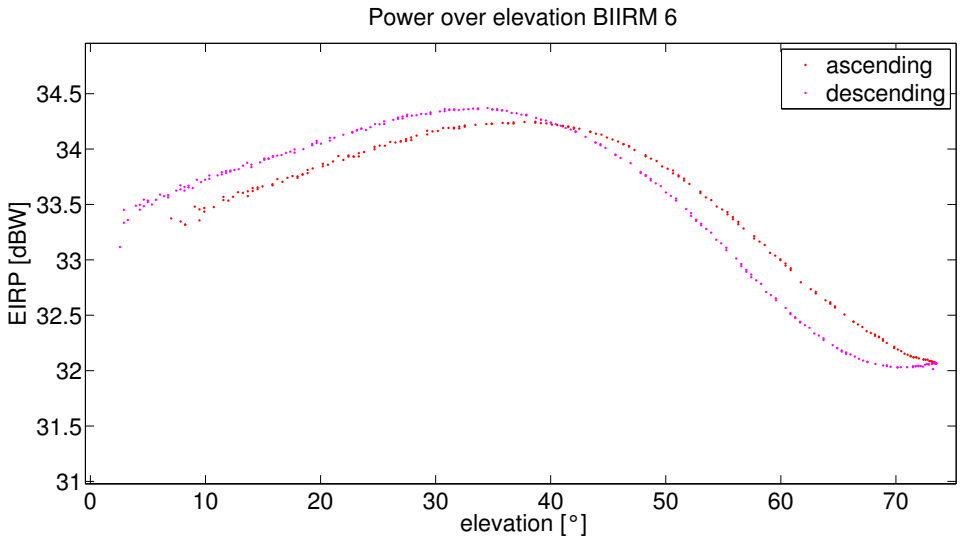

Figure 6.48: GPS BIIRM6 L1 power over elevation plot

power was measured with 34.37 dBW at an elevation of 34.51° as the satellite is descending. The minimum EIRP is 32.01 dBW at an elevation of 73.23° also as the satellite is descending.

The maximum and minimum power difference of the measurement is approximately 2.36 dB which is not much different from theory, which said that the different of the maximum and minimum power is around 2.1 dB due to the path loss.

The maximum signal as the satellite is ascending at around 40° corresponds to the theory. But as the satellite is descending, it does not correspond to the theory, which could be due to the satellite path that does not pass the zenith and causes the variation in azimuth and range as seen in figure 6.49 and 6.50.

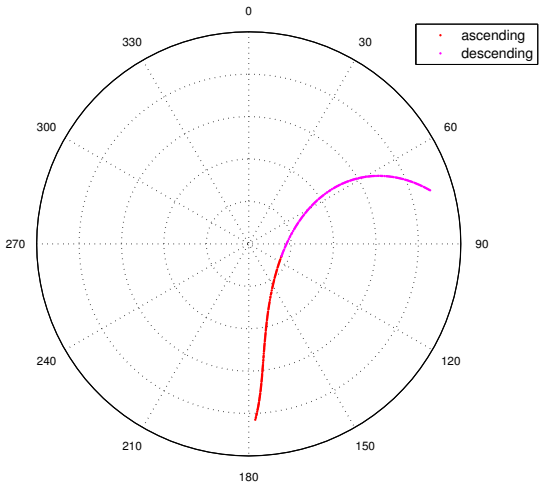

Figure 6.49: Elevation over azimuth on polar plot

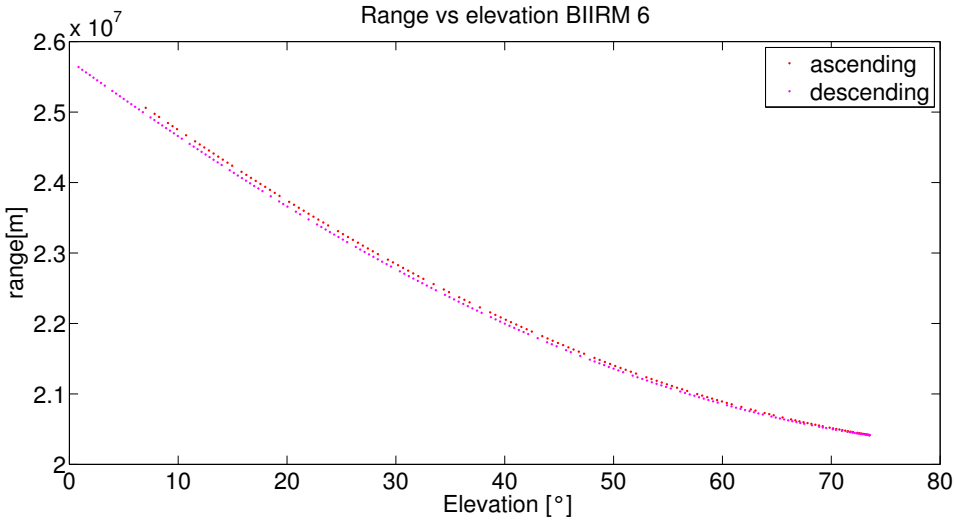

Figure 6.50: Range over elevation

The variation of the azimuth can cause the variation of the range. In figure 6.50 the range difference of the descending and the ascending satellite at each elevation is around 60 km, which is not as much as of BIIR12 satellite.

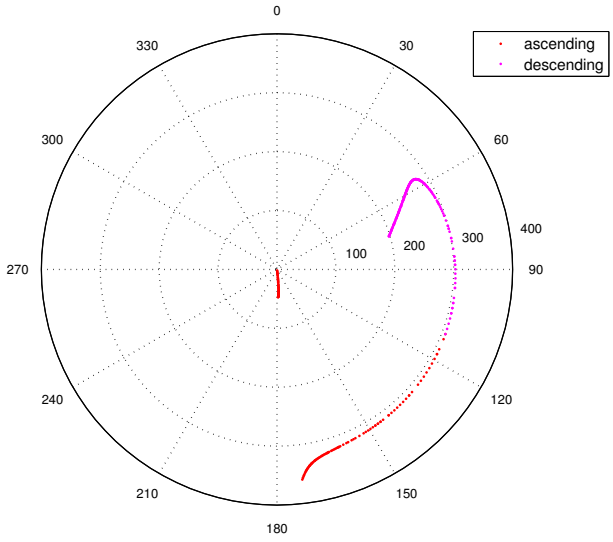

Figure 6.51: Yaw angle over the azimuth

Figure 6.51 and 6.52 show the yaw angle over the azimuth and elevation respectively. The yaw angle is the angle of satellite's rotation around the z-axis as the satellite tracks the sun. The z-axis is the antenna direction pointing toward the earth.

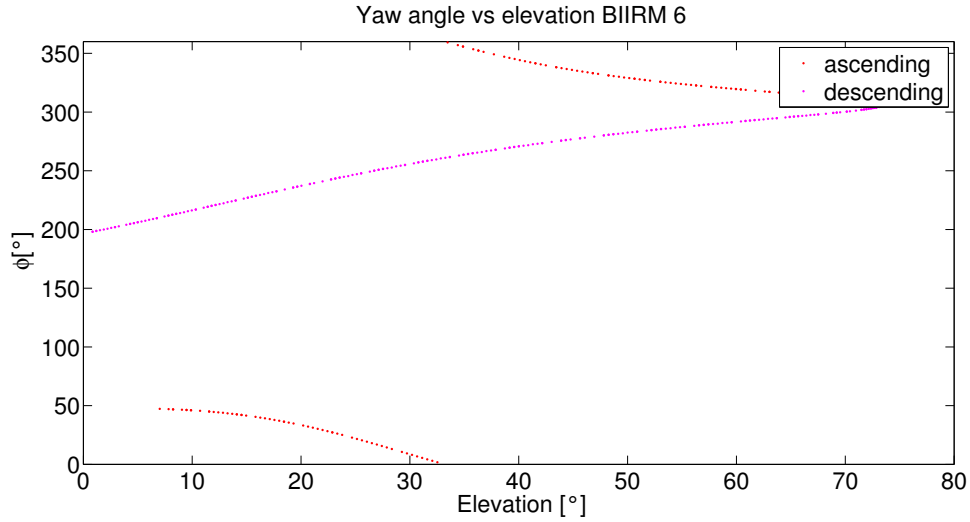

Figure 6.52: Yaw angle over the elevation

It can be seen that the yaw angle of this satellite changes continuously. The discontinuity at the elevation of 32.52° is only due to the interval of 2π. The change of the yaw angle causes the difference of the antenna gain pattern as described in [35].

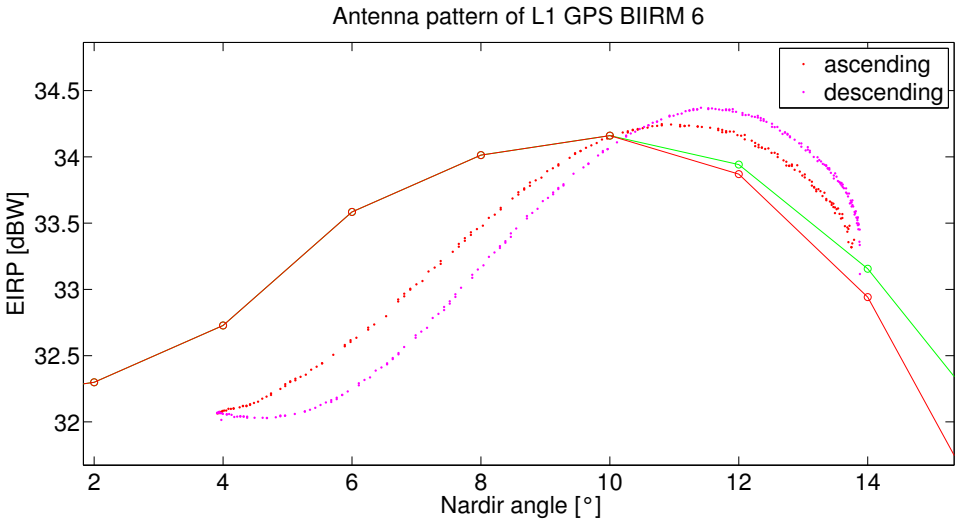

Figure 6.53: GPS BIIRM6 L1 antenna pattern

In figure 6.53 the antenna pattern compared with the theoretical pattern [35] fitted at nadir angle of 10° is shown. The antenna pattern is not well fitted to the theoretical gain pattern. It must be noted that the theoretical pattern is based on the Block I NAVSTAR GPS L-band antenna, which is the old generation of GPS satellite.

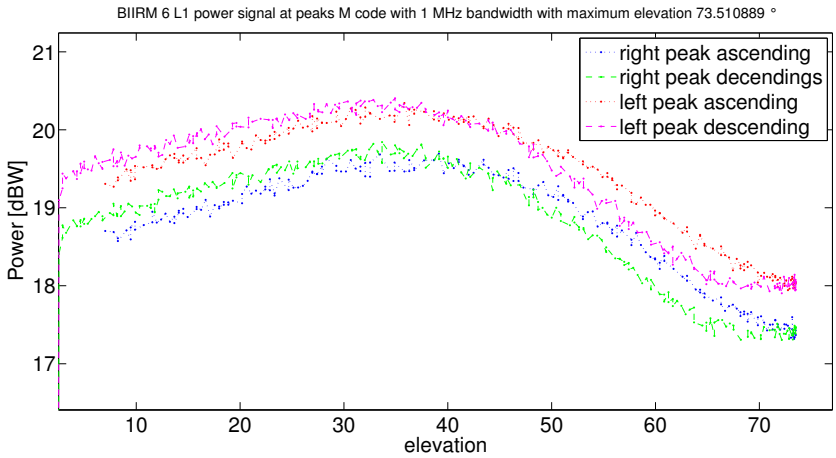

Figure 6.54: GPS BIIRM6 L1 power signal 1 MHz bandwidth at the right and left M code peak

The figure 6.54 shows the left M code peak has about 0.5 dB more power than the right M code peak for all the period of record. The curve has the same shape as the plot in figure 6.48

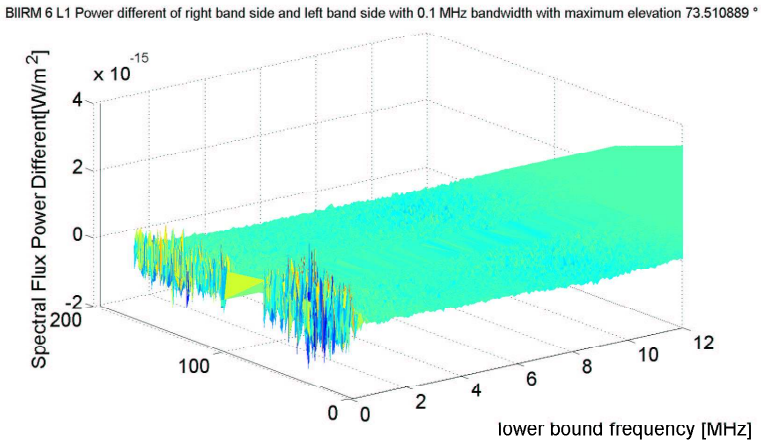

Figure 6.55: GPS BIIRM6 L1 spectrum asymmetry plot with elevation

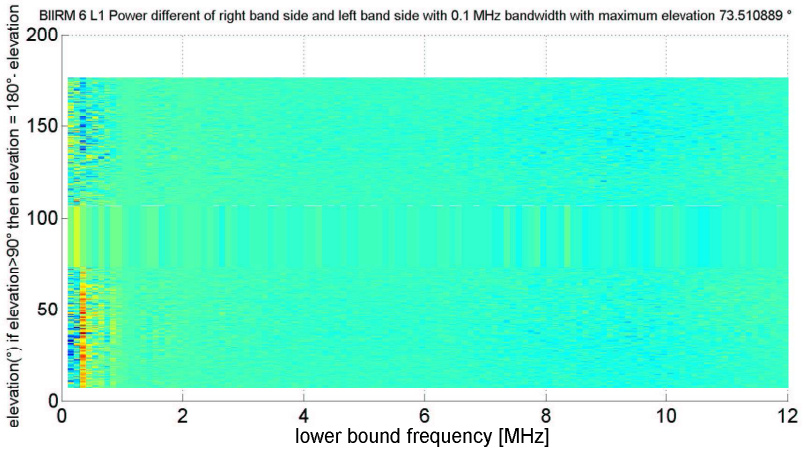

Figure 6.56: GPS BIIRM6 L1 spectrum asymmetry plot with elevation top view

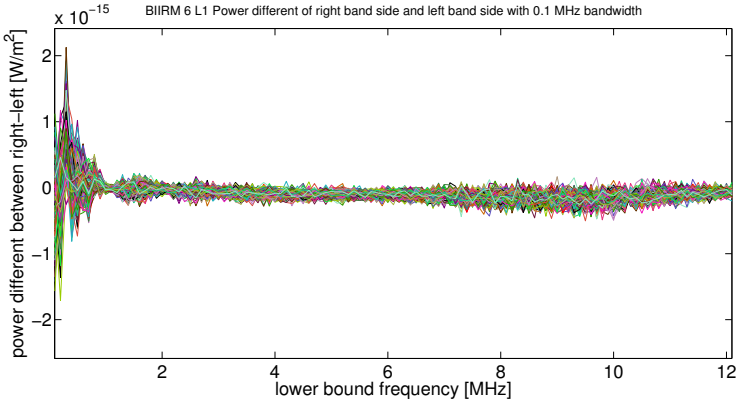

Figure 6.57: GPS BIIRM6 L1 spectrum asymmetry plot with elevation side view

In figures 6.55- 6.57 the asymmetry of the spectrum are determined. The difference is mostly around the center frequency to the frequency of 1 MHz. At the peak of M code, which lie 10 MHz from the center frequency, is some power difference to be seen.

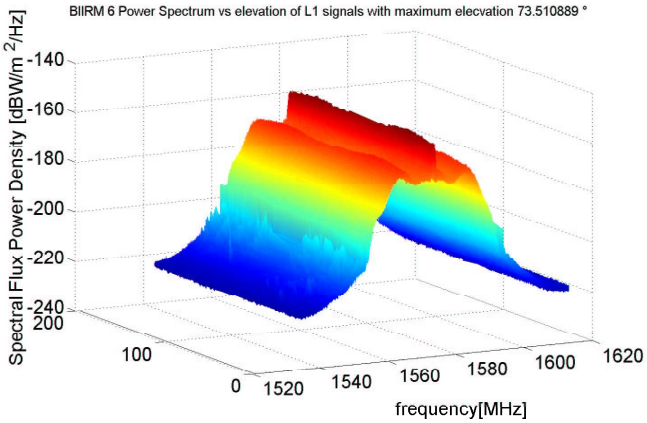

Figure 6.58: GPS BIIRM6 L1 power spectral density plot with elevation

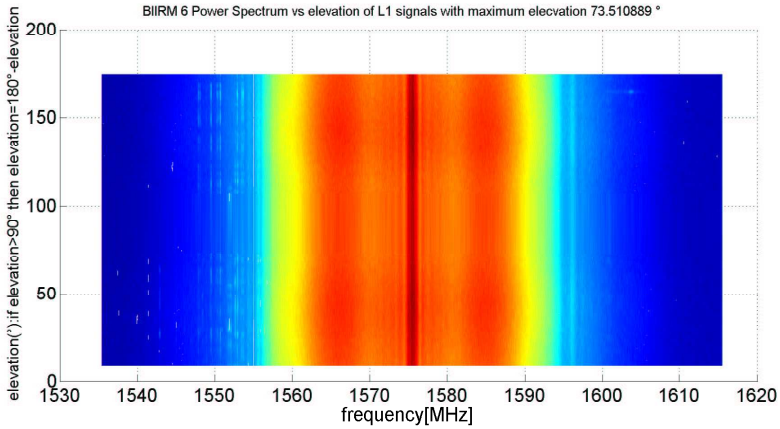

Figure 6.59: GPS BIIRM6 L1 power spectral density plot with elevation top view

At last the power spectral density is plotted with elevation. The signal looks clean in the L1 band for the time of record. Out of the band there are some other interference signals to be seen.

7. Analysis with Filtering

The filters are applied in many stages of signal receiver before the baseband signal is produced. It is useful to know which effect the filters have to the received signal, in which the spectrum, the IQ constellation, the correlation function and discriminator are determined.

The processing is done from the measurement signal which already band-limited and down-mixing to baseband, therefore the filter researched here is actually designed to be low-pass filter half bandwidth of the stated name of band-pass filter. The test data is always from BIIR12 L1 signal for which the ideal constellation is known in order to be able to check for the error vector magnitude. First the original data and spectrum are shown. The bandwidth of the received signal is 40 MHz pre-filtered.

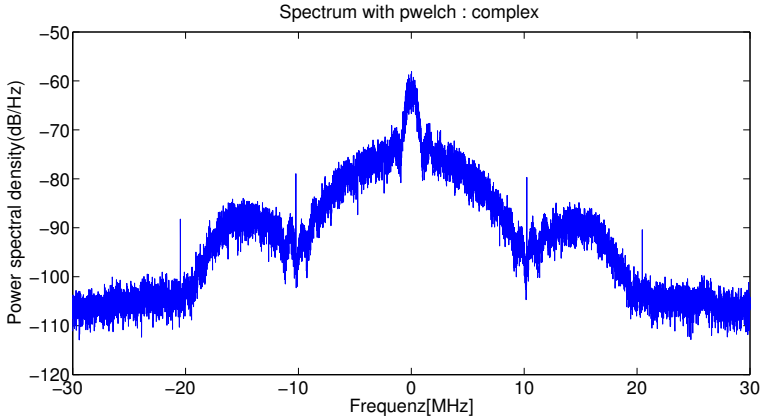

Figure 7.1: Power Spectrum of IQ data measurement

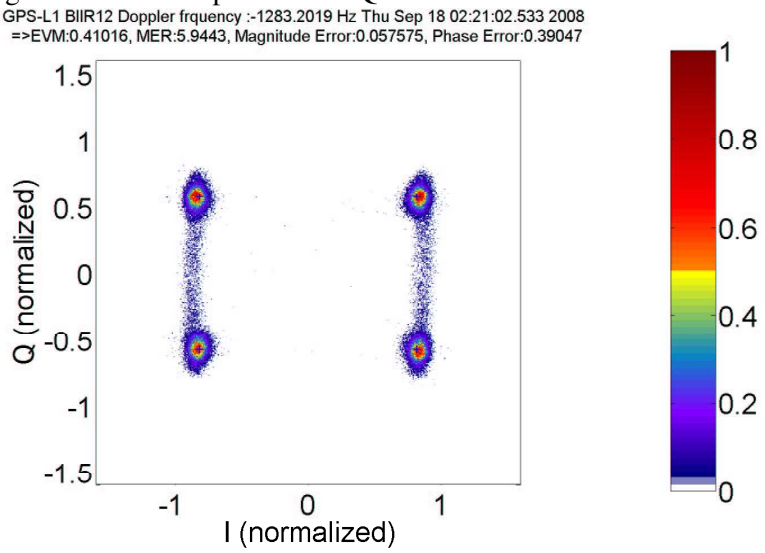

Figure 7.2: IQ constellation of GPS BIIR12 L1

7.1 GPS BIIR12 L1 with Chebychef Filtering

The first filter examined is Chebychef filter of order 9 with different cut off frequency of 20, 10, 5 and 2 MHz. The group delay of these filter are not constant, which means the filtered signal are phase distorted by the filter. The entire IQ constellations in this chapter are normalized with the maximum value of IQ constellation before filtering.

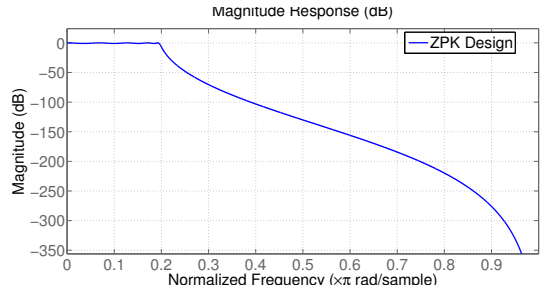

Figure 7.3: Magnitude response of the 9th order Chebychef filter with cut of frequency 20 MHz

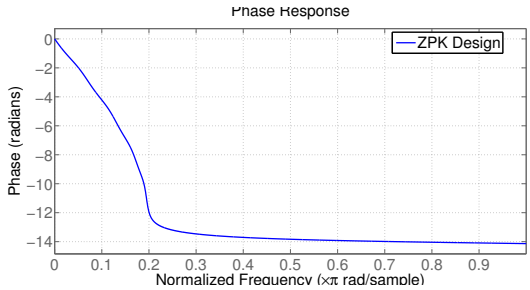

Figure 7.4: Phase response of the 9th order Chebychef filter with cut of frequency 20 MHz

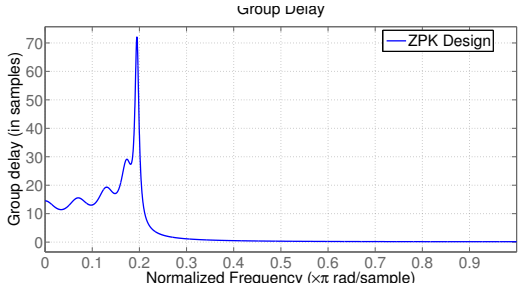

Figure 7.5: Group delay of the 9th order Chebychef filter with cut of frequency 20 MHz

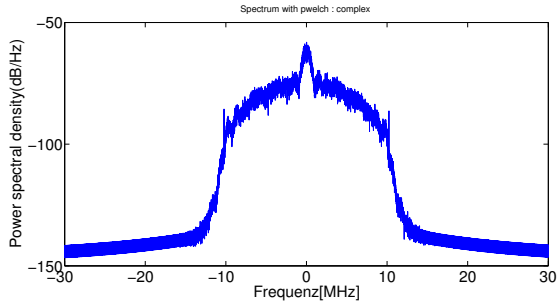

Figure 7.6: Power spectrum of IQ data filtered with 9th order Chebychef filter cut of frequency 20 MHz

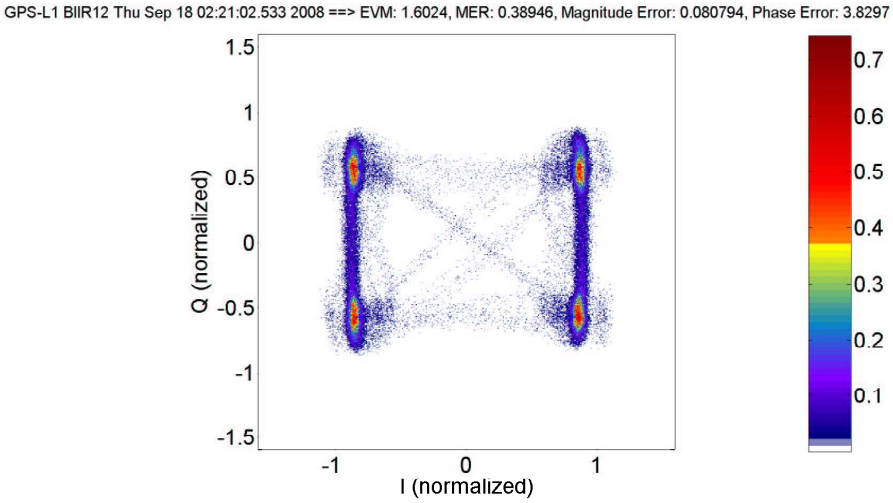

Figure 7.7: IQ constellation of GPS BIIR12 L1 signal filtered with Chebychef filter with cut of frequency 20 MHz normalized with maximum value before filtering

With 20 MHz filter, the main lobes of the P(Y) and C/A code can be seen. The constellation is distorted by the filter; however the ideal constellation points are still able to be recognized. The transitions between the points are intensified, since some of the energy with more rates is cut out, so the points move more slowly. The error vector magnitude increases accordingly.

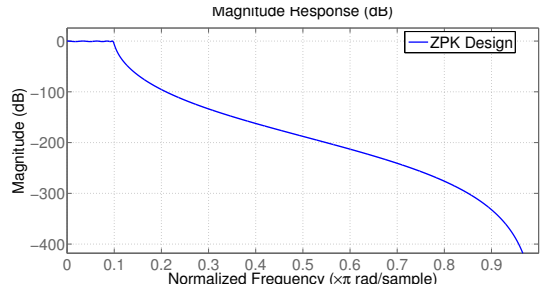

Figure 7.8: Magnitude response of the 9th order Chebychef filter with cut of frequency 10 MHz

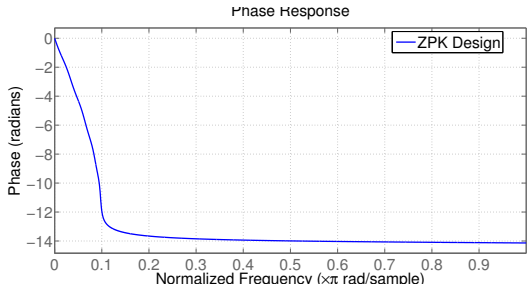

Figure 7.9: Phase response of the 9th order Chebychef filter filter with cut of frequency 10 MHz

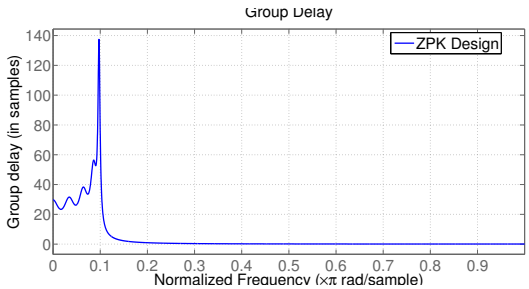

Figure 7.10: Group delay of the 9th order Chebychef filter filter with cut of frequency 10 MHz

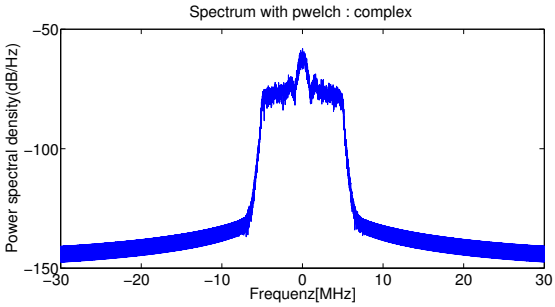

Figure 7.11: Power Spectrum of IQ data filtered with 9th order Chebychef filter cut of frequency 10 MHz

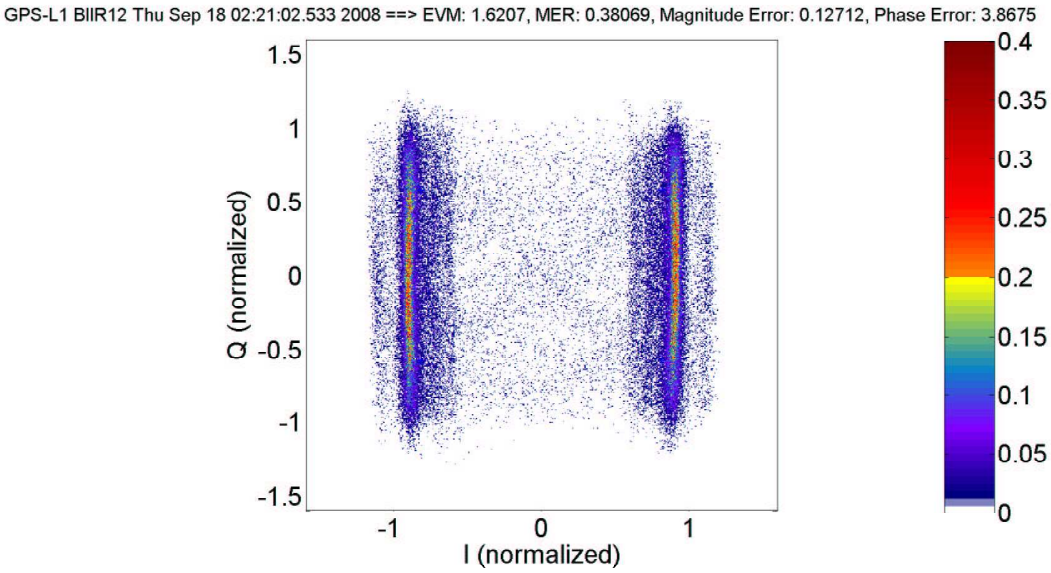

Figure 7.12: IQ constellation of GPS BIIR12 L1 signal filtered with Chebychef filter with cut of frequency 10 MHz normalized with maximum value before filtering

With 10 MHz filter some of the main-lobe of P(Y) code is cut off, therefore the transition in the quarature phase cannot be verified and look like two lines without ideal points. The EVM increases accordingly.

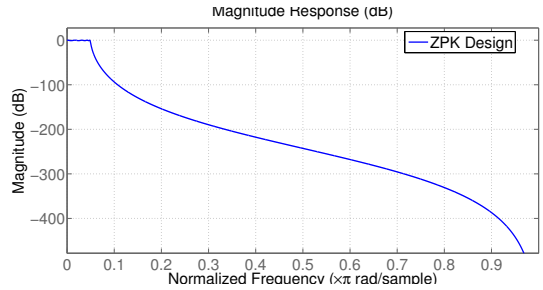

Figure 7.13: Magnitude response of the 9th order Chebychef filter with cut of frequency 5 MHz

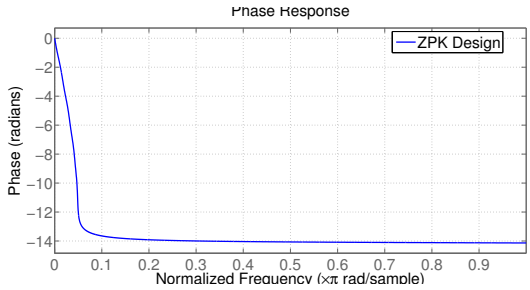

Figure 7.14: Phase response of the 9th order Chebychef filter with cut of frequency 5 MHz

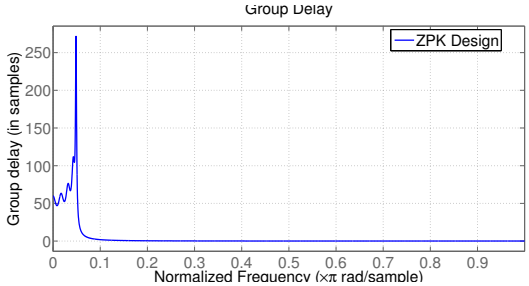

Figure 7.15: Group delay of the 9th order Chebychef filter with cut of frequency 5 MHz

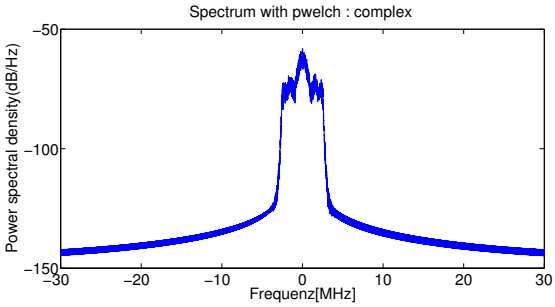

Figure 7.16: Power Spectrum of IQ data filtered with 9th order Chebychef filter cut of frequency 5 MHz

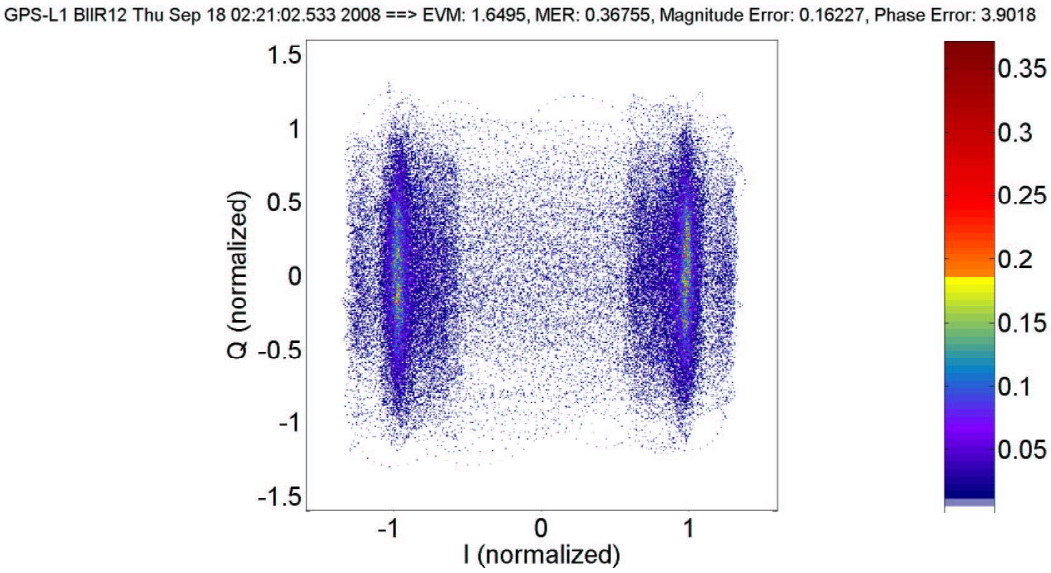

Figure 7.17: IQ constellation of GPS BIIR12 L1 signal filtered with Chebychef filter with cut of frequency 5 MHz normalized with maximum value before filtering

With 5 MHz filter the main-lobe of the P(Y) code is more cut off, therefore the IQ constellation is more distorted and the points are more scatter. The EVM increases accordingly.

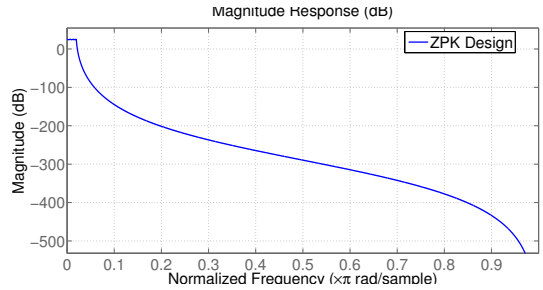

Figure 7.18: Magnitude response of the 9th order Chebychef filter with cut of frequency 2 MHz

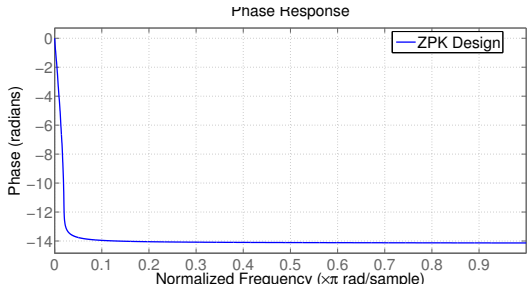

Figure 7.19: Phase response of the 9th order Chebychef filter with cut of frequency 2 MHz

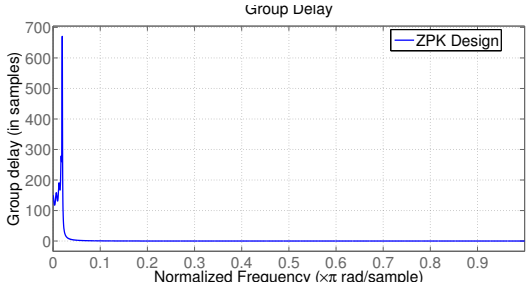

Figure 7.20: Group delay of the 9th order Chebychef filter with cut of frequency 2 MHz

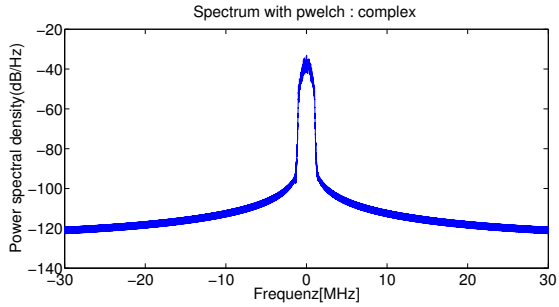

Figure 7.21: Power Spectrum of IQ data filtered with 9th order Chebychef filter cut of frequency 2 MHz

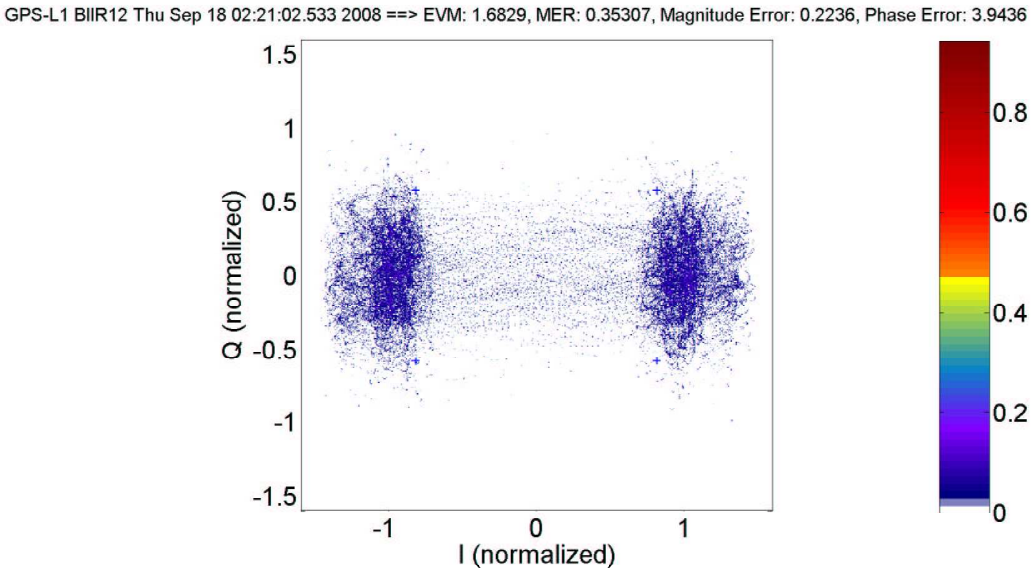

Figure 7.22: IQ constellation of GPS BIIR12 L1 signal filtered with Chebychef filter with cut of frequency 2 MHz normalized with maximum value before filtering

With 2 MHz low-pass filter the main-lobe of the P(Y) code is mostly cut off. Actually some of the P(Y) is still there but it is sheltered by the C/A power. The transition in the quadrature phase cannot be observed and also the constellation points. However the in-phase still can be bounded. The EVM is maximized, because the signal is the most distorted.

Figures 7.23- 7.30 show the IQ diagram from side view in order to investigate the distribution of the signal for each filter bandwidth. The power of the signals is decreased due to filtering. The IQ constellation is scattered away from the ideal points. The in-phase signal can be decided down to bandwidth of 2 MHz because the main lobe of the signal still exists after filtering in contrast to quadrature signal, which could not be recognized for filtering narrower than of 20 MHz.

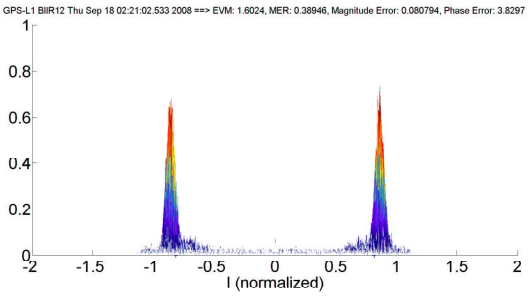

Figure 7.23: IQ diagram with Chebychef filter 20 MHz looking from in-phase side

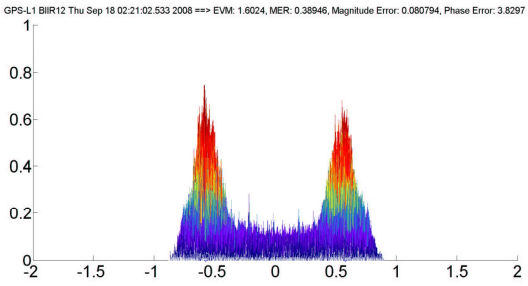

Figure 7.24: IQ diagram with Chebychef filter 20 MHz looking from quadrature side

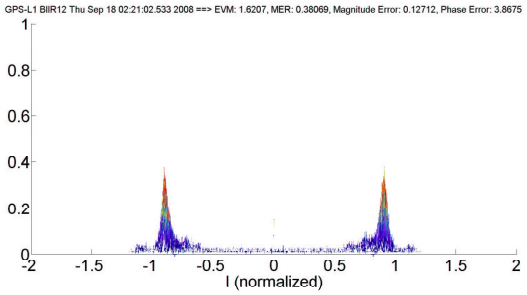

Figure 7.25: IQ diagram with Chebychef filter 10 MHz looking from in-phase side

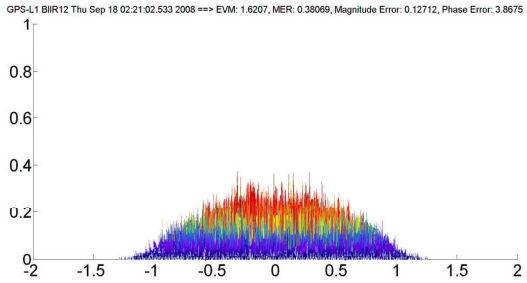

Figure 7.26: IQ diagram with Chebychef filter 10 MHz looking from quadrature side

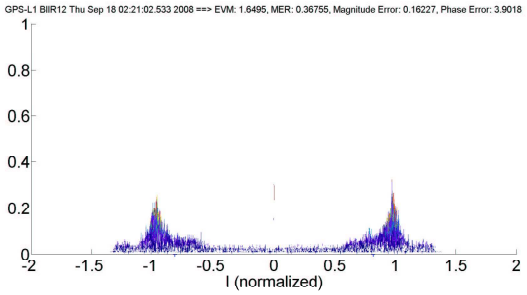

Figure 7.27: IQ diagram with Chebychef filter 5 MHz looking from in-phase side

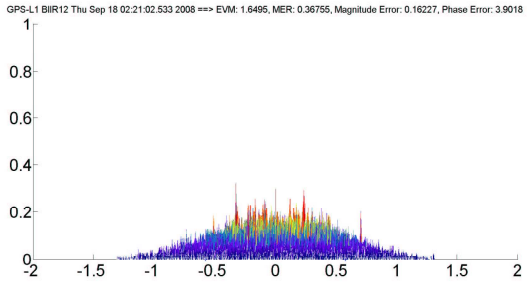

Figure 7.28: IQ diagram with Chebychef filter 5 MHz looking from quadrature side

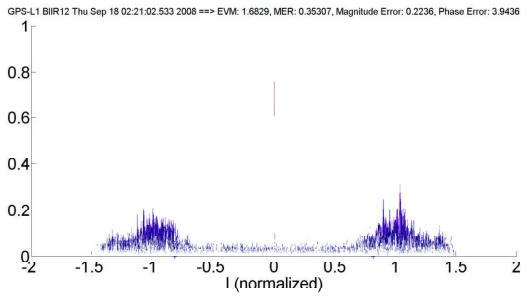

Figure 7.29: IQ diagram with Chebychef filter 2 MHz looking from in-phase side

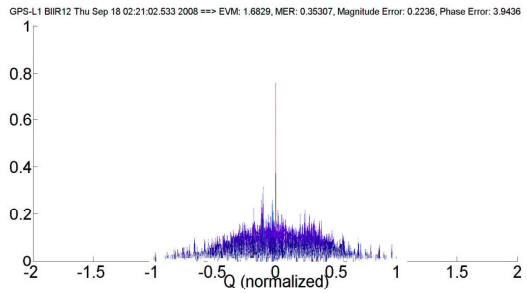

Figure 7.30: IQ diagram with Chebychef filter 2 MHz looking from quadrature side

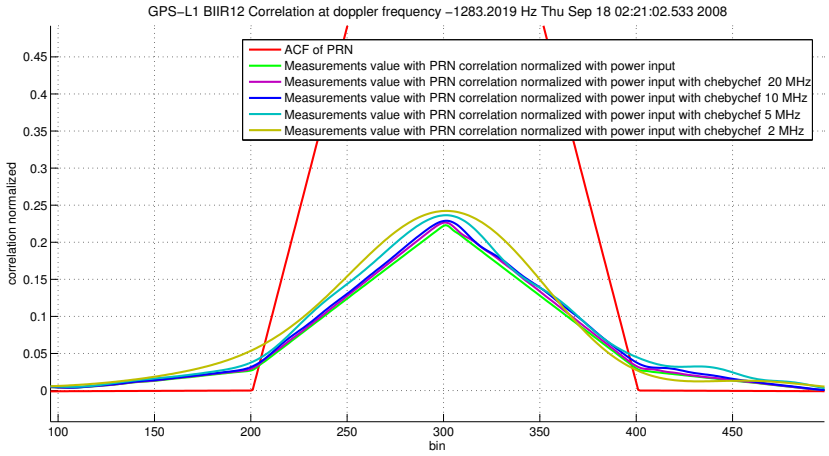

Figure 7.31: Correlation peak of the GPS BIIR12 L1 signal filtered with Chebychef

It can be seen from fig 7.31 that the correlation peak is deformed due to the filter. The peak is deformed in the late bin more than the early bin because the filters have memory and because the signals are time delayed after passing through the filter. With the smaller bandwidth such as 5 MHz and 2 MHz, the peak is rounder and has more normalized power. The reason for the increasing of the normalized power of the correlation peak to C/A code is that the power of C/A remains constant in contrast to the power of the wideband P(Y), which is more cut off by the narrower filter.

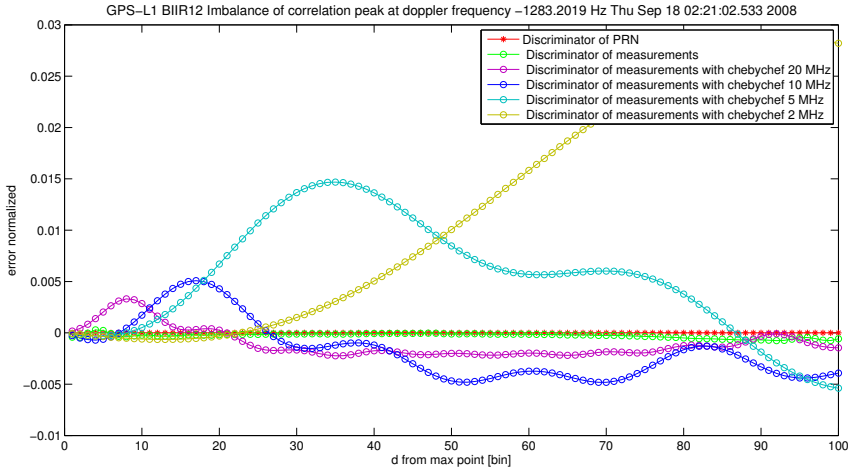

Figure 7.32: Imbalance of the correlation peak of the GPS BIIR12 L1 signal filtered with Chebychef

It can be seen from fig 7.32 that the peak of measurement without filtering is quite symmetry. With narrower bandwidth the difference of early and late bin increases , that means the correlation peak is more deformed.

Figures 7.33- 7.40 the early minus late power discriminator and their tracking error are shown. With the narrower bandwidth, the more the discriminator is deformed that cause the tracking error to increase. With the filter bandwidth of 5 MHz the tracking error reaches 8 meter, which is too bad for positioning.

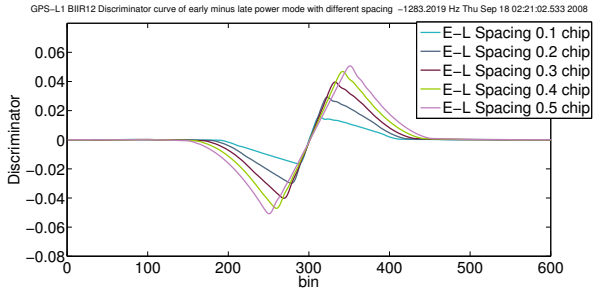

Figure 7.33: Early minus late power discriminator of the GPS BIIR12 L1 filtered with 20 MHz Chebychef

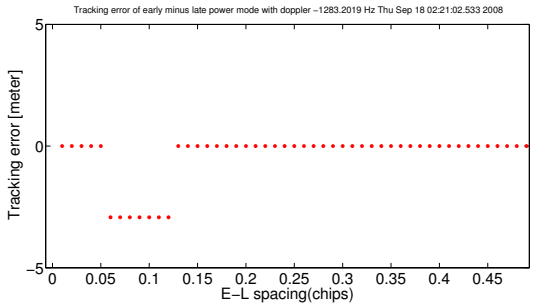

Figure 7.34: Tracking error of GPS BIIR12 L1 signal filtered with 20 MHz Chebychef

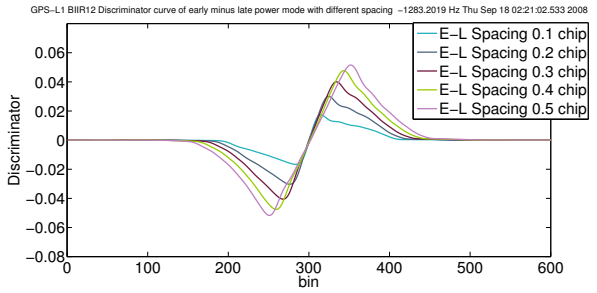

Figure 7.35: Early minus late power discriminator of the GPS BIIR12 L1 filtered with 10MHz Chebychef

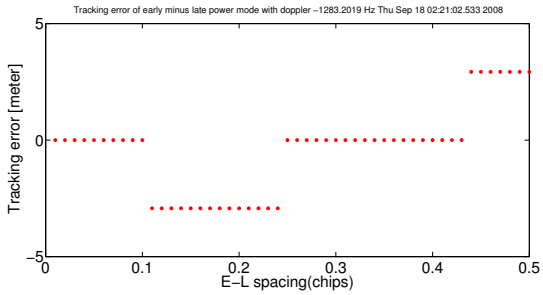

Figure 7.36: Tracking error of GPS BIIR12 L1 signal filtered with 10 MHz Chebychef

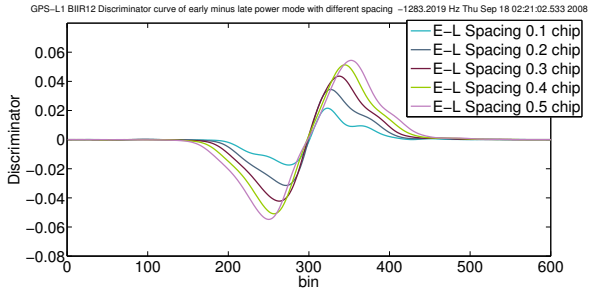

Figure 7.37: Early minus late power discriminator of the GPS BIIR12 L1 filtered with 5 MHz Chebychef

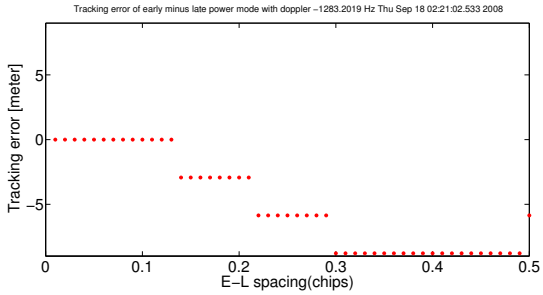

Figure 7.38: Tracking error of GPS BIIR12 L1 signal filtered with 5 MHz Chebychef

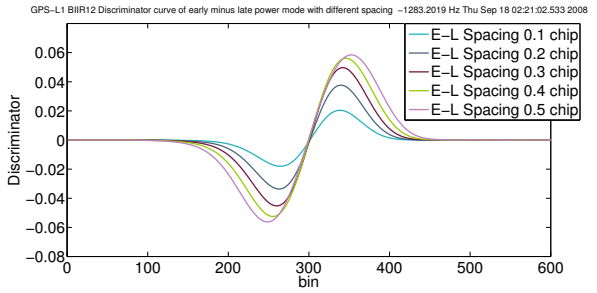

Figure 7.39: Early minus late power discriminator of the GPS BIIR12 L1 filtered with 2 MHz Chebychef

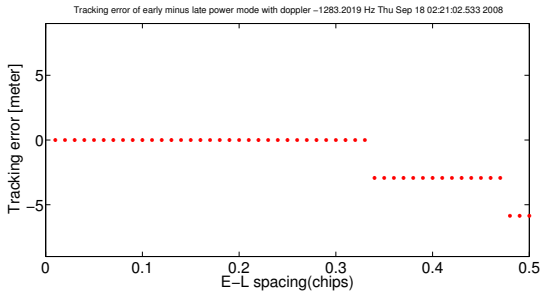

Figure 7.40: Tracking error of GPS BIIR12 L1 signal filtered with 2 MHz Chebychef

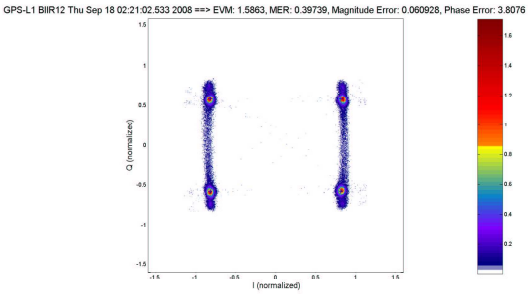

Figure 7.41: IQ diagram with 2 order Chebychef filter bandwidth 20 MHz

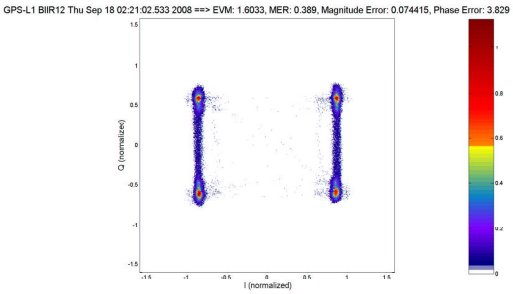

Figure 7.42: IQ diagram with 5 order Chebychef filter bandwidth 20 MHz

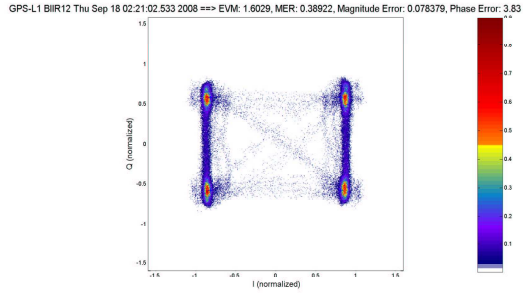

Figure 7.43: IQ diagram with 7 order Chebychef filter bandwidth 20 MHz

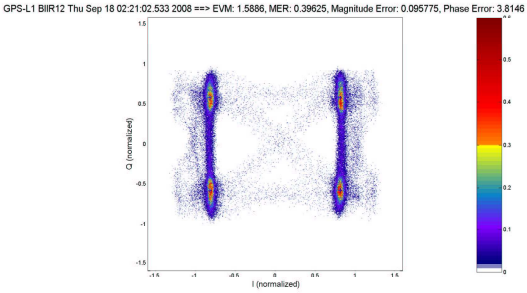

Figure 7.44: IQ diagram with 12 order Chebychef filter bandwidth 20 MHz

Figures 7.41- 7.44 compare the IQ diagram of different order of 20 MHz Chebychef filtering. The filter with 2nd order does not have steep bound, so some signal at the bound are still exist and the red points in the constellation are exactly at the ideal points. With increasing order of the filter, the IQ constellation is scattered from ideal points.

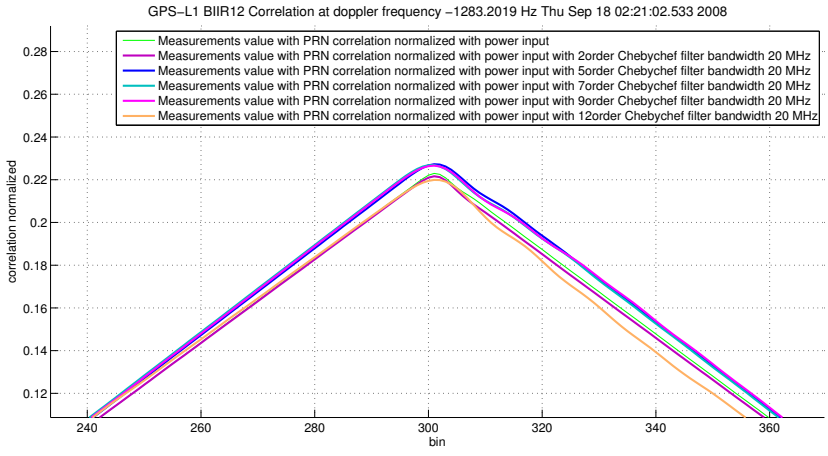

Figure 7.45: Comparing correlation peak with Chebychef filter bandwidth 20 MHz of different order

In figure 7.45 the correlation peaks with different order of 20 MHz Chebychef filtering are compared. The peaks of the filter with higher order are definitely deformed at the late bins.

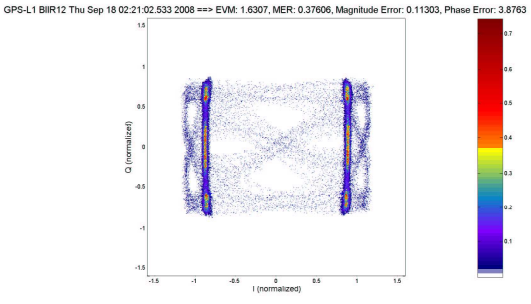

Figure 7.46: IQ diagram with 2 order Chebychef filter bandwidth 5 MHz

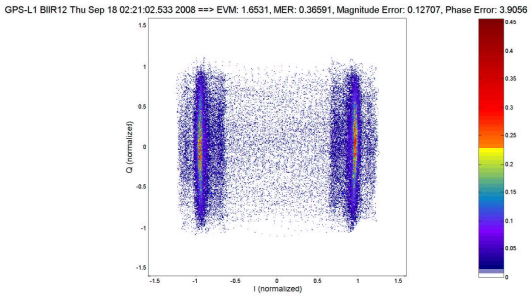

Figure 7.47: IQ diagram with 5 order Chebychef filter bandwidth 5 MHz

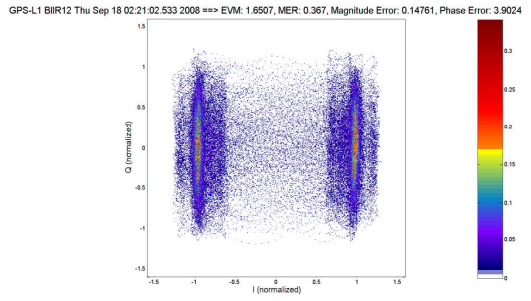

Figure 7.48: IQ diagram with 7 order Chebychef filter bandwidth 5 MHz

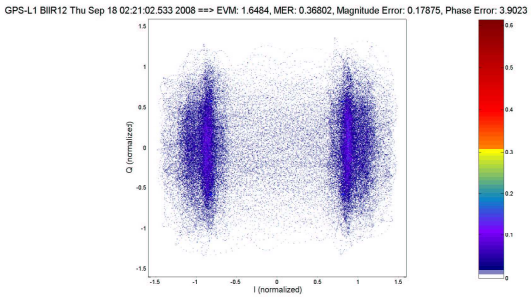

Figure 7.49: IQ diagram with 12 order Chebychef filter bandwidth 5 MHz

Figures 7.46- 7.49 compare the IQ diagram of different order of 5 MHz Chebychef filtering. The IQ constellation is more scattered from ideal points with the increasing order of the filter.

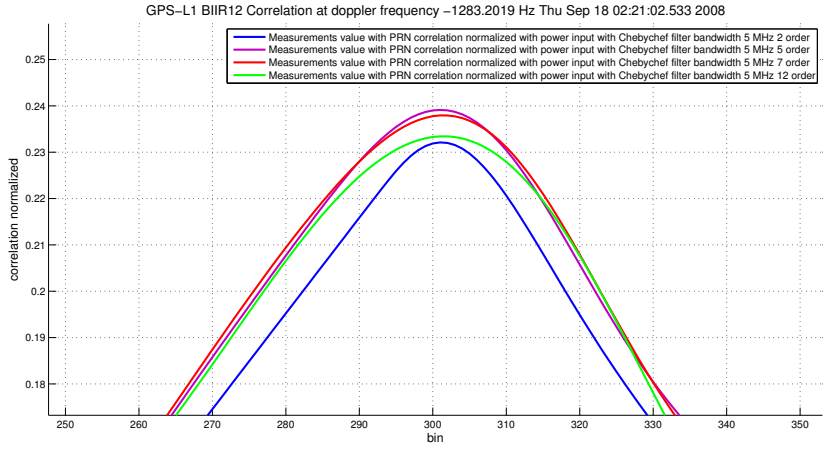

Figure 7.50: Comparing correlation peak with Chebychef filter bandwidth 5 MHz of different order

Figure 7.50 the correlation peaks with different order of 5 MHz Chebychef filtering are compared. The peak gets more rounder with the increasing order of the filter. The normalized powers of the peaks are increased, because the power of C/A remains in contrast to the power of the wideband P(Y), which is more cut off by the narrower filter of higher order.

7.2 GPS BIIR12 L1 with FIR Filtering

The next filter examined is FIR filter of order 61 with different cut-off frequency of 20, 10, 5 and 2 MHz. The phase delay and group delay of linear phase FIR filters are equal and constant over the frequency band. For an order n linear phase FIR filter, the group delay is n/2, and the filtered signal is delayed by n/2 time steps (and the magnitude of its Fourier transform is scaled by the filter's magnitude response). This property preserves the wave shape of signals in the passband; that is, there is no phase distortion [30]. The high order of filter is chosen to be exactly cut off the out-band frequency.

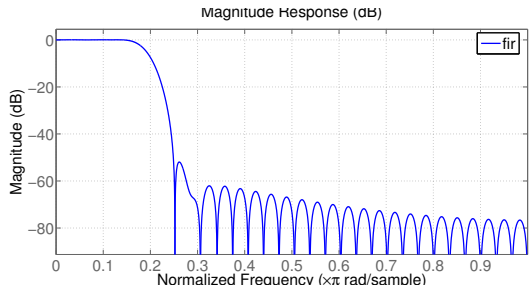

Figure 7.51: Magnitude response of the FIR order 61 with cut of frequency 20 MHz

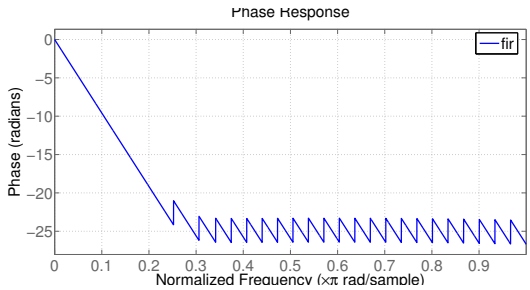

Figure 7.52: Phase response of the FIR order 61 with cut of frequency 20 MHz

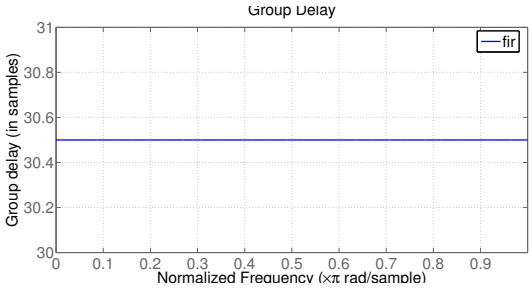

Figure 7.53: Group delay of the FIR order 61 with cut of frequency 20 MHz

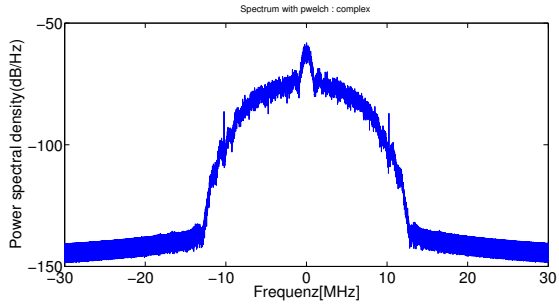

Figure 7.54: Power Spectrum of IQ data filtered with 61th order FIR filter with cut of frequency 20 MHz

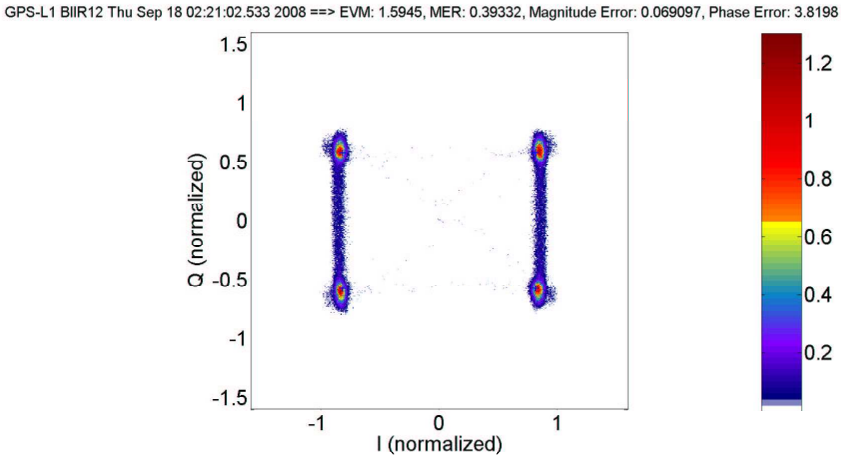

Figure 7.55: IQ constellation of GPS BIIR12 L1 signal filtered with 20 MHz FIR normalized with maximum value before filtering

With 20 MHz filter the main lobes of the P(Y) and C/A code still can be seen. The constellation is deformed by the filter; however the ideal constellation points are still able to be recognized. The

transitions between the points are intensified, since the signals are not exactly at the ideal points. The error vector magnitude increases accordingly.

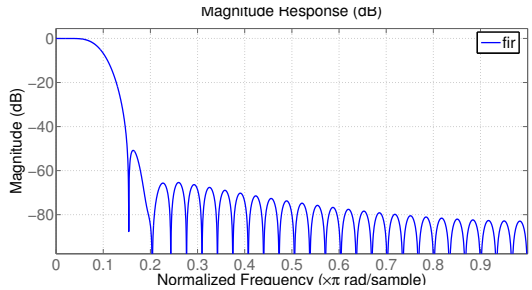

Figure 7.56: Magnitude response of the 61th order FIR filter with cut of frequency 10 MHz

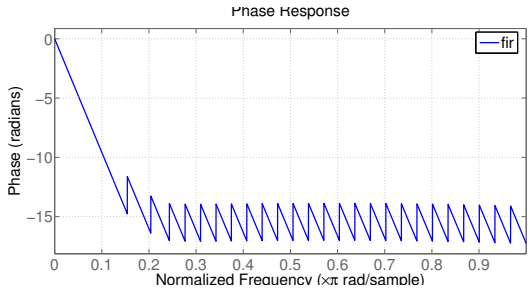

Figure 7.57: Phase response of the 61th order FIR filter with cut of frequency 10 MHz

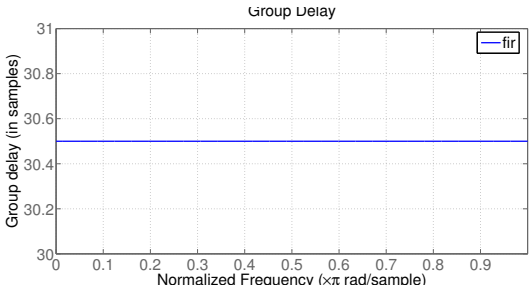

Figure 7.58: Group delay of the 61th order FIR filter with cut of frequency 10 MHz

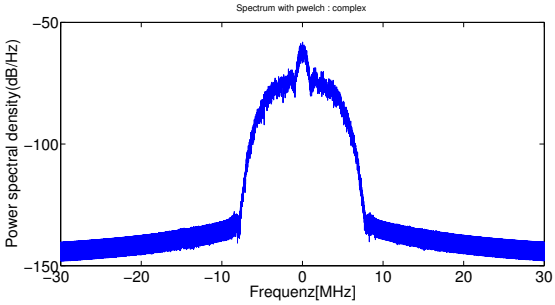

Figure 7.59: Power Spectrum of IQ data filtered with 61th order Filter filter with cut of frequency 10 MHz

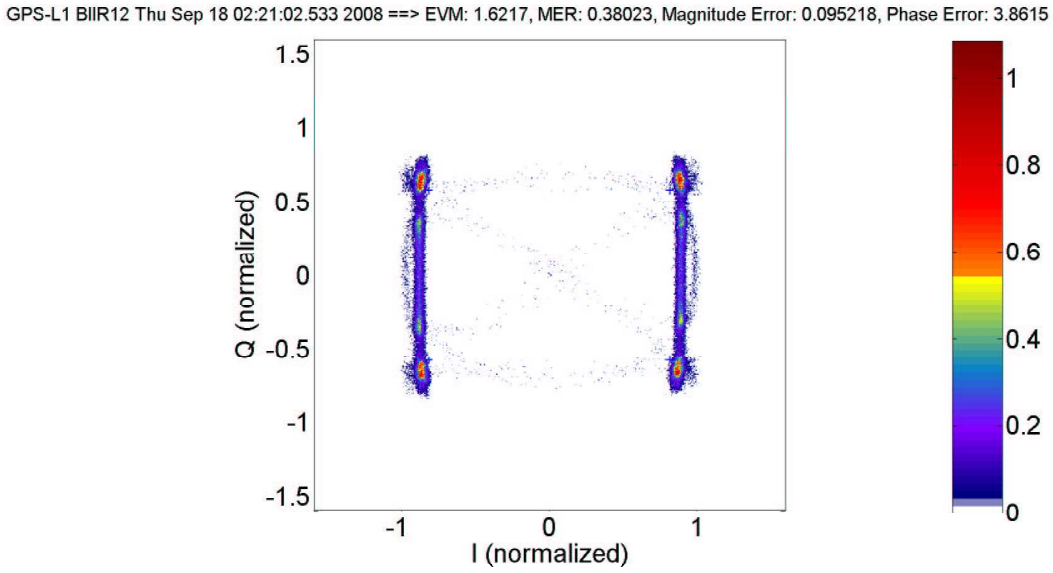

Figure 7.60: IQ constellation of GPS BIIR12 L1 signal filtered with 10 MHz FIR normalized with maximum value before filtering

With 10 MHz filter the main lobes of the P(Y) and C/A code can be seen. The constellation is deformed by the filter that the recognized points move away from the ideal points. The transitions seem to be still moving to and from the correct constellation. The error vector magnitude increases accordingly.

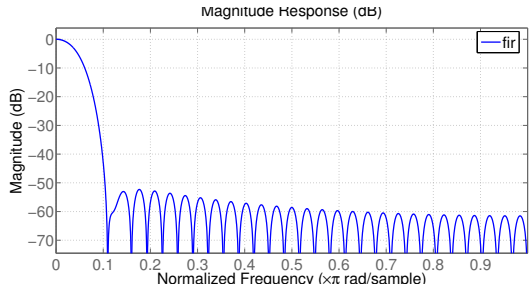

Figure 7.61: Magnitude response of the 61th order FIR filter with cut of frequency 5 MHz

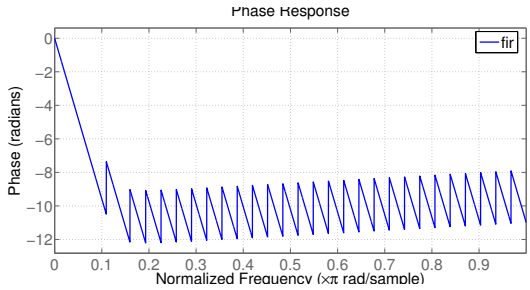

Figure 7.62: Phase response of the 61th order FIR filter with cut of frequency 5 MHz

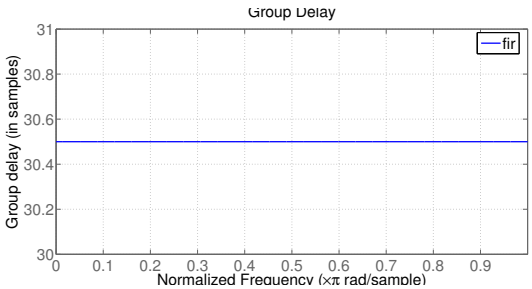

Figure 7.63: Group delay of the 61th order FIR filter with cut of frequency 5 MHz

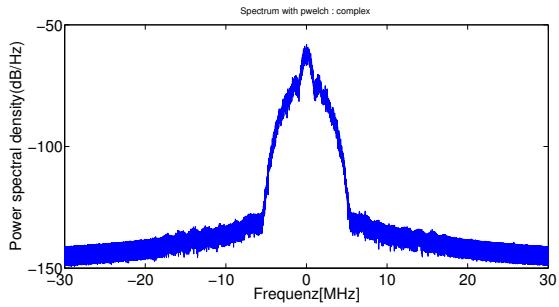

Figure 7.64: Power Spectrum of IQ data filtered with 61th order Filter filter with cut of frequency 5 MHz

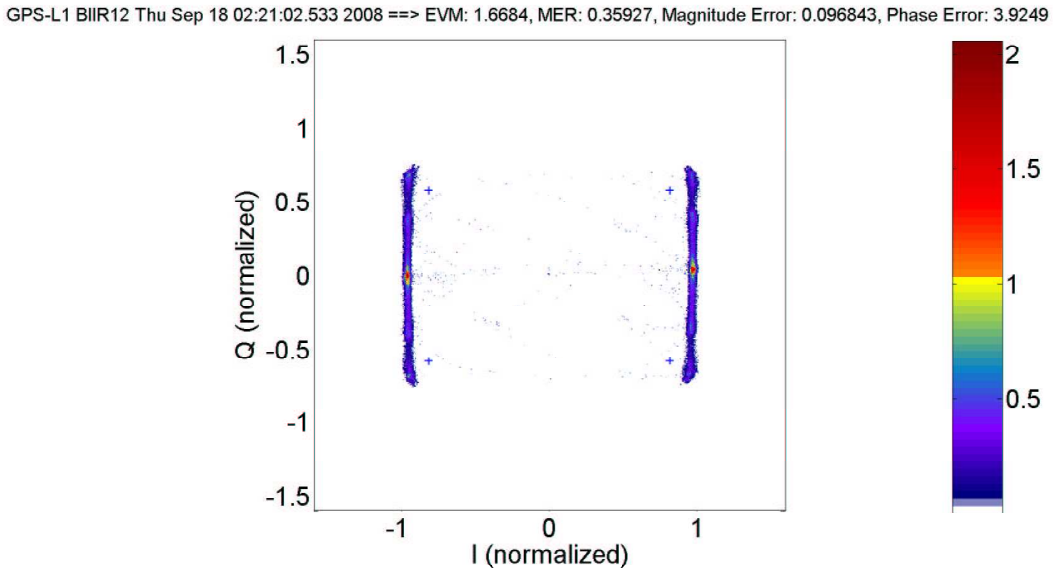

Figure 7.65: IQ constellation of GPS BIIR12 L1 signal filtered with 5MHz FIR normalized with maximum value before filtering

With 5 MHz filter the main lobes of the P(Y) and C/A code can be seen. The constellation looks like two thin lines with maximum point in the middle of each line. These two lines are clearly extended outward from the original point. The error vector magnitude increases accordingly.

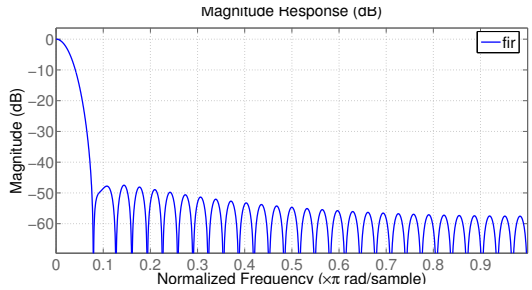

Figure 7.66: Magnitude response of the 61th order FIR filter with cut of frequency 2 MHz

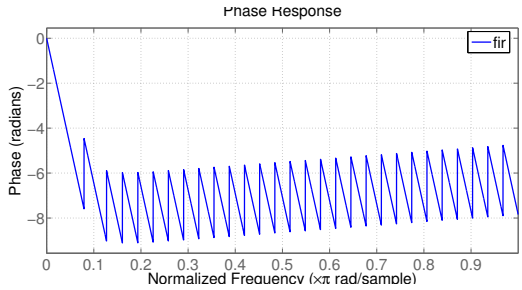

Figure 7.67: Phase response of the 61th order FIR filter with cut of frequency 2 MHz

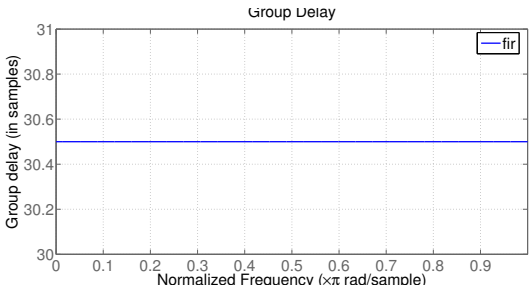

Figure 7.68: Group delay of the 61th order FIR filter with cut of frequency 2 MHz

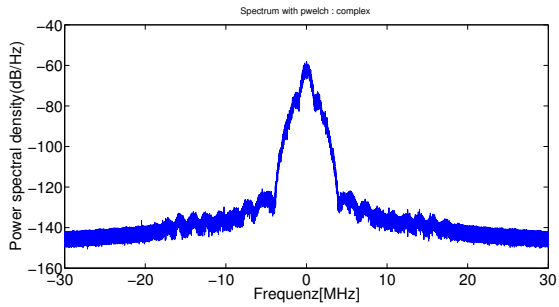

Figure 7.69: Power Spectrum of IQ data filtered with 61th order FIR filter with cut of frequency 2 MHz

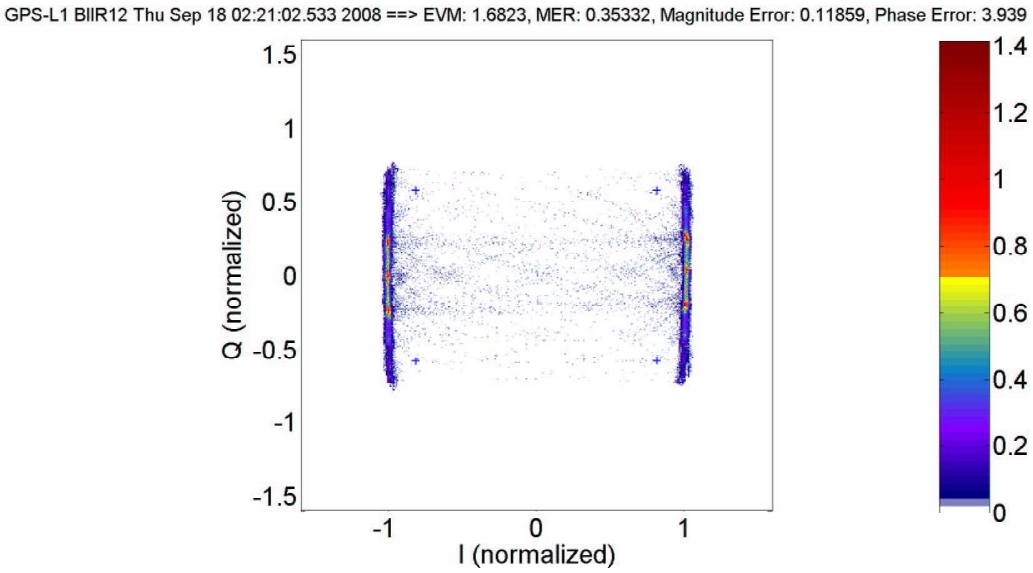

Figure 7.70: IQ constellation of GPS BIIR12 L1 signal filtered with 2MHz FIR normalized with maximal value before filtering

With 2 MHz filter the main lobes of the P(Y) and C/A code still can be seen. The constellation is distorted by the filter, that the ideal points cannot be recognized. The transition in quadrature phase looks like two lines, 3 red points in the middle of each line can be seen.

It could be seen that the cut-off frequency of the FIR filter is not as steep as with the Chebychef filter, that the P(Y) code still exist with the narrower bandwidth and the transition in the quadrature axis are to be recognized.

Figures 7.71- 7.78 show the IQ diagram from side view to investigate the distribution of the signal of each filter bandwidth. With narrower filter bandwidth the in-phase constellation are moved outward from the original point but can still be recognized. The transition in the quadrature phase

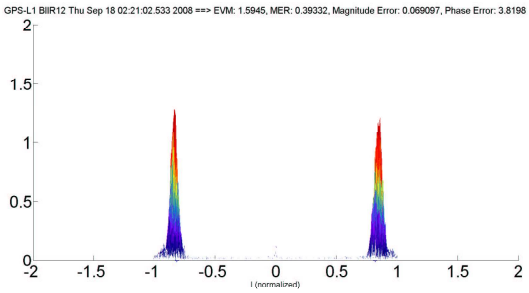

Figure 7.71: IQ diagram with FIR filter 20 MHz looking from in-phase side

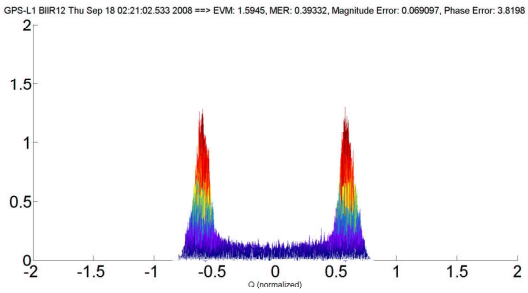

Figure 7.72: IQ diagram with FIR filter 20 MHz looking from quadrature side

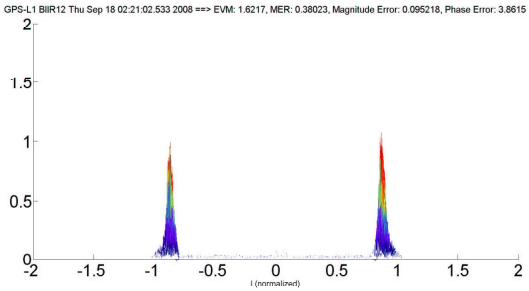

Figure 7.73: IQ diagram with FIR filter 10 MHz looking from in-phase side

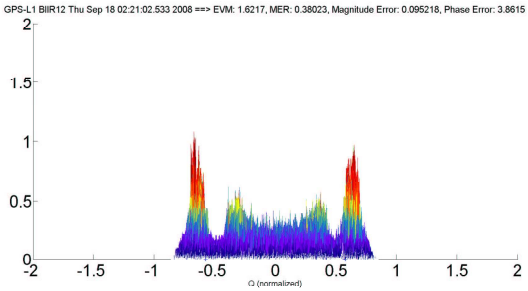

Figure 7.74: IQ diagram with FIR filter 10 MHz looking from quadrature side

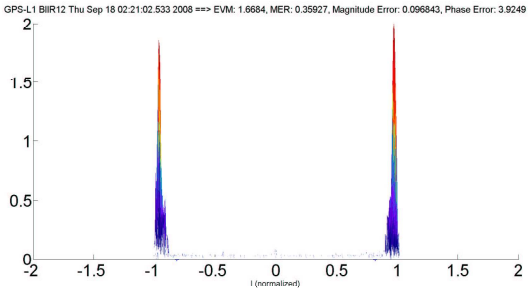

Figure 7.75: IQ diagram with FIR filter 5 MHz looking from in-phase side

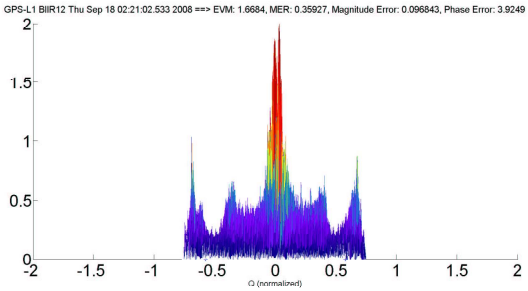

Figure 7.76: IQ diagram with FIR filter 5 MHz looking from quadrature side

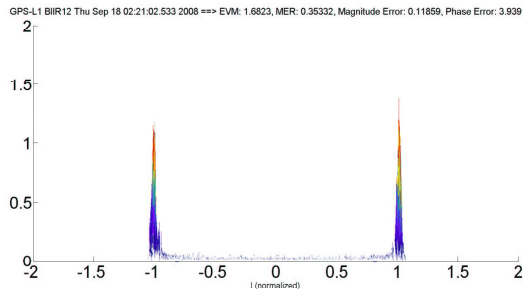

Figure 7.77: IQ diagram with FIR filter 2 MHz looking from in-phase side

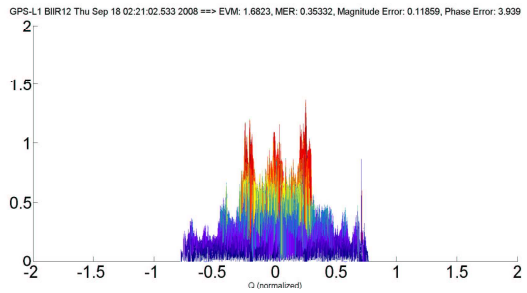

Figure 7.78: IQ diagram with FIR filter 2 MHz looking from quadrature side

concentrates more in the middle of the transition with the filter bandwidth of 5 MHz, which make it unable recognize the points.

The IQ constellations are not strongly scattered after passing through the FIR filter in contrast to the Chebychef filter. The normalized power of the IQ constellation after FIR filtering is increased in contrast to the Chebychef filter. This could be due to the linear phase of the FIR filter.

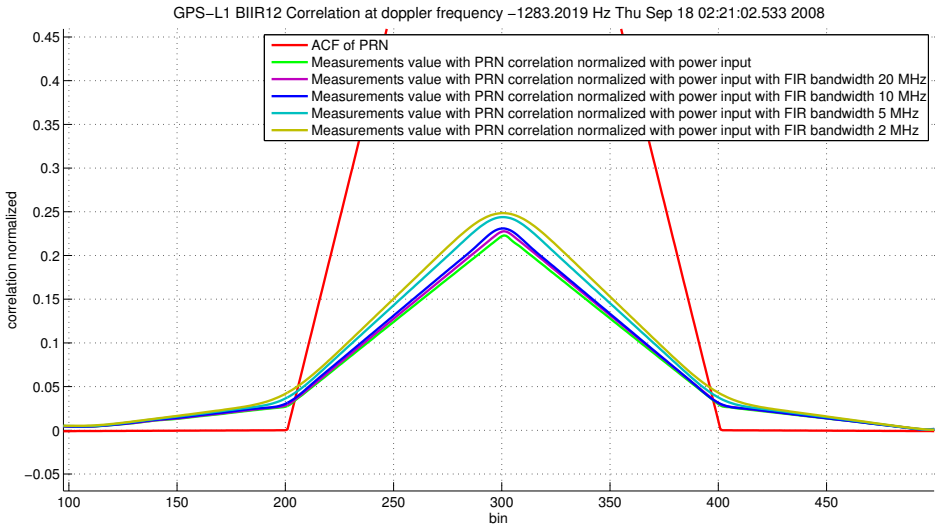

Figure 7.79: Correlation peak of the GPS BIIR12 L1 signal filtered with FIR

The correlation peaks are deformed. With the narrower bandwidth, the peak would become rounder and higher due to the same factor as explained for Chebychef filter. However the peak still looks symmetric in contrast to the peak with Chebychef filter, because the FIR filter has linear phase response that does not distorted the signal.

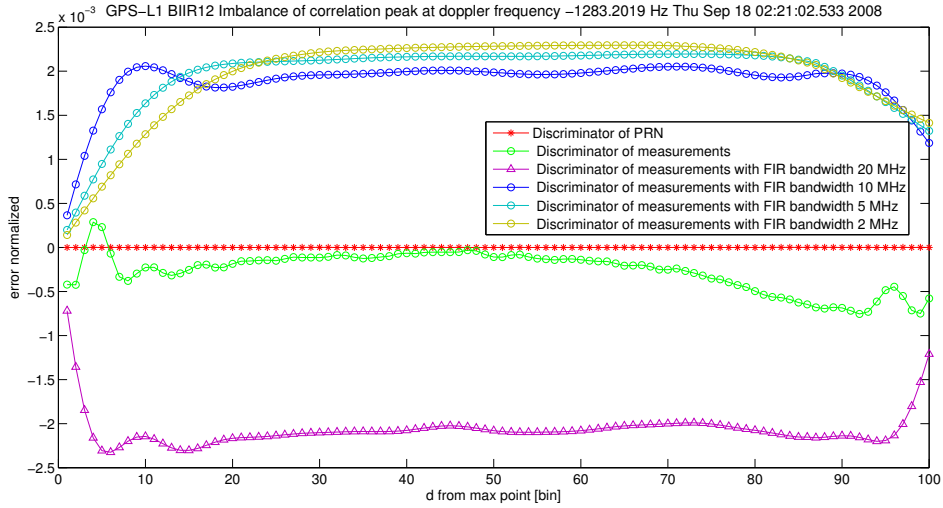

Figure 7.80: Imbalance of the correlation peak of the GPS BIIR12 L1 signal filtered with FIR

From figure 7.80 it can be said that without filter the imbalance of the peak keeps close to the ideal PRN curve, but when the filter is used, the imbalance increases.

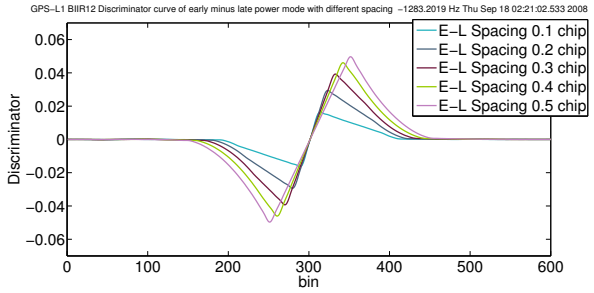

Figure 7.81: Early minus late power discriminator of GPS BIIR12 L1 signal filtered with 20 MHz FIR

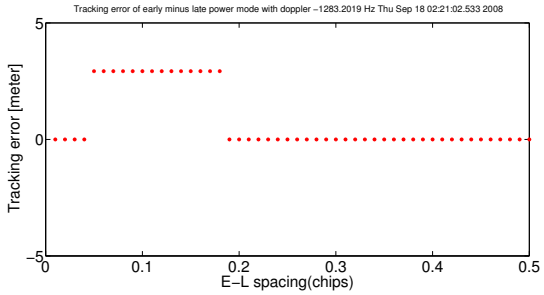

Figure 7.82: Lock point bias of early minus late power discriminator of BIIR12 L1 signal with 20 MHz FIR

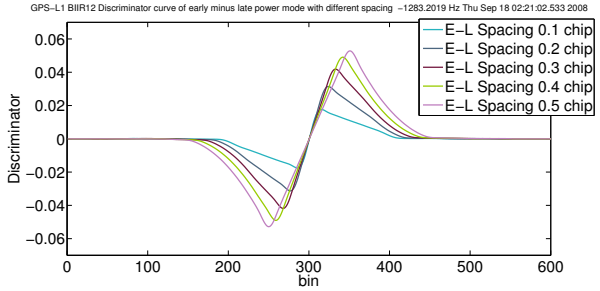

Figure 7.83: Early minus late power discriminator of GPS BIIR12 L1 signal filtered with 10 MHz FIR

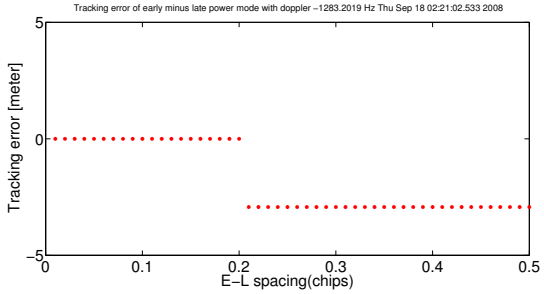

Figure 7.84: Lock point bias of early minus late power discriminator of BIIR12 L1 signal with 10 MHz FIR

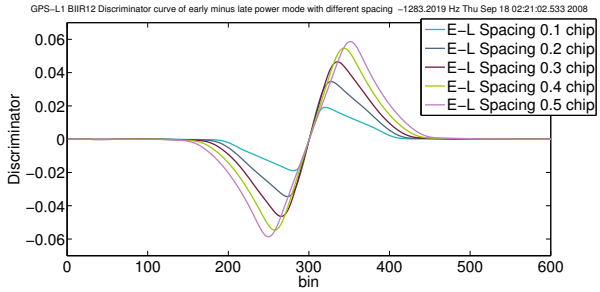

Figure 7.85: Early minus late power discriminator of GPS BIIR12 L1 signal filtered with 5 MHz FIR

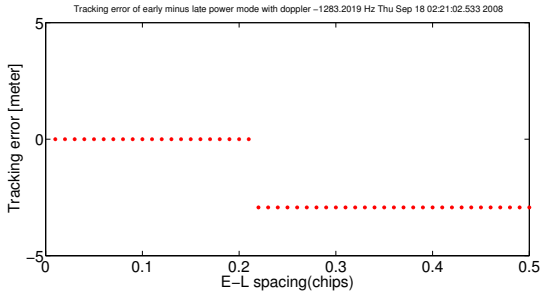

Figure 7.86: Lock point bias of early minus late power discriminator of BIIR12 L1 signal with 5 MHz FIR

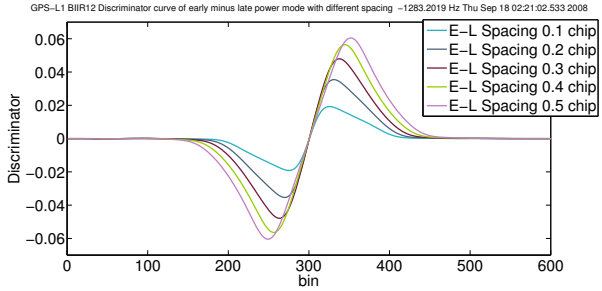

Figure 7.87: Early minus late power discriminator of GPS BIIR12 L1 signal filtered with 2 MHz FIR

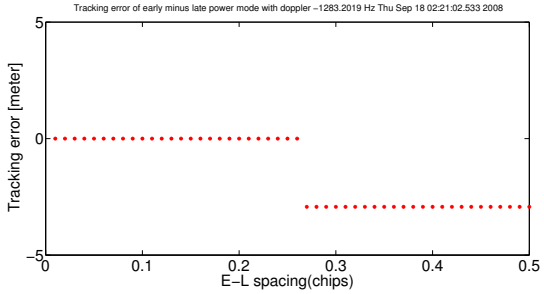

Figure 7.88: Lock point bias of early minus late power discriminator of BIIR12 L1 signal with 2 MHz FIR

Figures 7.81- 7.88 the early minus late power discriminator and their tracking error are shown. With narrower bandwidth, the more the discriminator is deformed. But the maximum tracking error keeps on about 3 meters in contrast to Chebychef filtering that causes the tracking error to increase to about 8 meters.

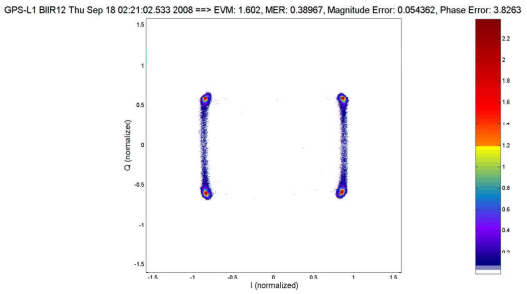

Figure 7.89: IQ diagram with 10 order FIR filter bandwidth 20 MHz

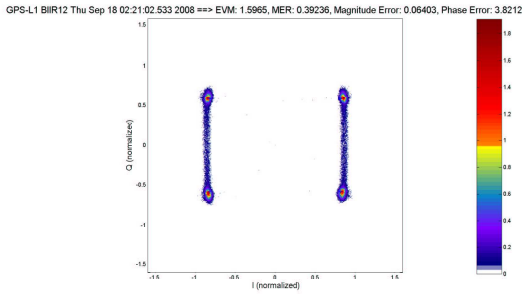

Figure 7.90: IQ diagram with 30 order FIR filter bandwidth 20 MHz

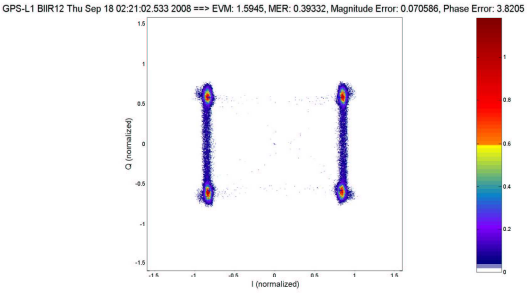

Figure 7.91: IQ diagram with 80 order FIR filter bandwidth 20 MHz

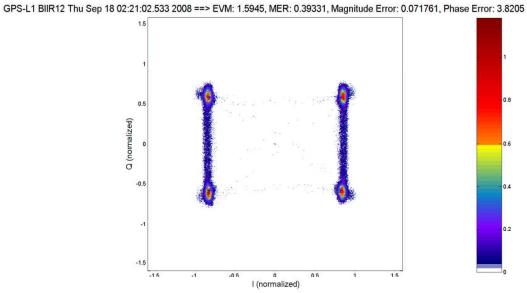

Figure 7.92: IQ diagram with 101 order FIR filter bandwidth 20 MHz

Figures 7.89 - 7.92 compare the IQ diagram of different order of 20 MHz FIR filtering. With increasing order of the filter, the IQ constellation is more scattered from ideal points.

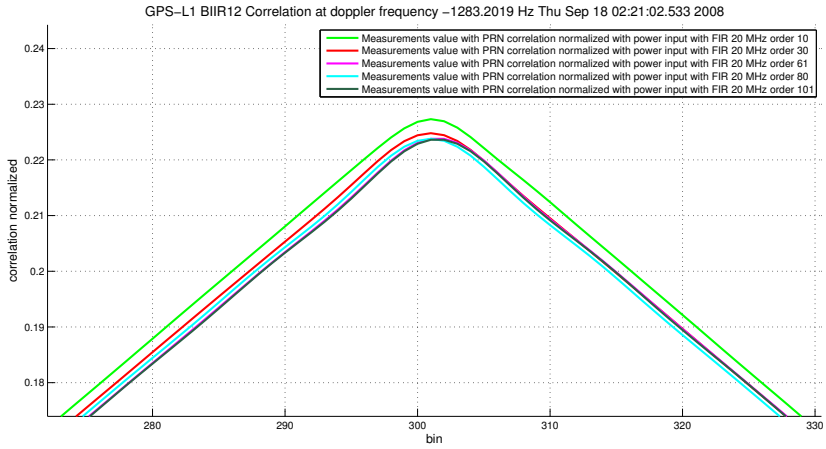

Figure 7.93: Comparing correlation peak with FIR filter bandwidth 20 MHz of different order

Figure 7.93 the correlation peaks with different order of 20 MHz FIR filtering are compared. The normalized power of the peak decreases with the increasing order of the FIR filter, which does not comply with the normal case. The normal case signifies that the more frequency has been cut (due to the narrower bandwidth or the higher order of the filter), the more the normalized power is produced. However the decreasing power of the peak is up to 0.0037, which is only a small amount.

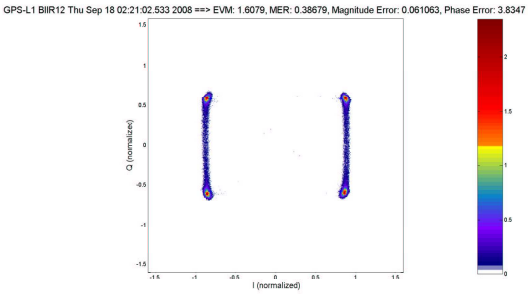

Figure 7.94: IQ diagram with 10 order FIR filter bandwidth 2 MHz

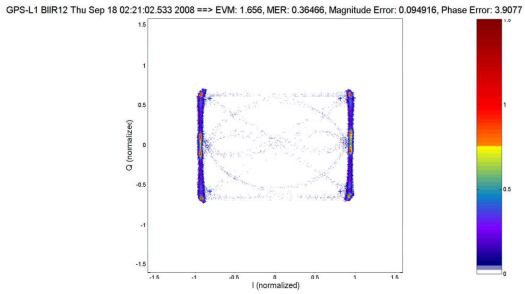

Figure 7.95: IQ diagram with 30 order FIR filter bandwidth 2 MHz

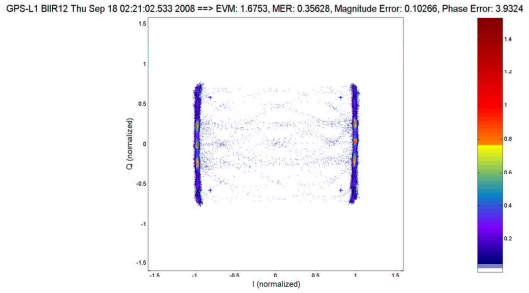

Figure 7.96: IQ diagram with 80 order FIR filter bandwidth 2 MHz

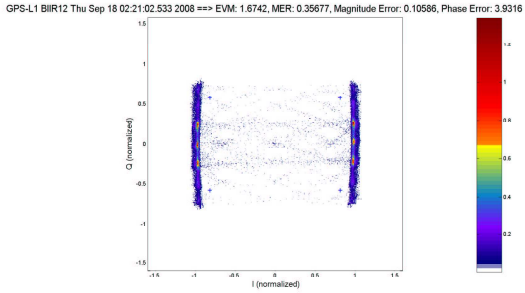

Figure 7.97: IQ diagram with 101 order FIR filter bandwidth 2 MHz

Figures 7.94- 7.97 compare the IQ diagram of different order of 2 MHz FIR filtering. The points in the IQ constellation with FIR order 10 can still be recognized, because the cut off bound is not steep and mostly power of P(Y) is retained. With more order of the FIR filter, the points with maximum possibility concentrate more in the middle of each quadrature transition.

The difference between the linear phase filter and the non-linear phase filter is that the linear phase filter has just cut the out of bound frequency but does not distort the signal. Therefore the transitions in the quadrature phase only look thinner but do not scatter like the non-linear phase filter.

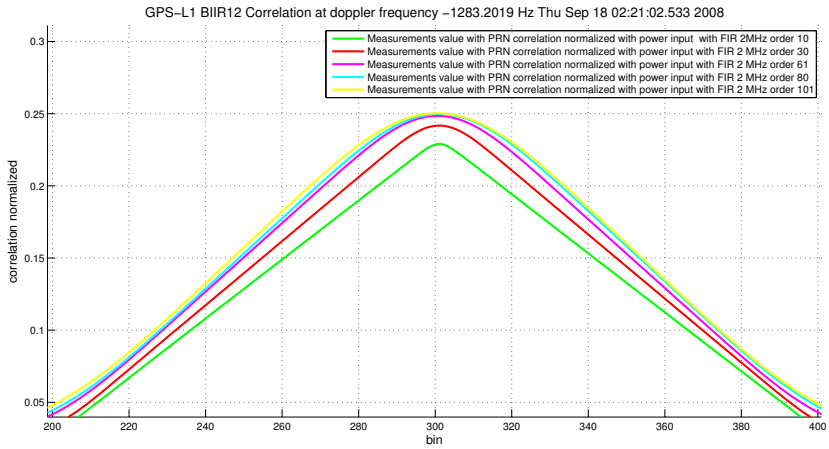

Figure 7.98: Comparing correlation peak with FIR filter bandwidth 2 MHz of different order

Figure 7.98 the correlation peaks with different order of 2 MHz FIR filtering are compared. The peaks are rounder and the normalized power increases with the increasing order of the FIR filter. This complies with results of previous experiments which indicate: the more frequency has been cut (due to the narrower bandwidth or the higher order of the filter), the more the normalized power is produced.

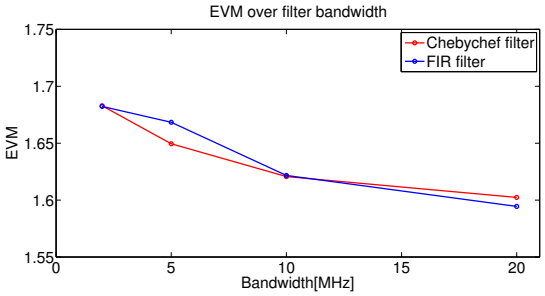

Figure 7.99: EVM over filter bandwidth

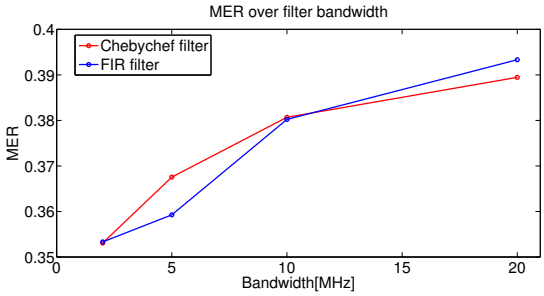

Figure 7.100: MER over filter bandwidth

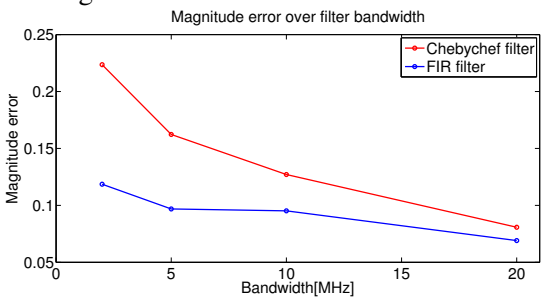

Figure 7.101: Magnitude error over filter bandwidth

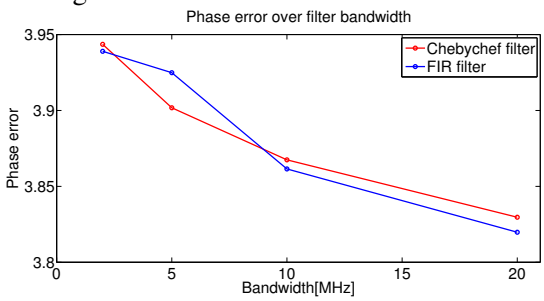

Figure 7.102: Phase error over filter bandwidth

In figure 7.99 - 7.102 the error vector magnitude and related quantities are plotted over the filter bandwidth. The EVM, magnitude error and phase error decrease as the bandwidth increases in contrast to the MER, which measures the signal to noise ratio. The magnitude error of the Chebychef filter is absolutely higher than the magnitude error of the FIR filter. Whereas the value differences of the other units are marginal.

8. Signal Deformation Analysis

8.1 Non-Linear Power Amplification

Power amplifiers are described by their AM/AM which is the amplitude amplification and AM/PM which is the the phase distortion depending on the amplitude. The model used here is from Saleh [29], which is a simple two-parameter formulas. The input is the amplitude of the signal A and the output are

$$\gamma(A) = \frac{\alpha_a A}{1 + \beta_a A^2} \tag{8.1}$$

$$\Delta\phi(A) = \frac{\alpha_\phi A^2}{1 + \beta_\phi A^2} \tag{8.2}$$

whereas α_a, β_a, α_ϕ, β_ϕ are parameter specific for a given amplifier.

According to [28] for a large input back off, the operation of the amplifier below its saturation point limits the AM/AM distortion. The AM/PM term becomes dominant. The model is further simplified that $\beta_a = \beta_\phi = 0$ then

$$\Delta\phi(A) = \alpha_\phi A^2 \tag{8.3}$$

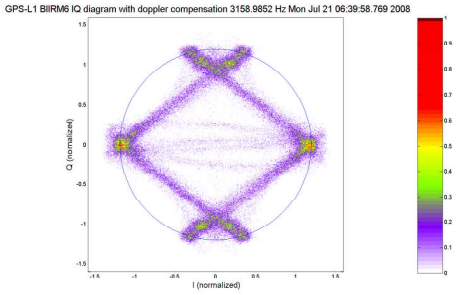

Figure 8.1: The IQ diagram before AM/PM

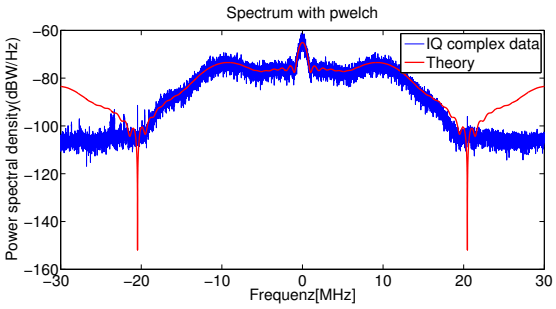

Figure 8.2: Power spectrum density before AM/PM

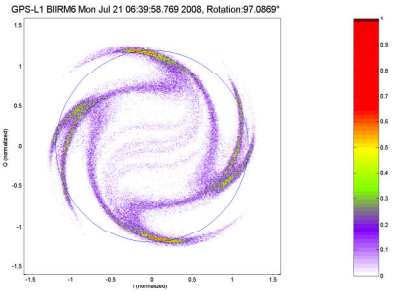

Figure 8.3: The IQ diagram after AM/PM

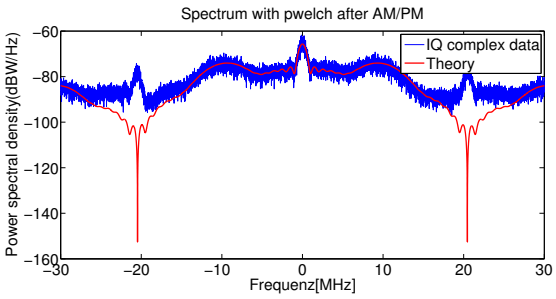

Figure 8.4: The power spectrum density after AM/PM

The variable α_ϕ is set to 1.2. The distorted IQ constellation is generated. From figure 8.3 it can be seen that the large amplitudes are significantly rotated and deformed. The constellation is rotated with 97.0869° from the ideal constellation.

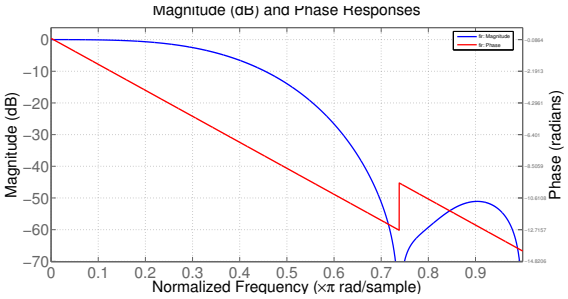

Figure 8.5: The magnitude and phase response of 20MHz lowpass FIR filter order 11

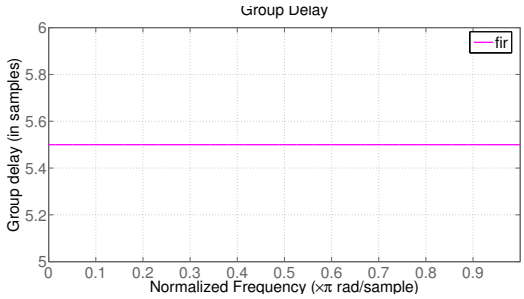

Figure 8.6: The group delay of 20MHz lowpass FIR filter order 11

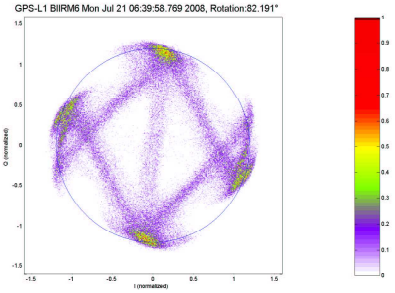

Figure 8.7: The IQ diagram after AM/PM and FIR filtering

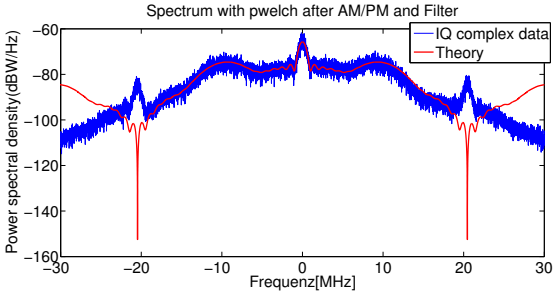

Figure 8.8: The power spectrum density after AM/PM and FIR filtering

The figure 8.4 shows the power spectral density of the by AM/PM distorted signal. As seen, the power is amplified and some power outside the bandwidth boundary increases. The difference of the out of band power to the power at center frequency decreases to be less than 30 dB from figure 8.2. This could be the bandwidth expansion as described in [28], in which the power out of the band is pumped. The spectrum after AM/PM does not show asymmetries; therefore AM/PM has no effect to the asymmetry of the signal.

As suggested in [28] the distortion due to the AM/PM could be compensated by the post-filtering. Here the FIR lowpass filter of order 11 with 20 MHz bandwidth is used to filter the signal with AM/PM amplification. The IQ constellation as seen in figure 8.7 does not show S-shape like before but the constellation is still slant and scattered, with the rotation of 82.191°.

In figure 8.8 the spectral power density after filtering is shown. The out-of-band power, which is due to AM/PM characteristics, is decreased. The power spectrum does not show asymmetry, because the symmetry filter is used.

Figure 8.9 shows a spectral measurement of BIIRM1 L1 signal recorded at 12:11:54 UTC on 21 July 2008. The deformation of the spectral power density around 1560 and 1591 MHz can be seen. This deformation looks similar to the investigated spectrum after AM/PM and filtering, therefore this deformation can be caused by the AM/PM distortion.

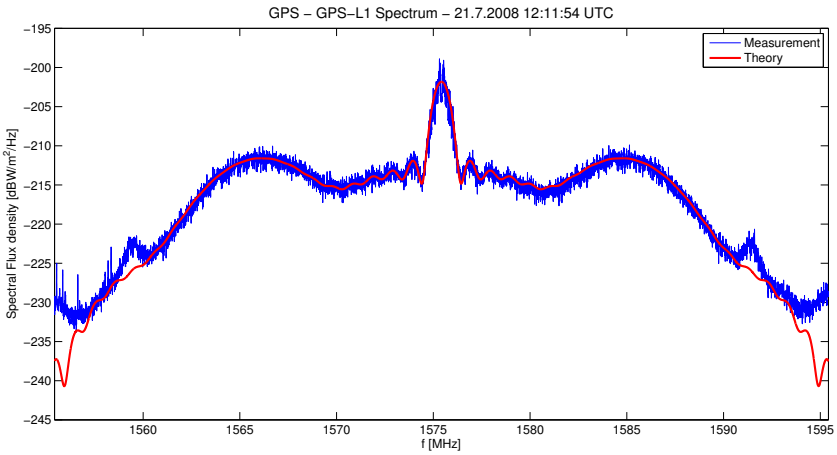

Figure 8.9: Measured spectral of GPS BIIRM1 L1 signal

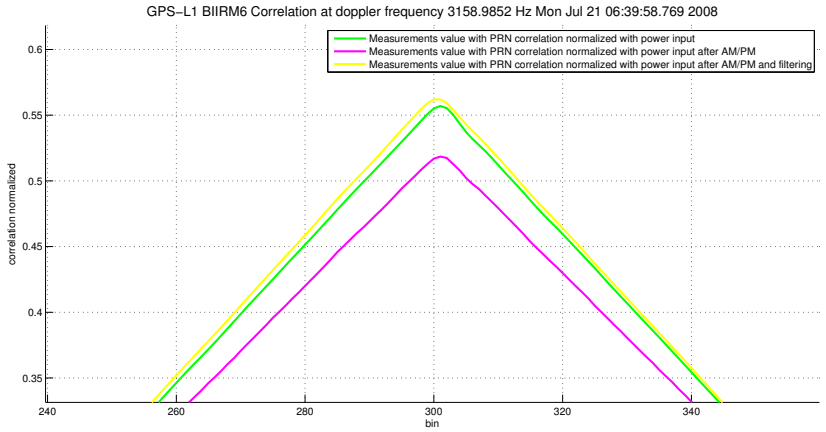

Figure 8.10: Compare correlation peak

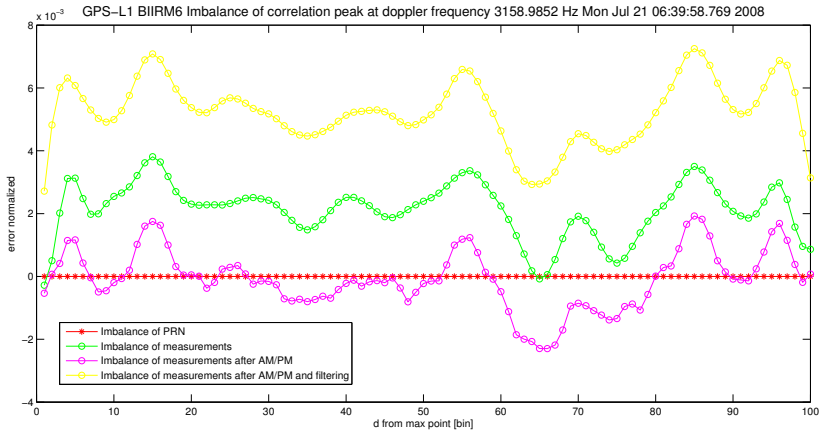

Figure 8.11: Compare imbalance of correlation peak

In figure 8.10 the correlation peak after AM/PM distortion lies under the original correlation, but after AM/PM and filtering the correlation has a little bit more power than the original correlation. This could be due to the filter effect as discussed in chapter 7.

In figure 8.11 the imbalance of the peak has mostly the same distribution. But there are some differences caused by the variation of the power after amplification. This is obviously the case because the correlation peak is not deformed.

It can be concluded that the AM/PM affects the IQ phase constellation and power spectral density at some frequency, however it does not cause spectral asymmetries and correlation peak distortion.

8.2 Dispersive Behavior of the Front-End

The dispersive behavior of the transmitter front end can be modeled by a finite-response filter [28]. A Wiener filter is obtained if the quadratic distance between the signal generated by the filter and the received signal is minimized.

$$\Delta = \sum_{n=1}^{N} |r_n - (\hat{h} * s)_n|^2 \tag{8.4}$$

The length of filter N is chosen to be finite and here is chosen to be 14 like in [28]. The solution of the Wiener filtering problem is

$$h = (A^H A)^{-1} A^H C \tag{8.5}$$

with $.^H$ denoting the Hermitian conjugate and with A and C being the following autocorrelation matrix and cross correlation vector as

$$A_{km} = \sum_n s_{n-m} s^*_{n-k} \tag{8.6}$$

$$C_k = \sum_n r_n s^*_{n-k} \tag{8.7}$$

The frequency response denoted

$$\begin{aligned} H(f) &= |H(f)| e^{j\Phi(f)} \\ &= \sum_{n=0}^{N-1} h_n e^{j2\pi n\delta} \end{aligned} \tag{8.8}$$

whereas $|H(f)|$ is the amplitude and $\Phi(f) = arg(H(f))$ is the phase response of the filter. The group delay is $\tau = -d\Phi(f)/df$. The asymmetry in the amplitude leads to a corresponding asymmetry in the spectrum, which will be seen later in the experiments.

At first the dispersive behavior of the signal from BIIR12 L1 signal is examined. In figure 8.12 the spectral power density shows symmetry. The magnitude response of the front-end dispersive behavior solved with Wiener solution in figure 8.13 is therefore symmetric. The group delay is not constant; however the tendency continues to be near zero.

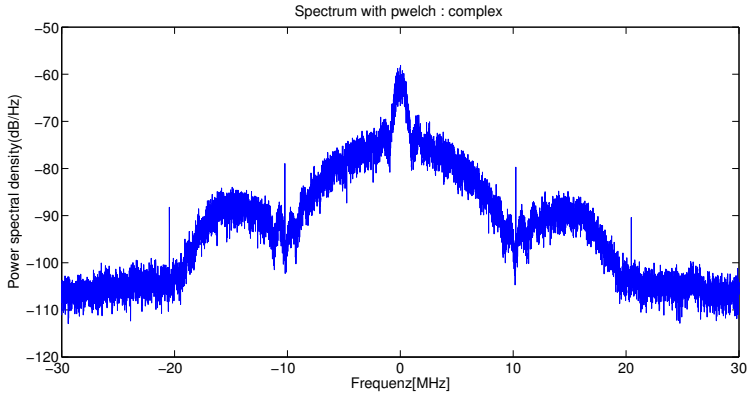

Figure 8.12: Symmetric power spectral density of BIIR12 L1 signal

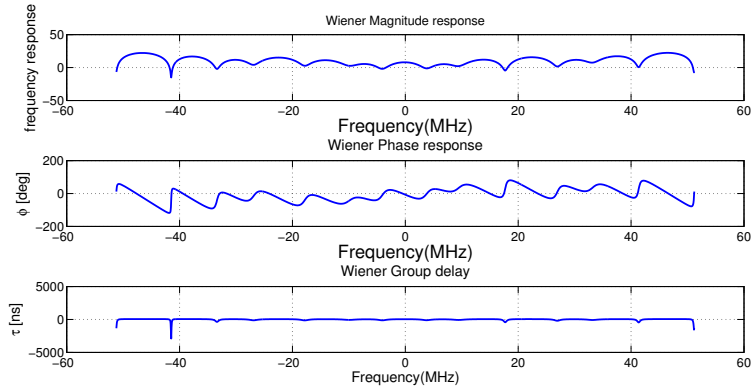

Figure 8.13: Dispersive behavior of the front-end BIIR12 L1

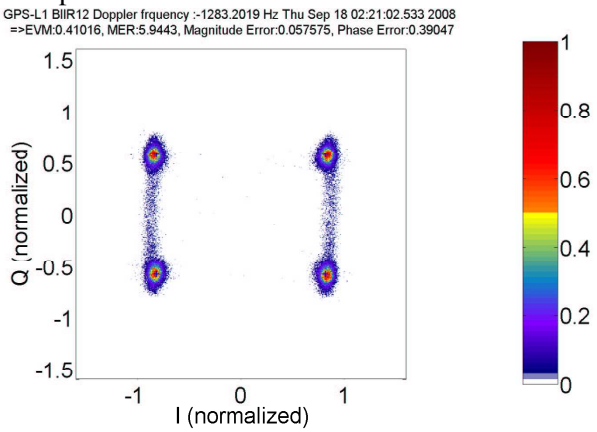

Figure 8.14: IQ Constellation of GPS BIIR12 L1 signal

After that the signal with asymmetric spectrum is examined. The signal is from BIIR12 L2 band as shown in figure 8.15- 8.18. The power spectrum generated from IQ data with pwelch function in figure 8.15 has more power in the left side lobe than in the right side lobe. The magnitude response of the front-end dispersive behavior solved with Wiener solution is asymmetric accordingly. The IQ constellation of the signal shown in figure 8.17 has very wide eye opening in the middle due to the phase distortion that causes the mixing of the in-phase and quadrature components.

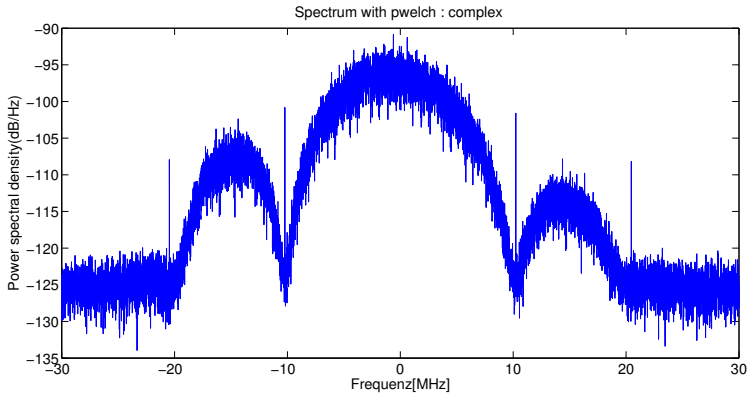

Figure 8.15: Asymmetric power spectral density of BIIR12 L2 signal

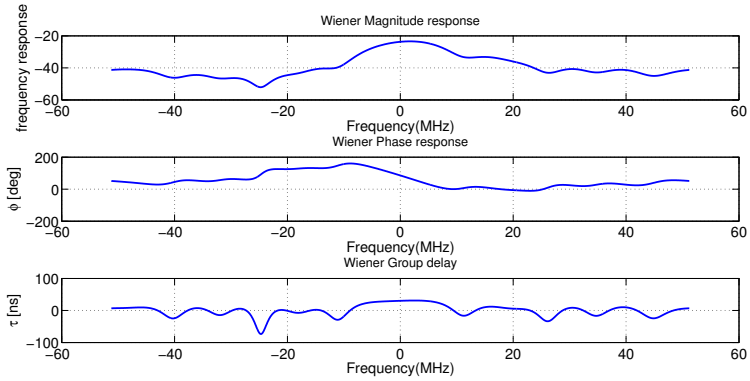

Figure 8.16: Dispersive behavior of the front end BIIR12 L2

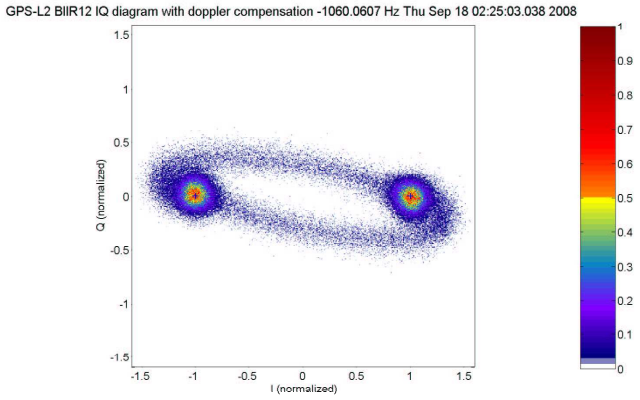

Figure 8.17: The IQ constellation of BIIR12 L2

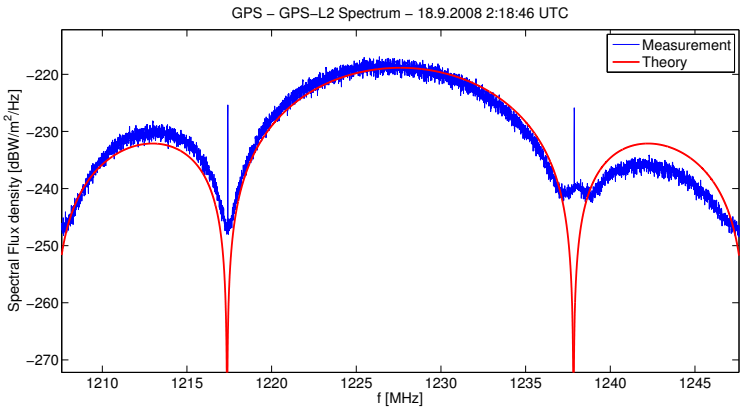

Figure 8.18: The spectral measurement of BIIR12 L2 measured shortly after the IQ data

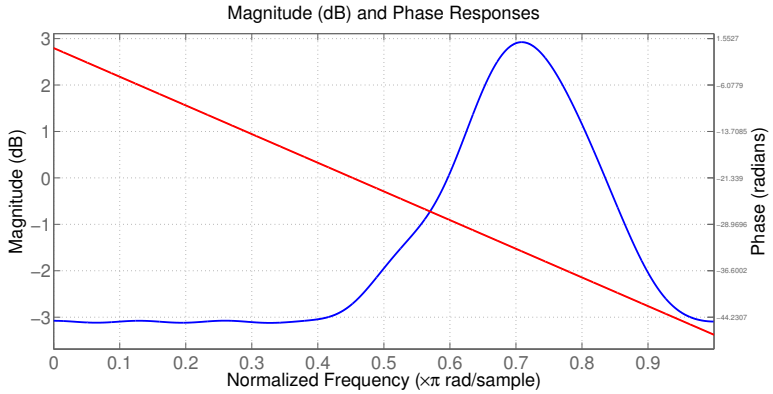

Figure 8.19: Magnitude and phase response of FIR filter

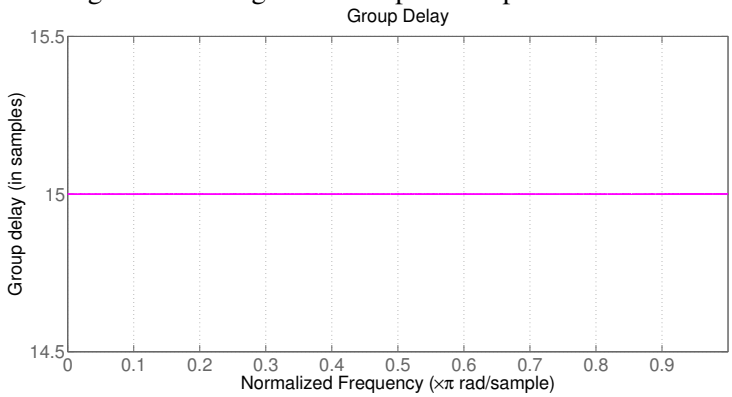

Figure 8.20: Group delay of the FIR filter

The non-linearity of the measured power spectral density can be seen in the figure 8.18, in which the zero crossing around the frequency of 1328 MHz is flattened.

The FIR filter is designed on a trial basis to be used to compensate for the dispersive behavior of the front end as seen in figure 8.19 and 8.20. The FIR filter is used, because the FIR filter has linear phase response, which will not distort the signal.

After the linear compensation with FIR filter, the spectral power has more symmetry as seen in figure 8.21. The magnitude response after compensation appears to have more symmetry. The signal still shows a little bit asymmetry because it is not exactly compensated, since the FIR filter is designed on a trial basis. The group delay is not constant, however the tendency continues to be

near zero in contrast to the group delay of figure 8.16, which is apparently not constant . The IQ constellation of the signal in figure 8.23 show less eye opening.

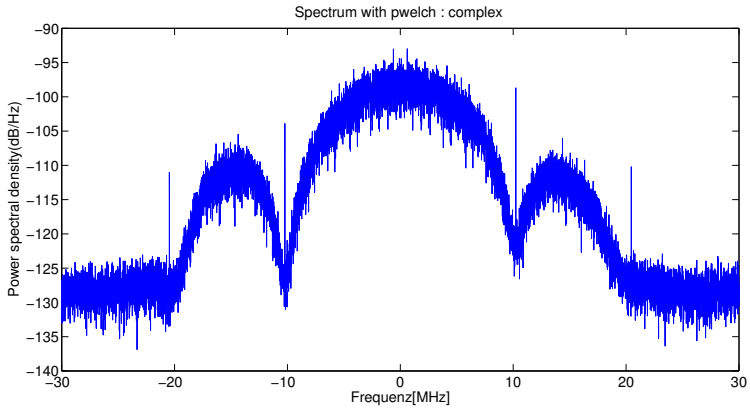

Figure 8.21: Power spectral density of BIIR12 L2 signal after compensation with FIR filter

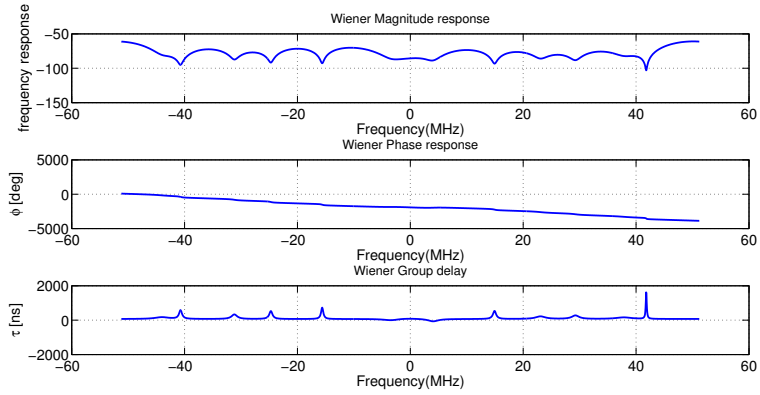

Figure 8.22: Dispersive behavior of the front end BIIR12 L2 after compensation with FIR filter

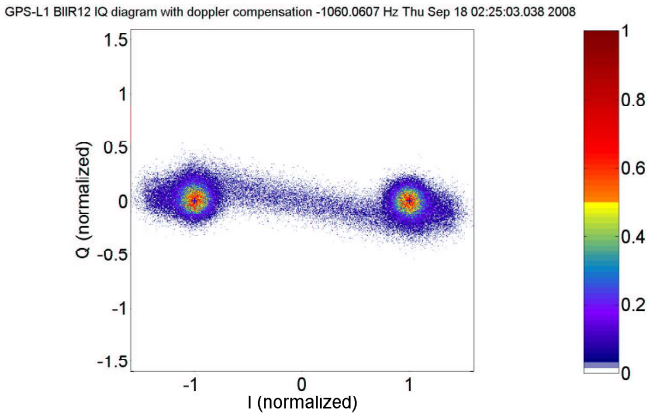

Figure 8.23: The IQ constellation of BIIR12 L2 after compensation with FIR filter

With all the previous experiments, it can be concluded that the dispersive behavior of the front-end can cause the spectrum to be asymmetric and the IQ diagram to have eye opening; however, it can be abolished through the compensation with FIR filters.

8.3 Offset of the Constant Component

The zero crossing always exists in the spectrum of legacy signals, because both C/A and P(Y) components have zero crossing at the same time in contrast to the signals with the M code. At the zero crossing the power spectrum should be at zero, but as can be seen in many previous spectrums and in figure 8.24 and 8.25 there are peaks at the zero crossing positions, which could be due to the offset of the constant component. The offset of the constant component is the imbalance between the -1 and +1 level.

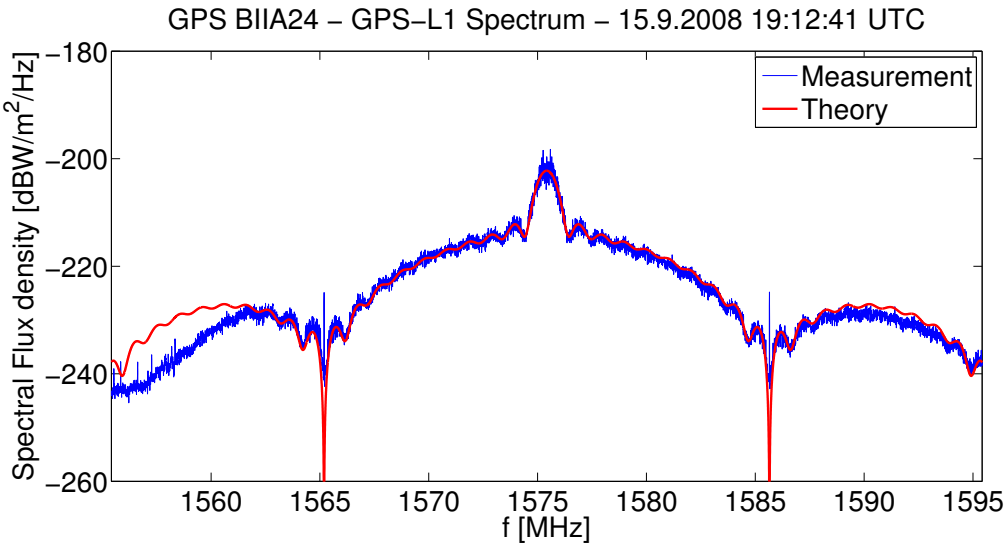

Figure 8.24: Power spectral density of the measured BIIA24 L1 signal

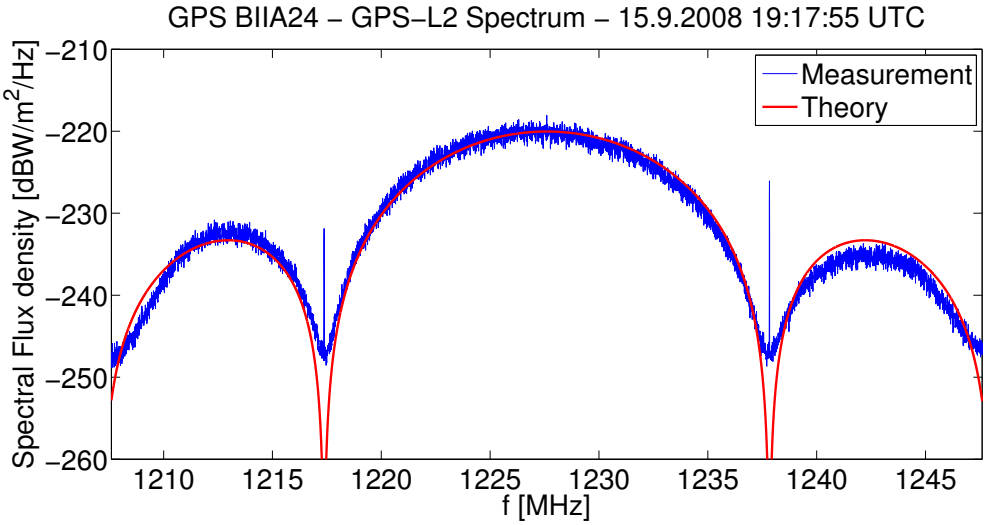

Figure 8.25: Power spectral density of the measured BIIA24 L2 signal

Firstly the time domain signals of L1 and L2 without offset are simulated and IQ diagrams are shown in figure 8.26 and 8.28. The power spectrums of L1 and L2 are then generated from the time domain signals using pwelch function in MATLAB as can be seen in figure 8.27 and 8.29. There is no offset in the code signals and therefore no peak at zero crossings can be seen.

Thereafter the L1 and L2 code signals with offset at some samples are simulated and IQ diagrams are shown in figure 8.30 and 8.32. Then the power spectrums are generated as can be seen

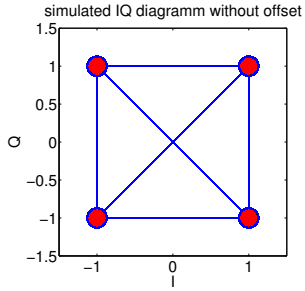

Figure 8.26: Simulated IQ diagram of L1 signal without offset

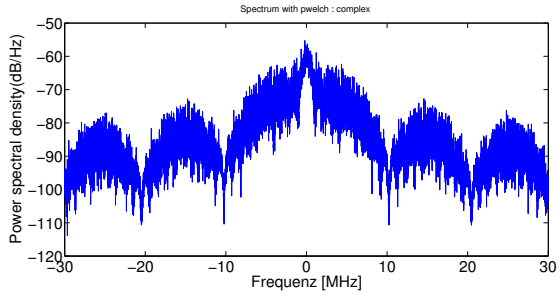

Figure 8.27: Simulation of L1 signal without offset

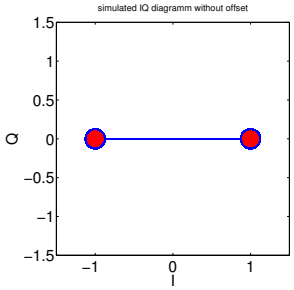

Figure 8.28: Simulated IQ diagram of L2 signal without offset

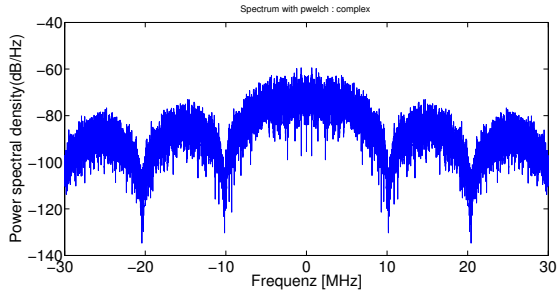

Figure 8.29: Simulation of L2 signal without offset

in figure 8.31 and 8.33. Because the offsets exist, the peaks can be seen at the zero crossings of power spectrums.

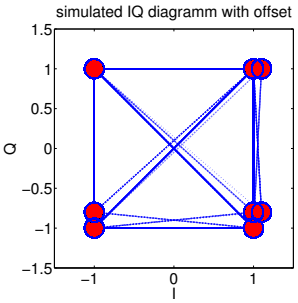

Figure 8.30: Simulated IQ diagram of L1 signal with offset

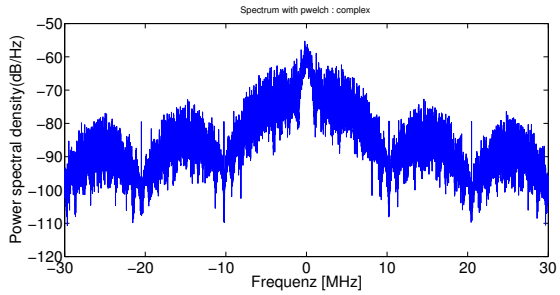

Figure 8.31: Simulation of the L1 signal with offset

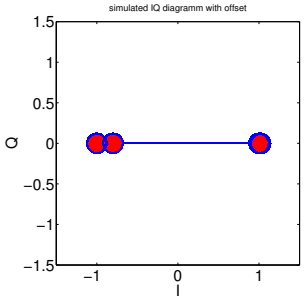

Figure 8.32: Simulated IQ diagram of L2 signal with offset

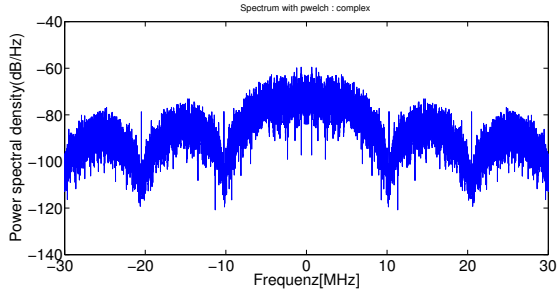

Figure 8.33: Simulation of the L2 signal with offset

Lastly in figures 8.34- 8.39 the spectrums with different offset are compared. It can be seen that the signal with more offset has the higher peaks at the zero crossings than the signal with less offset.

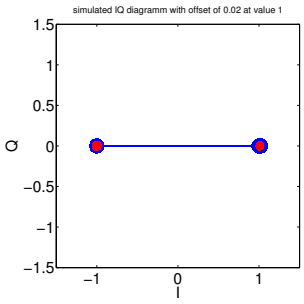

Figure 8.34: Simulated IQ diagram with offset 0.02 at some of value +1

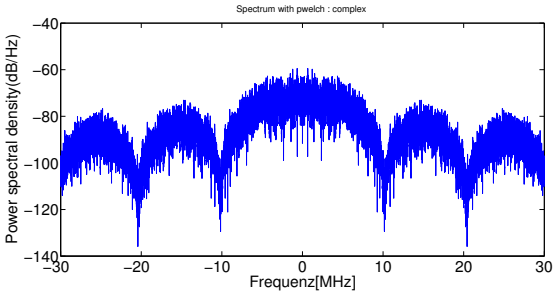

Figure 8.35: Spectrum of the simulated IQ diagram with offset 0.02 at some of value +1

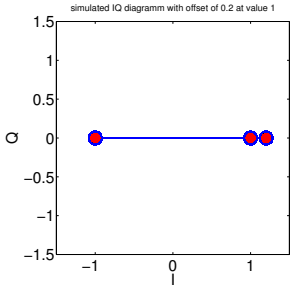

Figure 8.36: Simulated IQ diagram with offset 0.2 at some of value +1

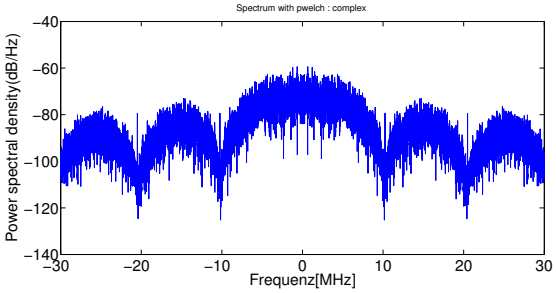

Figure 8.37: Spectrum of the simulated IQ diagram with offset 0.2 at some of value +1

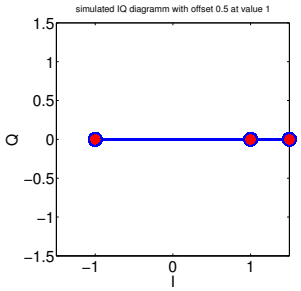

Figure 8.38: Simulated IQ diagram with offset 0.5 at some of value +1

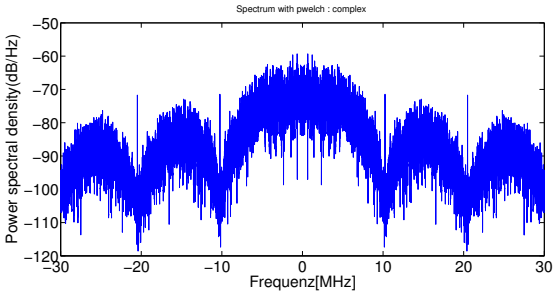

Figure 8.39: Spectrum of the simulated IQ diagram with offset 0.5 at some of value +1

9. Conclusion

This chapter concludes the research results obtained in the previous chapters and provides suggestions for future work.

The purpose of this thesis is to analyze the received signal from the 30 m high gain antenna at Weilheim.

First, the GPS signal characteristics have been detailed in order to be the references of the measurement signals. The energy and power of the signal have been defined as basic knowledge for the analysis of power spectral density. The correlation function is thoroughly studied, so that the acquisition, correlation peak determination and discriminator could be determined. The modulation schemes have been introduced including their theoretical spectral density for the comparing with the power spectral measurement. The experiment set up has been described and the signal processing has been evaluated.

The chapter 6 has analyzed the GPS measurement signals. The legacy measurement signals of BIIR12 are consistent with the specification in [24], where the L1 signal has shown more perfection of the signal. The BIIR12 L2 signal has shown asymmetry in power spectral density as well as the eye opening in the IQ constellation. Only the correlation of the BIIR12 L1 has been determined, since the P(Y) code on L2 is too long to be generated. The modernized signal measurement of BIIRM6 has been investigated.

The power of the BIIR12 and BIIRM6 signals achieved from the measurement power spectral densities have been plotted over the elevation. Both satellites have different form of the curve but the maximum and minimum power has quite the similar elevations. The difference of the power signals between the ascending and the descending satellites is not more than 0.5 dB. This difference could be due to the yaw angle of the satellites or the variation of the azimuth of the satellites. From the plot of the power asymmetry over elevation it could be concluded that the signal shows asymmetry most of the time of recorded.

The chapter 7 has demonstrated the effect of symmetric linear and non-linear phase filter, which are FIR and Chebychef filter respectively. It has been proved that the non-linear phase filter distorted signals more than the linear phase filter and the narrow bandwidth of the filter distorted the signals more than the wide bandwidth, which could be seen by the scattering of IQ constellation, error vector magnitude, the correlation peak, and the tracking error.

The chapter 8 has investigated the causes of signal deformation. The non-linear power amplification has been investigated through a simplified Saleh[29] model. The AM/PM proved to have no effect on the asymmetry of the power spectrum. However the power spectrum has been increased at some frequency and the IQ constellation has been distorted due to AM/PM. After the bandwidth limitation with linear filter assuring that no phase distortion added to the signal has been done, the IQ constellation has less distortion and the power has not shown asymmetry accordingly. The correlation peak and imbalance of the signal with AM/PM and after filtering has been determined, the peak has not been distorted due to AM/PM.

The dispersive behavior of front-end has been investigated, whereas the dispersive behavior has been obtained with Wiener solution. The power spectrum with asymmetries exhibits the asymmetrical dispersive behavior, non-constant group delay, and eye opening in the IQ constellation.

After the dispersion compensation with the linear FIR filter, the power spectrum and the dispersive behavior have shown symmetry, the group delay has developed to be nearly constant and the eye opening has been closed. From the last two points investigated, the FIR filter should be a useful filter band limiting the AM/PM distortion and also compensation for the dispersive behavior.

Lastly the spectra with the offset of the constant component have been simulated and the relationship with the peaks at zero crossings has been settled.

Four major recommendations could be made for future work.

The first one concerns the exact inter-modulation of the M code to the existing code for the ideal constellation to be established. This could be derived through the knowledge of the factors m, P_I and P_Q. If the ideal constellation is known, the error vector magnitude and their related quantities can be calculated so that the quality of the signal can be determined.

The second recommendation is about the antenna pattern. To have a conclusion about the power difference of the ascending and the descending satellite, the power signal of the satellite that passes the zenith and the satellite that does not have yaw angle should be measured and investigated. The relationship of the antenna gain with the yaw angle should be established to derive the exact antenna pattern.

The third recommendation concerns the effect of filters. The investigated filter should be the filter which is used in the actual signal path.

The fourth recommendation concerns the FIR filter. That is, the exact algorithm compensating for the dispersive behavior should be studied so that the received signal possesses more perfection.

Appendix

A1. Spectrum_Programm

A1.1 Spectrum_theory_calibrierung

- main_spectral_flux : generates the calibrated measurement compared with the theoretical spectrum

A1.2 Spectrum_antennapattern_elevation

- main_antenna_pattern_GPS : power of the measurement plot over elevations and antenna pattern
- main_antenna_pattern_peakM : power of the measurement at the M code peak plot over elevations
- main_asymmetry_elevation2 : power asymmetry plot over elevations
- main_spectrum_3D_GPS : power spectral density plot over elevations

A2. IQ_Programm

A2.1 IQ_processing

- findDoppler_GPS_CA_1 : IQ with doppler frequency compensation, rotated the signal to ideal constellation, plot constellation, EVM calculation, eye diagram plot
- findDoppler_GPS_L2CM_tle : similar to findDoppler_GPS_ca_1 but using TLE file to find doppler frequency
- correlation_xcorr : plot correlation function, imbalance, discrimination and lock point bias from the rotated IQ
- spectrum_GPS : generate spectrum with pwelch function from rotated IQ
- simulateM_inphase : simulate interplex code with variable co-efficient
- umwandel_filterung : filter the signal with different filter and bandwidth
- AMPMdistortion_L1 : experiment on non-linear amplification on L1
- AMPMdistortion_L2 : experiment on non-linear amplification on L2
- LinearLeastSquare : experiment on dispersive behavior of the front-end on L1
- LinearLeastSquareL2 : experiment on dispersive behavior of the front-end on L2
- simulate_gleichanteil : experiment on the offset of the constant component

Bibliography

[1] Pratap Misra, Per Enge.,*Global Positioning System Signal, Measurement, and Performance*, Gangga-Jamuna Press, 2004.

[2] B.Hofmann-Wellenhof, H.Lichtenegger and E.Wasle., *GNSS Global Navigation Satellite Systems*, Springer-Verlag Wien, 2008.

[3] Per Enge., *GPS Modernization: capabilities of the new Civil Signals*, Invited paper for the Australian International Aerospace Congress, Brisbane, 29 July - 1 August 2003.

[4] D.M.Akos, A.Chen, J.Dantepal, P.Enge, G.X.Gao, T.Grelier, J.Issler, S.Lo, L.Ries., *GNSS Album Images and Spectral Signatures of the New GNSS Signals*, InsideGNSS, May/June, 2006.

[5] T.Grelier, J.Dantepal, A.Delatour, A.Ghion, L.Ries., *Initial Observation and Analysis of Compass MEO Satellite Signals*, InsideGNSS, May/June, 2007.

[6] A.Chen, D.de Lorenzo, P.Enge, G.X.Gao, S.Lo., *GNSS over China : The Compass MEO Satellite Codes*, InsideGNSS, July/August, 2007.

[7] E.Rebeyrol, C.Macabiau, L.Lestarquit, L.Ries, J.L.Issler, M.L.Boucheret, M.Bousquet., *BOC Power Spectrum Densities*, ION NTM 2005, 24-26 January, 2005, San Diego, CA.

[8] J.W.Betz., *Binary Offset carrier Modulations for Radionavigation*, Journal of the Institute of Navigation, Winter 2001-2002.

[9] G.Hein, J.W.Betz, J.Rodriguez, C.Hegarty, S.Wallner, A.R.Pratt, S.Lenahan, J.Rushanan, A.Kraay, J.Owen, J.L.Issler, T.A.Stansell., *MBOC The New Optimized Spreading Modulation Recommended for Galileo L1OS and GPS L1C*, InsideGNSS, May/June, 2006.

[10] Coordination Scientific Information Center., *Global Navigation Satellite System GLONASS : Interface Control Document (version 5.0)*, Moscow,2002.

[11] capt.C.Barker, J.W.Betz, J.E.Clark, J.T.Correia, J.T.Gillis, S.Lazar, Lt.K.A.Rehborn, J.R.Straton., *Overview of the GPS M Code Signal*

[12] J.J.Spilker, A.J.V.Dierendonck., *Proposed New Civil GPS Signal at 1175.45 MHz*, ION GPS'99, 14-17 September 1999, Nashville, TN.

[13] J.W.Betz, Major D.B.Goldstein., *candidate Design for an Additional Civil Signal in GPS Spectral Bands*

[14] E.D.Kaplan, C.J.Hegarty., *Understanding GPS Principles and Applications*, Artech House INC., 2006.

[15] M.Petovello, G.Lachapelle., *GNSS Resolution: Will the L2C signal be able to be tracked by existing L2 capable(civilian) receiver*, InsideGNSS, January/February, 2006.

[16] *Navstar GPS Space Segment / User Segment L5 Interfaces*, IS-GPS-705, Initial Release, 24 November 2003. http://www.losangeles.af.mil/shared/media/document/AFD-070803-060.pdf

[17] J.G.Proakis, D.G.Manolakis., *Digital Signal Processing : Principles, Algorithms, and Applications* Pearson Prentice Hall, Upper Saddle River, New Jersey. 2007.

[18] J.Bao, Y.Tsui., *Fundamental of Global Positioning System Receivers a software approach*, Wiley-Interscience, A John Wiley& sons, Hoboken, New Jersey. 2005.

[19] R.E.Phelts, D.M.Akos., *Effects of Signal Deformations on Modernized GNSS Signals*, Journal of Global Positioning Systems, Vol.5, No.1-2:2-10, 2006.

[20] R.E.Phelts, D.M.Akos., *Nominal Signal Deformations : Limits on GPS Range Accuracy*, Presented at GNSS 2004, The 2004 International Symposium on GNSS/GPS, Sydney, Australia, 6-8 December 2004.

[21] F.Macchi, D.Borio, M.Petovello, G.Lachapelle., *New Galileo L1 Acquisition Algorithms : Real Data Analysis and Statistical Characterization* ,PLAN Gruop, Department of Geomatics Engineering, Univerity of calgary.

[22] J.L.Pinto, I.Darwazeh, *Phase Distortion and Error Vector Magnitude for 8 PSK Systems*, Department of Electrical Engineering and Electronics, University of Manchester Institute of Science and Technology(UMIST), Manchester.

[23] M.Soellner, C.Kurzhals, G.Hechenblaikner, M.Rapisarda, T.Burger, S.Erker, J.Furthner, U.Grunert, M.Meurer. S.Thoelert., *GNSS Offline Signal Quality Assessment*, ION GNSS, September 2008.

[24] *Interface Specification IS-GPS-200D*, 7 Dec 2004.

[25] M.Cuntz, S.Erker, J.Furthner, U.Grunert, M.Meurer. S.Thoelert., *GNSS Signal Verification: Spectral and Temporal Analysis of GIOVE and BEIDOU Signals*, ION GNSS, September 2008.

[26] J.Furthner., *Galileo Signal Verification and Validation*, DLR information.

[27] L.Boithias., *Radio Wave Propagation*, North Oxford Academic Publishers Ltd, 1987.

[28] S.Graf, C.Guenther., *Analysis of GIOVE-A L1-Signal*, ION GNSS 19th International Technical Meeting of the Satellite Division, 26-29 September 2006, Fort Worth, TX.

[29] A.A.M.Saleh., *Frequency-Independent and Frequency-Dependent Nonlinear Models of TWT Amplifiers*, IEEE Transactions on Communications, vol. 29, pp. 1715-1720, November 1981.

[30] *MATLAB HELP : Signal Processing Toolbox*, The MathWorks, Inc, 1984-2006.

[31] E.Rebeyrol, C.Macabiau, L.Ries, J.L.Issler, M.Bousquet, M.L.Boucheret., *Interplex Modulation for Navigation Systems at the L1 band*, ION NTM 2006, 18-20 January 2006, Monterey, CA.

[32] P.A.Dafesh, L.Cooper, M.Partridge., *Compatibility of the Interplex Modulation Method with ca and P(Y) code Signals*, ION GPS 2000, Salt Lake City, September, 2000.

[33] M.Aparicio, P.Brodie, L.Doyle, J.Rajan, and P.Torrione., *GPS Satellite and Payload*, Chapter 6 from *Global Positioning System : Theory and Applications Volume 1*, American Institute of Aeronautics and Astronautics, Inc. Washington, DC, 1996.

[34] J.J.Spilker Jr., *GPS Signal Structure and Theoretical Performance*, Chapter 3 from *Global Positioning System : Theory and Applications Volume 1*, American Institute of Aeronautics and Astronautics, Inc. Washington, DC, 1996.

[35] F.Czopek and Lt.S.Shollenberger., *Description and Performance of the GPS Block I and II L-Band Antenna and Link Budget*, 6th International Technical Meeting, The Institute of Navigation, Sept. 1993.

Internet Sources

[36] http://pnt.gov/public/images/

[37] http://commons.wikimedia.org

[38] http://en.wikipedia.org/wiki/Modulation_error_ratio

[39] http://en.wikipedia.org/wiki/Phase-shift_keying